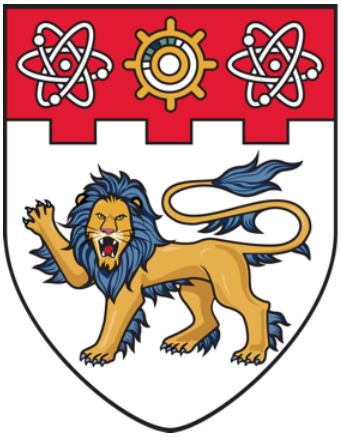

NANYANG TECHNOLOGICAL UNIVERSITY
SINGAPORE

STUDY OF THE PIEZOELECTRICITY OF TWO-DIMENSIONAL PIEZOELECTRIC MATERIALS FOR ACOUSTIC WAVE RESONATORS

SUN JIAYI

SCHOOL OF ELECTRICAL & ELECTRONIC ENGINEERING

2025

STUDY OF THE PIEZOELECTRICITY OF TWO-DIMENSIONAL PIEZOELECTRIC MATERIALS FOR ACOUSTIC WAVE RESONATORS

SUN JIAYI

SCHOOL OF ELECTRICAL & ELECTRONIC ENGINEERING

A thesis submitted to the Nanyang Technological University in partial fulfilment of the requirement for the degree of Doctor of Philosophy

2025

Statement of Originality

I hereby certify that the work embodied in this thesis is the result of original research, is free of plagiarized materials, and has not been submitted for a higher degree to any other University or Institution.

18-08-2024

. . . . . .

Date

. . . . . .

Sun Jiayi

Supervisor Declaration Statement

I have reviewed the content and presentation style of this thesis and declare it is free of plagiarism and of sufficient grammatical clarity to be examined. To the best of my knowledge, the research and writing are those of the candidate except as acknowledged in the Author Attribution Statement. I confirm that the investigations were conducted in accord with the ethics policies and integrity standards of Nanyang Technological University and that the research data are presented honestly and without prejudice.

19-08-2024

. . . . . .

Date

. . . . . .

Zhang Qing

Authorship Attribution Statement

This thesis contains the materials from two paper(s) published in the following peer-reviewed journal(s) in which I am listed as the co-first author and the first author respectively.

Chapter 5 and part of Chapter 3 and 4 are based on the paper published as Yang Yang*, Jiayi Sun*, Weifan Cai, Zheng Liu, Corinne Dejous, Magali De Matos, Hamida Hallil, and Qing Zhang. "Solidly Mounted Resonators with Ultra-High Operating Frequencies Based on 3R-MoS2 Atomic Flakes." Advanced Functional Materials 33, no. 29 (2023): 2300104.

The contributions of the co-authors are as follows:

- Prof Qing Zhang and Prof Hamida provided the initial project direction and edited the manuscript drafts.
- I characterized the materials, fabricated and characterized the devices in School of Electrical and Electronic Engineering and Cintra in Nanyang Technological University. I also analyzed the experimental data and prepared the manuscript drafts.
- Dr Yang Yang did the simulation in University of Bordeaux, France. He designed the prototype and prepared the manuscript drafts.
- I co-designed the structure of the sample with Dr Yang Yang, Prof Qing Zhang and Prof Hamida.
- Dr Weifan Cai assisted to prepare the sample and PFM measurement.
- Prof Liu Zhen provides the materials for experiment.
- Magali De Matos assisted to characterize the sample.

Chapter 6 and part of Chapter 3 and 4 are based on the paper published as Jiayi Sun, Weifan Cai, Yang Yang, Yihao Zhuang, and Qing Zhang. "2D α-In2Se3 Flakes for High Frequency Tunable and Switchable Film Bulk Acoustic Wave Resonators." *Advanced Electronic Materials* (2024): 2400498.

The contributions of the co-authors are as follows:

- Prof Qing Zhang provided the project direction and edited the manuscript drafts.
- I proposed the initial idea of the project. I characterized the materials, fabricated and characterized the devices in School of Electrical and Electronic Engineering and Cintra in Nanyang Technological University. I also analyzed the experimental data and prepared the manuscript drafts.
- Dr Weifan Cai assisted to prepare the sample and PFM calibration and measurement.
- Dr Yang Yang assisted to analyze the experimental data.
- Mr Yi Haozhuang assisted to the VNA calibration and measurement.

18-08-2024

. . . .

Date

Sun Jiayi

Acknowledgements

First, I would like to express my deepest gratitude and sincere thanks to my supervisor Prof. Zhang Qing, who has provided me this opportunity to explore the world of science research. He is a respectable scientist who possesses deep knowledge in electronic materials and physics and can always provide inspiring and far-sighted suggestions. He is very professional and principled, and can always manage the projects in a correct and efficient way.

I would like to convey my special thanks to Prof. Hamida Hallil Abbas (University of Bordeaux, France). She led me into the field of acoustic wave devices and the project 'REGENERATE'. I am sincerely grateful for my cooperator and also my friend Dr. Yang Yang. He is an expert in design and simulation of the acoustic wave devices. He is a kind and warm-hearted person who offered me many helps when I studied in University of Bordeaux, France. I would like to thank Prof Philippe Coquet, the director of CINTRA, for his strong support of this PhD project. He provided financial support for me to enter the cleaning room and help me with the characterization techniques.

I would like to acknowledge my past and current group members, Dr. Cai Weifan, Mr. Seh Wei Bin, Dr. Zou Jianping, Dr Deng Shuo, Dr. Xu Ran, Dr. Fang Xiao Yan, Dr. Wang Zhaozheng, Ms. Jin Zhuolin, Ms. Li Jinzhao, Dr. Liu Zhao Cheng, Ms. Yao Yuan, Ms. Xiang Lingxi. I like to acknowledge few more Sai Kang warriors in other research group, Dr. Yap Wen Hou, Mr. Jiang Rongtao, Mr. Chan How, Dr. Wang Xingli, Dr. Choo Yun Da, Dr. Lucas, Mr. Zhao Guangchao, Dr. Hu Yi, Dr. Zhi Kai, Dr. Wan Rongqiao, Dr. Wang Chongwu, Dr. Xie Hanlin, Dr. Suo Fei and Dr. Li Yuanbo. I also want to thanks to those NTU staffs who always offered support to me, Ms. Seet, Ms. Debbie, Ms. Choo Hwee Pin, Mr. Shamsul, Mr. Mak, Ms. Irene, Mr. Zi Ming, Mr. Kowk Fai, Ms. Yang Xiaohong and Ms. Ling Ling.

I would like to convey my special thanks to my friends who haven't been mentioned above, Dr. Liu Lingli, Dr. Yang Jinlin, Ms. Zhang Dingyi, Mr. Yu Zonghong, Dr. Pan Jingwen, Ms. Huang Xuejiao, Dr. Zhao Chunyang, Ms. Shou Yimeng, Dr. Wang Yongjun, Mr. Ye Liangtao, Mr. Chen Tianyu, Mr. Chen Cheng, Mr Li Bohao, Mr. Ge

Runlin, Mr. Wang Weilin, Mr. Liang Qinbo, Mr. Zhang Jiajie, Dr. Hu Xiaochun, Mr. Liu Zhaowei, Ms. Xiong Linrui who has always been with me and support me.

I would like to express my strong gratitude to my fiancée Qiu Qiu and my mom Ms. Chen Lei. They give me the strongest support and encouragement.

I am thankful to all technicians, seniors, colleagues, and classmates from EEE Clean Room, CINTRA, Semiconductor Characterization Lab, Nanoelectronics Lab, Nanyang Nanofabrication Center, Nanomaterials and Photonics laboratories and for their kindly assistance in my research.

Table of Contents

Contents

List of Figures

List of Tables

Abbreviations and Symbols

2D	Two dimensional
AC	Alternative current
AFM	Atomic force microscopy
AlN	Aluminum nitride
$BaTiO_3$	Barium titanate
BAW	Bulk acoustic wave
(M)BVD	(Modified) Butterworth Van-Dyke
BST	Barium strontium titanate
CIPS	$CuInP_2S_6$
CPW	Coplanar waveguide
CVD	Chemical vapor deposition
DART	Dual AC resonance-tracking
DC	Direct current
DFT	Density functional theory
DUT	Device under test
E-beam	Electron beam evaporator
FBAR	Film bulk acoustic wave resonator
FEM	Finite element method
GSG	Ground-Signal-Ground
GPS	Global positioning system
IDT	Interdigital transducers
In_2Se_3	Indium selenide

$LiNbO_3$	Lithium niobate
MEMS	Micro-electromechanical system
MIMO	Multi-input multi-output
MoS_2	Molybdenum disulfide
OBAR	Overtone bulk acoustic wave resonator
PDMS	Polydimethylsiloxane
PECVD	Plasma-enhanced chemical vapor deposition
PFM	Piezo-response force microscopy
PZT	Lead zirconate titanate
Q factor	Quality factor
RF	Radio frequency
RIE	Reactive-ion etching
SAW	Surface acoustic wave
SEM	Scanning electron microscope
Si_3N_4	Silicon nitride
SiO_2	Silicon dioxide
SMR	Solid mounted resonator
TMDCs	Transition metal dichalcogenides
vdWs	van der Waals
VNA	Vector network analyzer
XBAR	Lateral-field-excited bulk acoustical resonator
ZnO	Zinc oxide
C	Capacitor
d_{eff}	Effective piezoelectric coefficient
d_{ij}	Piezoelectric coefficient component

D	Electrical displacement
E	Electric field
f_a	Anti-resonant frequency
f_r	Resonant frequency
f_{rt}	Targeted resonant frequency
h	thickness
I_p	Incidence portion of acoustic wave
K_t^2	Electromechanical coupling coefficient
L	Inductor
P	Polarization
R	Resistor
R_p	Reflected portion of acoustic wave
s	Elastic stiffness
S	Strain
S(superscript)	At constant strain
S_{ij}	Scattering parameter component
T	stress
V_{ac}	Amplitude of AC signal
V_{dc}	Amplitude of DC signal
Z	Impedance
Z_a	Acoustical impedance
ε	Dielectric permittivity
λ	Wavelength
v	Acoustical velocity
v_l	Longitudinal acoustical velocity

ω	Angular frequency
ρ	Density

Abstract

Film Bulk Acoustic Wave Resonators (FBARs) are fundamental electronic components in modern radio frequency (RF) wireless communication systems. They use thin-film piezoelectric materials to generate and filter high-frequency acoustic waves. However, FBARs with conventional piezoelectric materials are facing a challenge to increase their resonant frequencies beyond several GHz because conventional piezoelectric materials are hard to maintain high piezoelectricity with their thickness below sub-micron. Recent advancement in two dimensional (2D) piezoelectric materials creates new opportunities in this aspect. Several 2D piezoelectric materials exhibit strong piezoelectricity with even a single atomic layer. The research carried out in this PhD project has been focused onto the pioneering studies of several typical 2D piezoelectric materials for novel FBARs, which show better performances than those counterpart devices based on conventional piezoelectric materials.

3R (3 Rhombohedral) MoS_2, a transitional metal dichalcogenide, has been theoretically predicted and experimentally confirmed to possess strong piezoelectricity regardless of the numbers of the atomic layers involved. The atomic layers are bound through van der Waals (vdWs) force and are easily exfoliated into single or few layer flakes with atomically flat and defect-free surfaces, very promising for acoustic wave device application. In this PhD project, the out-of-plane piezoelectricity of 3R-MoS_2 flakes has been characterized by Piezo-response Force Microscope (PFM) technique. 3R-MoS_2 based solid mounted resonators (SMRs), a category of FBARs, have been designed, fabricated and characterized. Ultrahigh resonant frequencies up to 27.5 GHz have been achieved with SMRs with ~200 nm thick 3R-MoS_2. To the best of our knowledge, those devices are the first bench of FBARs based on 2D piezoelectric materials in the world.

With the development of the 5/6G industry, communication band has become wider and more crowded. Compared to the static FBARs, dynamic FBARs whose resonant frequencies can be tuned corresponding to the requirements become increasingly attractive. In this PhD project, we have systematically studied the out-of-plane piezoelectricity and room-temperature ferroelectricity of 2D α phase In_2Se_3 and found that the domains of the α-In_2Se_3 flakes can be switched by a direct current (DC) electric field. This unique characteristic makes α-In_2Se_3 very promising for dynamic FBARs. To avoid the challenge of the matching between the Bragg mirror and α-In_2Se_3 flakes, we have adopted the air gap structure and successfully fabricated and characterized α-In_2Se_3 based tunable and switchable FBARs. High tuning

efficiency of 4.3 MHz/V (0.05% tuning/V at the resonant frequency of 8.60 GHz) has been achieved with 160 nm thick α-In_2Se_3 flake. The device is at the on-state under zero bias and can be switched off under a small bias voltage of − 4 V. To the best of our knowledge, it is the first dynamic FBARs based on 2D ferroelectric materials that could work beyond the sub-6G band, with a high tuning efficiency and a very small switched-off voltage.

Chapter 1 Introduction

1.1 Background and Motivation

Film Bulk Acoustic Wave Resonators (FBARs) are electronic components that use thin-film piezoelectric materials to generate and filter high-frequency acoustic waves. They are the key devices in modern wireless communication, providing efficient signal processing at high frequencies. Their small size, compatibility with standard semiconductor processes, and high Q-factor (quality factor) make them essential in mobile phones, base stations, and other radio frequency applications, etc.[1-6] FBAR technology has evolved significantly with advance in materials and fabrication techniques enhancing their performance and enabling integration into increasingly sophisticated telecommunications infrastructure. Besides, they are also widely used as oscillators[7, 8], sensors[9-12], actuators[13-15] and detectors[16, 17].

The key advantage of FBAR over an ordinary electromagnetic resonator originates in slow acoustic wave speed that is typically around 10000 times smaller than the electromagnetic waves. This makes the acoustical resonators thinner, lighter, and smaller to be integrated into microelectronic systems. For example, for a wave with frequency of 3 GHz, acoustic wave processes the wavelength of around only few μm, while 3 GHz electromagnetic wave processes wavelength of around 10 cm. Besides, the low insertion loss, high quality factor, good stability and high compatibility with semiconductor fab fabrication technologies make FBAR an ideal passive device for modern telecommunication industry. Since FBAR devices was commercialized in the later 1990s, this type of the devices has soon occupied most of market share of the RF (radio frequency) filters. Today, almost every mobile phone and some other 4/5G products contain tens of FBARs filters in their telecommunication module.

FBARs commonly consist of the top and bottom parts. The top part is constructed with one piezoelectric layer clamped by two electrodes, functioning as an acoustic wave generator and receiver. While the bottom part works as a reflector to reflect acoustic wave that is generated in the top part. Based on different structures of bottom reflectors, FBARs can be further divided into air gap-based FBARs, cavity-based FBARs, and solid mounted resonators (SMRs), as illustrated in Figure 1-1.

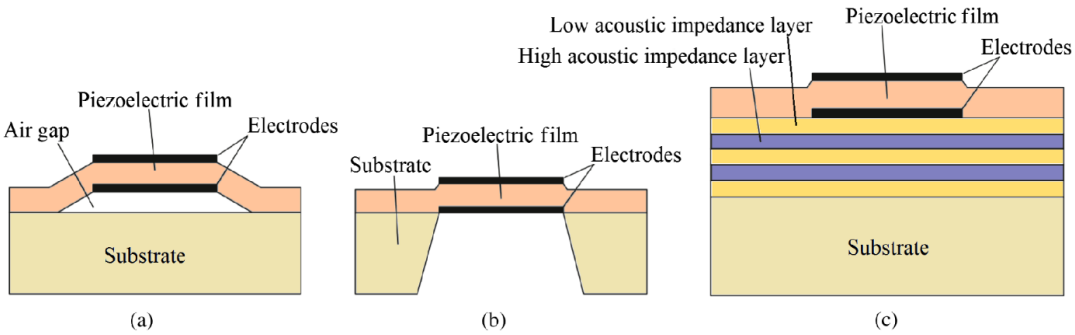

Figure 1-1 (a) Air gap-based acoustic wave resonators, (b) cavity-based bulk acoustic wave resonators, and (c) Solid Mounted Resonators (SMR)[18]

With the development of 5/6G communication technology, the communication frequency increases rapidly. Higher frequencies offer much larger bandwidths compared to lower frequencies, which is directly proportional to the data transfer rate. Higher frequencies allow for the division of the spectrum into smaller, distinct channels, enabling many users to share the network simultaneously. As a result, as the basic component of RF filters in telecommunication systems, FBARs with ultrahigh resonatant frequencies are in urgent demand. Due to inversely proportional relation between the resonant frequencies and the thickness of the piezoelectric layers, FBARs with ultrahigh frequencies (up to a dozen of GHz) require ultrathin piezoelectric films (the thickness of submicron).[19] Unfortunately, conventional piezoelectric materials used for FBARs, like AlN, ZnO, quartz, significantly suffer from piezoelectricity reduction when their thicknesses are reduced below sub 1 μm. The reduction of their piezoelectricity is caused by a few reasons. Firstly, an amorphous seed layer is formed at the beginning of the growth process of those piezoelectric materials, leading to inconsistency of the orientations for the first one hundred nanometers of the materials.[20, 21] Secondly, the influence of the surface defects increases significantly when the film is made thinner.[22] Additionally, the rough surface with a large surface to volmune ratio could cause the scattering of the acoustic wave, leading to the leakage of the acoustic wave energy. All those drawbacks limit the resonant frequencies of conventional materials based FBARs.

Recent advance in two-dimensional (2D) piezoelectric materials provides new opportunities for novel FBARs with higher resonant frequencies and additional functions. Even though most of 2D piezoelectric materials only possess piezoelectricity with odd number of atomic layers, several 2D materials such as 3R-MoS_2 and α-In_2Se_3

nano flakes are theoretically predicted and experimentally verified to possess in-plane and out-of-plane piezoelectricity, regardless of the number of atomic layers involved. [23-28] Unlike conventional materials which would significantly lose their piezoelectricity when made sub-micron thin, 3R-MoS_2 and α-In_2Se_3 nano flakes can maintain strong piezoelectricity with their thickness even down to monolayer.[26, 29] The exfoliated nanoflakes exhibit no dangling bonds due to their layered structure. Thin flakes of these materials, produced using physical exfoliation techniques, feature atomically smooth surfaces with extremely low roughness (<1 nm) and relatively fewer defects, attributed to the weak van der Waals (vdWs) bonding. All these unique properties are crucial to low loss high frequency FBAR devices. Advance in 2D piezoelectric materials casts new light on development of high performance FBAR devices.

1.2 Objectives

This research aims to study the piezoelectricity/ferroelectricity of two-dimensional piezoelectric materials, including 3R-MoS_2 and α-In_2Se_3 flakes, and design and fabricate novel high performance FBARs based on these materials. The objectives of this research are listed below:

- To characterize the piezoelectric/ferroelectric properties of two-dimensional piezoelectric materials including 3R-MoS_2, and α In_2Se_3 using advanced Piezoelectric Force Microscope (PFM) technique.
- To design and fabricate 3R-MoS_2 based solid mounted resonators (SMRs) with the targeted operational frequency above 20 GHz and to assess the performances of 3R-MoS_2 based SMRs.
- To design and fabricate ferroelectric α-In_2Se_3 based air-gap type tuneable and switchable FBAR and to assess the performances of α-In_2Se_3 based FBARs under different direct current (DC) bias.

1.3 Major Contributions

This work is the pioneering work of utilizing 2D piezoelectric materials to develop higher performance FBAR devices. The main contributions are summarized as follows:

- Out-of-plane piezoelectricity of 3R-MoS_2/α-In_2Se_3 multilayer flakes and ferroelectricity of α-In_2Se_3 multilayer flakes at room temperature were studied through piezo force microscope characterization technique. ~200 nm 3R-MoS_2 flakes possess out-of-plane piezoelectric coefficient d_{33} varying from 2.0 to 3.5 pm/V. d_{33} of α-In_2Se_3 flakes with thickness from 50 to 200 nm increases from 4 to 7 pm/V. α-In_2Se_3 flakes was experimentally confirmed to possess out-of-plane ferroelectricity at room temperature. It is found that their electrical polarizations could be switched by a small external electric field.

- 3R-MoS_2 based SMRs, as the first bench of FBARs based on 2D piezoelectric materials, have been successfully designed and fabricated. The typical resonant frequency for an SMR device based on ~200 nm 3R-MoS_2 flakes reached over 25 GHz. To the best of our knowledge, this was the highest resonant frequency achieved for the FBARs using fundamental thickness extension mode so far. Electromechanical coupling coefficient of 47.6% was achieved by an SMR with a 240 nm thick 3R-MoS_2 flake. The above results demonstrate 2D piezoelectric materials for FBAR devices are feasible.

- α-In_2Se_3 based tuneable and switchable FBARs, as the first bench of FBARs based on 2D ferroelectric materials, have been successfully designed and fabricated. The tuning of the resonant frequencies and the switching of the device as response to the applied DC bias have been studied. High tuning efficiency of 4.3 MHz/V (0.05% tuning/V at the resonant frequency up to 8.60 GHz) was achieved with a FBAR with 160 nm thick α-In_2Se_3 flake. To the best of our knowledge, this is the first tunable FBARs that can function beyond the sub-6 GHz with a high tuning efficiency and smallest switched-off voltage reported so far. The device was at the on-state under zero bias and could be switched off under a small bias voltage of − 4 V. This work shows that developing dynamic FBARs based on 2D ferroelectric materials are promising for future high-speed, multi-band communications.

1.4 Thesis Organizations

This thesis consists of 6 chapters, and it is organized in the following way:

- Chapter 1 presents a brief introduction of FBAR devices and the limitations that conventional FBARs are facing. The motivations, objectives, and major contributions are stated in this chapter.
- Chapter 2 briefs the fundamentals of piezoelectric effect and the development, application, structure, and fabrication of acoustic devices based on piezoelectric materials. The state-of-art of FBAR devices and the characterization of two-dimensional piezoelectric materials are reviewed. The advantages of using two-dimensional piezoelectric materials over conventional piezoelectric materials to develop FBAR devices are discussed.
- Chapter 3 demonstrate the methodology and the experimental setups of the AFM/PFM piezoelectricity/ferroelectricity characterization. The sample preparation process of two-dimensional materials is also discussed in this chapter.
- Chapter 4 displays the piezoelectric characterization results of 3R-MoS_2 flakes and piezo/ferroelectric characterization results of α-In_2Se_3 flakes.
- Chapter 5 shows the design, simulation, fabrication, and characterization of 3R-MoS_2 based SMRs. The performance of 3R-MoS_2 based SMRs and comparison of the performance between 3R-MoS_2 based SMRs and conventional materials based FBARs are discussed in this chapter.
- Chapter 6 shows the design, fabrication, and characterization of α In_2Se_3 based tunable and switchable FBARs. The tunability and switchability of α In_2Se_3 based FBARs are studied. The principle of the tuning and switching behavior of the devices is discussed in this chapter.
- Chapter 7 concludes the main findings of this PhD project and propose some promising work that can be conducted in the future.

Chapter 2 Literature Review

2.1 From Piezoelectricity to Acoustic Wave Resonators and Filters

2.1.1 Piezoelectric effect and piezoelectric materials

The piezoelectric effect, a fascinating phenomenon where certain materials generate an electric charge in response to the applied mechanical stress, plays an important role in modern technology. This property was first observed in 1880 by French physicists Jacques and Pierre Curie. They discovered that when pressure was applied to quartz crystals, an electric potential was generated, known as the direct piezoelectric effect. Conversely, they also observed that these materials could deform when subjected to an external electric field, known as the reverse piezoelectric effect.

Piezoelectric effect results from the linear electromechanical interaction between the strains and electric fields in crystalline materials with no inversion symmetry. Figure 2-1 shows the mechanism of piezoelectric effect and reverse piezoelectric effect with a quartz crystal. The red circles represent Si ions with positive charges while the blue circles represent O ions with negative charges. Naturally, the Si and O ions in a x-y cut quartz forms a hexagonal shape and the center of the positive Si ions overlaps with the center of the negative O ions. When a tensile force F_y is applied to the quartz crystal, the former moves downwards while the latter moves upwards relatively. In other words, net positive charges are generated at the top while net negative charges are generated at the bottom, forming an electric dipole pointing upward. Correspondingly, when a compression stress is applied to the quartz crystal, the center of the positive ions moves upwards while the center of the negative ions moves downwards relatively, resulting in negative charges on the top and positive charges on the bottom as shown in Figure 2-1 (a). The materials exhibiting the direct piezoelectric effect also exhibit the reverse piezoelectric effect. When a positive electric field (from top to bottom) is applied to the crystal, the positive ions are repelled away while the negative ions are attracted towards the top surface, inducing a tensile strain S_y on the crystal. Correspondingly, when a negative electric field (from the bottom to the top) is applied to the crystal, a compressive strain S_y is created. (Figure 2-1 (b))

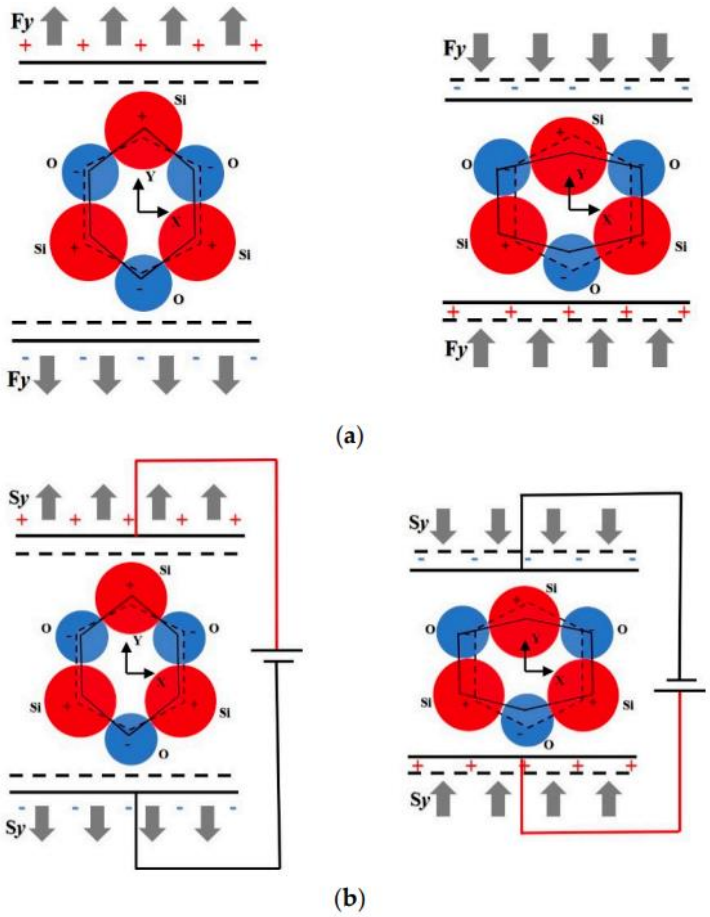

Figure 2-1 Schematic of (a) direct piezoelectric effect, and (b) reverse piezoelectric effect in a quartz crystal.[30]

Piezoelectric materials can be further divided into polar material and non-polar materials depending on whether the materials possess a net dipole moment under equilibrium. Most of polar materials contain polar molecules orienting randomly without an electric field. For those materials, a poling process where an external electric field is applied to the material for a certain period of time is required to create net polarizations. Some of the polar materials exhibit spontaneous polarizations without an external electric field, called pyroelectric materials. And if the polarizations of pyroelectric materials can be switched by external electric field, the materials are called ferroelectric materials. Figure 2-2 shows the relationship between dielectric, piezoelectric, pyroelectric and ferroelectric materials.

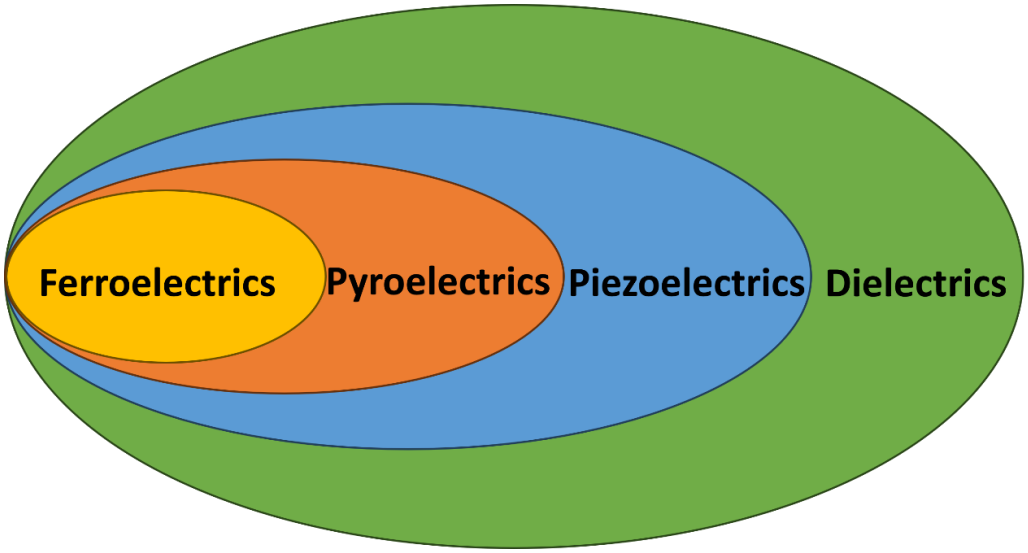

Figure 2-2 Relationship between ferroelectric, pyroelectric, piezoelectric and dielectric materials.

Discovery of the piezoelectric effect opened the door to a new field of materials science. Initially, research focused on natural piezoelectric materials like quartz, Rochelle salt, and topaz. Piezoelectric materials first aroused worldwide attention during the World War I. French scientist Paul Langévin developed a sandwich transducer based on quartz crystal to locate the submarines in the ocean. This device could listen to the acoustic wave with certain frequencies and is therefore to be considered as the prototype of sonars. After that, more and more researchers in different countries paid their attention to piezoelectric materials. In the 1950s, several groups in US, Soviet Union and Japan discovered that some ceramics possessed the same piezoelectric effect, and they were easily manufactured. Development of piezoelectric ceramics, such as barium titanate ($BaTiO_3$) and later lead zirconate titanate (PZT), marked a significant milestone. After that, commercial market for piezoelectric crystals and ceramics expanded rapidly. Until today, piezoelectric materials have become important parts of the modern world.

Piezoelectric effect offers a simple and direct way to convert mechanical energy into electrical energy or vice versa. As the results, piezoelectric materials have diverse applications in many fields. Firstly, piezoelectric materials are mostly used as actuators in electronics industries, for example ultrasonic cleaners, inkjet printers, piezoelectric buzz and speakers. For those applications, electric signals are applied to the piezoelectric materials though feeding circuits, generating strains or deformation of the piezoelectric materials. One advantage of using piezoelectric materials as actuators is that the strains and deformation can be precisely and predictably controlled with the accuracy of sub-

nanometer scale. As a result, piezo actuators have been widely used as motors/positioners in precision instruments such as Atomic Force Microscope (AFM). Secondly, piezoelectric materials are used as resonators/oscillators (timers) in electronics industries. A piezoelectric crystal possesses a natural resonant frequency. A piezoelectric resonator\oscillator is made of a bulk piezoelectric crystal whose two surfaces are coated with two metal electrodes. Resonance\oscillation is created once an AC signal is fed to the two electrodes. Due to the excellent stability, piezoelectric resonators/oscillators are always used to track the time in mechanical watches, to provide a stable clock signal for digital electronic circuits, and to stabilize the frequencies for radio communication. Then, ultrasonic detection technique used in surgery, military, and manufacturing were also developed based on piezoelectric effect. In medical applications, ultrasonic imaging of internal organs has many advantages over other imaging technologies. Ultrasonic vibrations are also used for treating joint pains, certain types of tumors for which localized heating is required and eliminating kidney and bladder stones. Sonars in military use the similar mechanism to detect enemy's submarines. Ultrasonic wave reflection can be applied in manufacturing for non-destructive testing. Moreover, piezoelectric sensors are widely used in both industries and customer electronics to measure changes in pressure, acceleration and strains. Piezoelectric sensors usually based on two mechanisms. One is to monitor piezoelectric signals induced by the strain variation of the piezoelectric materials to detect pressure, acceleration or forces, etc. Accelerators in vehicles, tilt sensors in customer electronics and pressure sensors in touch pad are based on this mechanism. The other is to monitor the changes of the nature resonant frequencies of crystal resonators to extract the information of the stress or strain applied. High sensitivity gas sensors and pressure sensors typically contain a piece of piezoelectric materials to generate piezoelectric signals. What's more, piezoelectric signals are generated by mechanical to electric power conversion process. In other word, piezoelectric materials exhibit a great application potential for mechanical power\energy harvesting.[31-35]

2.1.2 Constitutive piezoelectric equation

Direct piezoelectric effect is a linear process of piezoelectric materials to generate additional charge by applied stress. As a result, in terms of charge density displacement D (charge Q per area A) and stress T, direct piezoelectric effect could be described by:

$$D_{3\times1} = d_{3\times6} \cdot T_{6\times1} \tag{2.1}$$

where d is the piezoelectric coefficient. It should be noticed that D, T and d are in the form of matrix, the subscripts are the number of rows and columns of their matrix.

Similarly, the reverse piezoelectric effect could be described by:

$$S_{6\times1} = d^t_{6\times3} \cdot E_{3\times1} \tag{2.2}$$

where S is the strain, E is the electric field strength, d^t is the reverse matrix of d, representing the piezoelectric coefficient.

Equations (2.1) and (2.2) describe the linear electrical-mechanical coupling behavior of a piezoelectric material. Note that a common piezoelectric material is a dielectric material. Thus, the electrical behavior could be described by:

$$D_{3\times1} = \varepsilon_{3\times3} \cdot E_{3\times1} \tag{2.3}$$

As a common piezoelectric material is a linear elastic material, the mechanical behavior should also be governed by the Hooke's Law:

$$S_{6\times1} = s_{6\times6} \cdot T_{6\times1} \tag{2.4}$$

where s is the compliance.

Combine equation (2.1) with (2.3), and equation (2.2) with (2.4), the constitutive piezoelectric equations (in strain-charge form) for a piezoelectric material could be achieved:

$$D_{3\times1} = d_{3\times6} \cdot T_{6\times1} + \varepsilon^T_{3\times3} \cdot E_{3\times1} \tag{2.5}$$

$$S_{6\times1} = s^E_{6\times6} \cdot T_{6\times1} + d^t_{6\times3} \cdot E_{3\times1} \tag{2.6}$$

The superscripts in s^E stands for that the compliance is under a constant electric field and ε^T stands for that the dielectric constant is under a constant stain. In the equation (2.5), the first term $d \cdot T$ describes the contribution of the direct piezoelectric effect of a

piezoelectric material to the charge density displacement. The second term $\varepsilon^T \cdot E$ describes the charge density displacement caused by an electric field. In Equation (2.6), the first term $s^E \cdot T$ describes the stress induced deformation governed by Hooke's Law, which can be applied to all the linear elastic materials. The second term $d^t \cdot E$ introduces the contribution of the reverse piezoelectric effect induced deformation in a piezoelectric material under an electric field. The constitutive piezoelectric equations (2.5) and (2.6) mathematically describe the interactions between the strain, stress, charge density displacement and electric field for a piezoelectric material during the process of piezoelectric effect.

The constitutive piezoelectric equation (strain-charge form) for a typical piezoelectric ceramic with space group of 4mm or 6mm could be written as:

$$\begin{bmatrix} D_1 \\ D_2 \\ D_3 \end{bmatrix} = \begin{bmatrix} 0 & 0 & 0 & 0 & d_{15} & 0 \\ 0 & 0 & 0 & d_{24} & 0 & 0 \\ d_{31} & d_{32} & d_{33} & 0 & 0 & 0 \end{bmatrix} \begin{bmatrix} T_1 \\ T_2 \\ T_3 \\ T_4 \\ T_5 \\ T_6 \end{bmatrix} + \begin{bmatrix} \varepsilon_{11}^T & 0 & 0 \\ 0 & \varepsilon_{22}^T & 0 \\ 0 & 0 & \varepsilon_{33}^T \end{bmatrix} \begin{bmatrix} E_1 \\ E_2 \\ E_3 \end{bmatrix} \quad (2.7)$$

$$\begin{bmatrix} S_1 \\ S_2 \\ S_3 \\ S_4 \\ S_5 \\ S_6 \end{bmatrix} = \begin{bmatrix} s_{11}^E & s_{12}^E & s_{13}^E & 0 & 0 & 0 \\ s_{21}^E & s_{22}^E & s_{23}^E & 0 & 0 & 0 \\ s_{31}^E & s_{32}^E & s_{33}^E & 0 & 0 & 0 \\ 0 & 0 & 0 & s_{44}^E & 0 & 0 \\ 0 & 0 & 0 & 0 & s_{55}^E & 0 \\ 0 & 0 & 0 & 0 & 0 & s_{66}^E \end{bmatrix} \begin{bmatrix} T_1 \\ T_2 \\ T_3 \\ T_4 \\ T_5 \\ T_6 \end{bmatrix} + \begin{bmatrix} 0 & 0 & d_{31} \\ 0 & 0 & d_{32} \\ 0 & 0 & d_{33} \\ 0 & d_{24} & 0 \\ d_{15} & 0 & 0 \\ 0 & 0 & 0 \end{bmatrix} \begin{bmatrix} E_1 \\ E_2 \\ E_3 \end{bmatrix} \quad (2.8)$$

The subscripts 1, 2, 3, 4, 5, 6 stand for the x, y, z, xy, yz, xz direction in Cartesian coordinate system. The piezoelectric coefficient d_{31} stands for the induced charge density displacement in z direction when the applied stress is with x direction, or induced strain in x direction when the applied electric field is with z direction. Similarly, the piezoelectric coefficient d_{24} stands for the induced charge density displacement in y direction when the applied stress is a shear stress with xy direction, or the induced strain in xy direction when the applied electric field is with y direction.

The piezoelectric coefficient matrices for piezoelectric materials with other space groups are provided in the cited database.[36]

2.1.3 Acoustic wave resonators and filters

The generation of acoustic waves through the piezoelectric effect involves the interaction between electrical signals and mechanical vibrations within the piezoelectric materials. As discussed above, when an external electric field is applied to a piezoelectric material, the material deforms (be stretched or compressed normally) in a certain direction in response to the electric field. If an alternative electric field is applied, the piezoelectric material must deform back and forth. As a result, an acoustical vibration is generated. The frequency of the vibration depends on the frequency of the alternative electric field. The mode of the vibration depends on the piezoelectric and elastic properties of the material and the electric field direction. If the frequency of vibration matches with the intrinsic frequency of the piezoelectric material's vibration mode, a standing wave is generated, and the vibration is greatly enhanced. This is the acoustic resonance, and the frequency is called resonant frequency. Several modes of acoustic waves can be generated by piezoelectric effect. Generally, acoustic waves are divided into bulk acoustic waves (BAW), and surface acoustic waves (SAW). Bulk acoustic waves propagate through the entire body of the piezoelectric material with either thickness extension mode or thickness shear mode. In the former mode, the displacement direction is consistent with the wave propagation direction, (which means the material is compressed and stretched), as shown in Figure 2-3 (a). While in the latter mode, the displacement direction is perpendicular to the wave propagation direction, as shown in Figure 2-3 (b). Surface acoustic wave propagates along the material surface, the wave declines rapidly with the depth into the material. Usually, surface acoustic waves are generated by interdigital transducers (IDTs) (Figure 2-3 (c)).

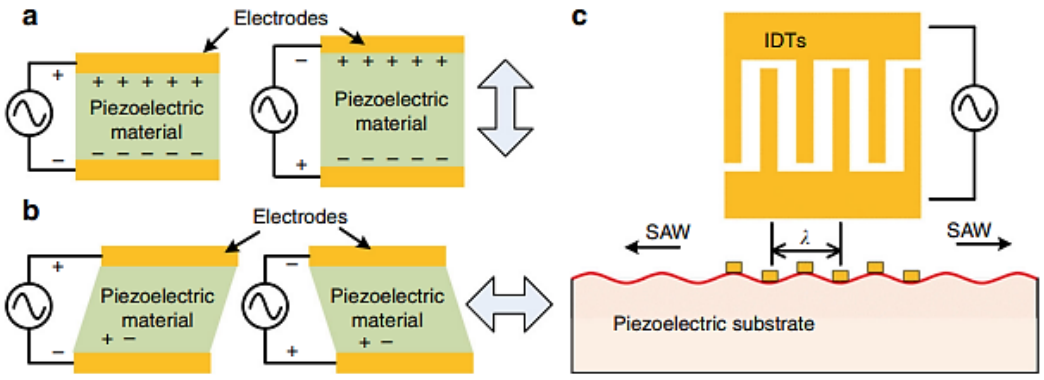

Figure 2-3 Schematic of (a) Thickness extension mode acoustic wave. (b) Thickness shear mode acoustic wave. (c) Surface acoustic wave.[37]

Acoustic wave resonators suppress unwanted frequency modes from being transmitted in the devices, while allowing the specific resonance frequency to be received and transmitted, functioning like bandpass filters. They have been used in many areas, including mobile communication systems (CDMA, UMTS, GSM, etc.), global positioning systems (GPS, Beidou, Galileo, etc.), data transmission systems (WLAN, Bluetooth, etc.), satellite, military communication systems, etc. Today, almost every smart phones and other wireless communication modules contain up to several tens of acoustic wave devices as RF filters.

Velocities of acoustic waves in piezoelectric materials usually are 4 to 5 orders lower than electromagnetic waves. Therefore, for same working frequency, the size of acoustic wave resonators are 4 to 5 orders smaller than that of electromagnetic wave resonators. (Wavelength equal to velocity divide by frequency.) For example, for a resonator with a resonant frequency of around 1 GHz, the corresponding wavelength of electromagnetic waves are around 0.3 meters, while the corresponding wavelength of acoustic waves are around a few micrometres. Therefore, the size of acoustic wave resonators can be comparable with the size of a standard integrated circuit chip. Additionally, FBAR devices typically exhibit lower insertion loss, high out-of-band rejection, good temperature stability and low cost compared to other resonator technologies. By virtue of those advantages discussed above, acoustic wave resonators have rapidly occupied the market of radio frequency resonators.

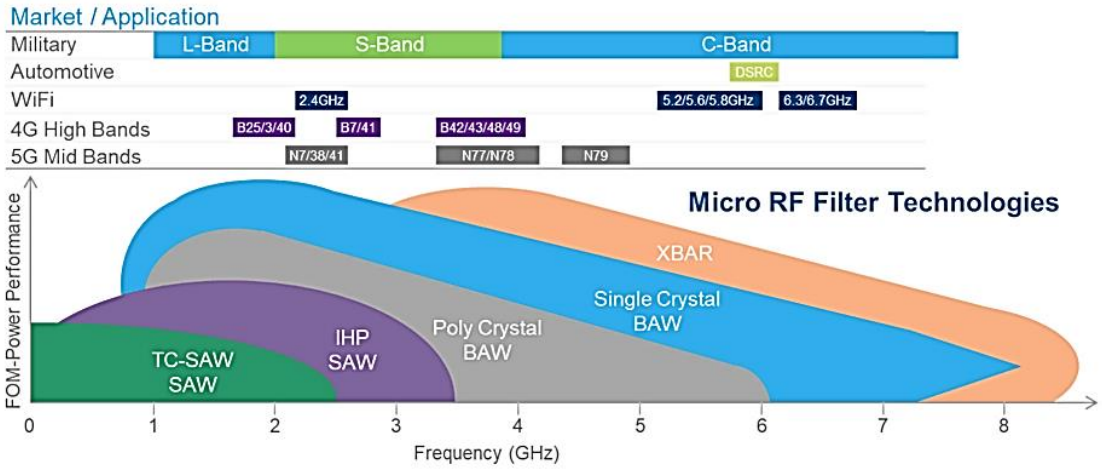

Figure 2-4 Market application, band allocation of RF filter technologies[38]

Figure 2-4 shows market application, band allocation and working frequency of different types of acoustic wave devices. Surface acoustic wave resonators have advantages of being easily designed and manufactured compared to bulk acoustic wave

resonators when working frequency is below a few GHz. Designers can simply determine the resonant frequency of SAW resonators through adjusting the spacing between the IDT fingers. And fabrication of SAW resonators is normally a single-mask process. However, SAW resonators' working frequency is hard to raise up to a few gigahertz due to the limitation to fabrication of submicron IDT finger spacing. As a result, bulk acoustic wave resonators dominate the super-high frequency market.

BAW resonators utilize acoustic wave propagating along the out-of-plane direction through the piezoelectric body. The working frequencies of BAW resonators can be increased by reducing the thickness of the piezoelectric materials. The working frequencies of BAW resonators are typically between 1 to 7 GHz, higher than those of SAW resonators, and they are of higher quality factors and low insertion lose. Unfortunately, BAW resonators are fabricated with relatively more complicated processes than SAW resonators.

XBAR refers to the lateral-field-excited bulk acoustical resonator. Unlike a conventional BAWs which have two electrodes clamping the piezoelectric material, an XBAR has electrodes on the same top surface of the piezoelectric material. XBAR is a novel type of BAWs proposed by researchers in 1990s. It has the potential to break through the limitation of working frequencies of conventional SAWs and BAWs. However, this type of devices is still in the research stage and haven't been commercialized yet. The details of XBARs are discussed later in this chapter.

In this PhD thesis, we only focus on one major type of BAWs, i.e., thin film bulk acoustic wave resonators (FBARs).

2.2 The Theory of FBAR

2.2.1 Structure and principle of FBAR

As introduced in the Chapter one, FBARs, resonating in a frequency range up to several GHz, are the basic component of radio frequency filters for modern wireless communication system like Wi-Fi and GPS. As shown in Figure 2-5 (a), a typical FBAR consists of a top and a bottom part. In the top part, a piezoelectric layer is sandwiched

with two metal electrodes, functioning as an acoustic wave generator. The bottom part is usually a cavity or an acoustical reflector, with the function of acoustical isolation from the supporting substrates to reduce acoustic wave loss.

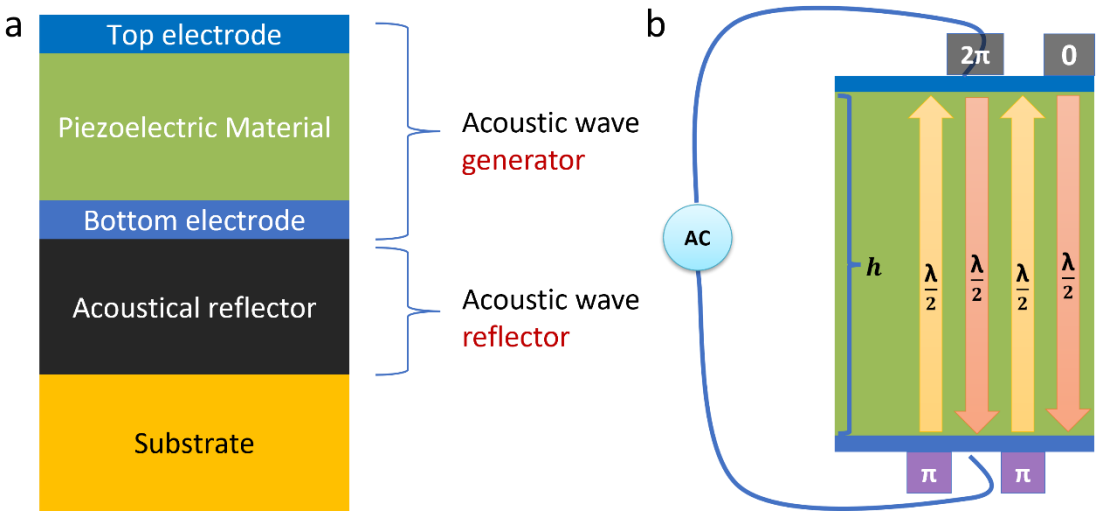

Figure 2-5 (a) Structure of a typical FBAR. (b) Schematic diagram of the wave propagation in a FBAR at resonant frequency.

Depending on the design of the bottom part, FBARs can be divided into three types – air gap-based, cavity-based bulk acoustic wave resonators, and SMRs as shown in Figure 1-1. Therefore, the fabrication process to form the acoustical isolation is also different. For a cavity FBAR, a back side etching process is used at the end of the fabrication process. A cavity is then formed below the active region (the top part).[7] For an air gap FBAR, a sacrificial layer was buried before the fabrication of the active region, and it is then etched away to form an air gap between the top part and supporting substrates at the end of the process.[39] SMRs use Bragg mirror structure as the acoustical reflector. Two materials with large difference of acoustic impedance are deposited alternately. Thickness of each layer of the Bragg mirror is designed to be a quarter of the wavelength at the resonant frequency. When the longitudinal acoustic wave propagates through the Bragg mirror, it is reflected by the layer with high acoustical impedance and low acoustical impedance. As the result, there will be less loss of the acoustic energy at the resonant frequency.

SMRs are more stable in structure domain, while air gap/cavity FBARs are more fragile and easier to break during fabrication process. Additionally, due to the negative temperature coefficient of frequency (TCF) of SiO_2, SMRs contains of SiO_2 layers have better TCF matching.[19]

Figure 2-5 (b) shows the schematic diagram of the longitudinal acoustic wave propagation in the top part of a FBAR at resonant frequency. When an AC signal is applied to the top and bottom electrodes of a FBAR, deformation is generated in the piezoelectric material, forming an acoustic wave propagating in the longitudinal direction. This acoustic wave is reflected back and forth between the two electrodes. When a certain frequency of the AC signal is applied so that half of the wavelength of the generated acoustic wave corresponds to the thickness of the piezoelectric material, all the longitudinal waves including the original wave and the reflected waves propagate in the same directions with the same phase. (Assume that the original wave starting at the top electrode is with phase of 0, after half of the wavelength travel, the phase will be π, then after reflected and another half wavelength travel, it becomes 2 π and so on.) Their energy gathers together to form a strong standing wave. The FBAR is in resonance, and the frequency is called the resonant frequency. The fundamental resonant condition is:

$$h = \frac{\lambda}{2} \tag{2.9}$$

, where h is the thickness of the piezoelectric material, λ is the wavelength of the longitudinal acoustic wave.

2.2.2 The equivalent circuit of FBAR

In order to simplify the analysis and design of the FBARs, equivalent circuits that could represent their complex physical and electrical behavior in terms of standard electrical components were developed. The Butterworth Van-Dyke (BVD) model is the most used model to describe the electrical behavior near the resonant frequency of the FBAR.

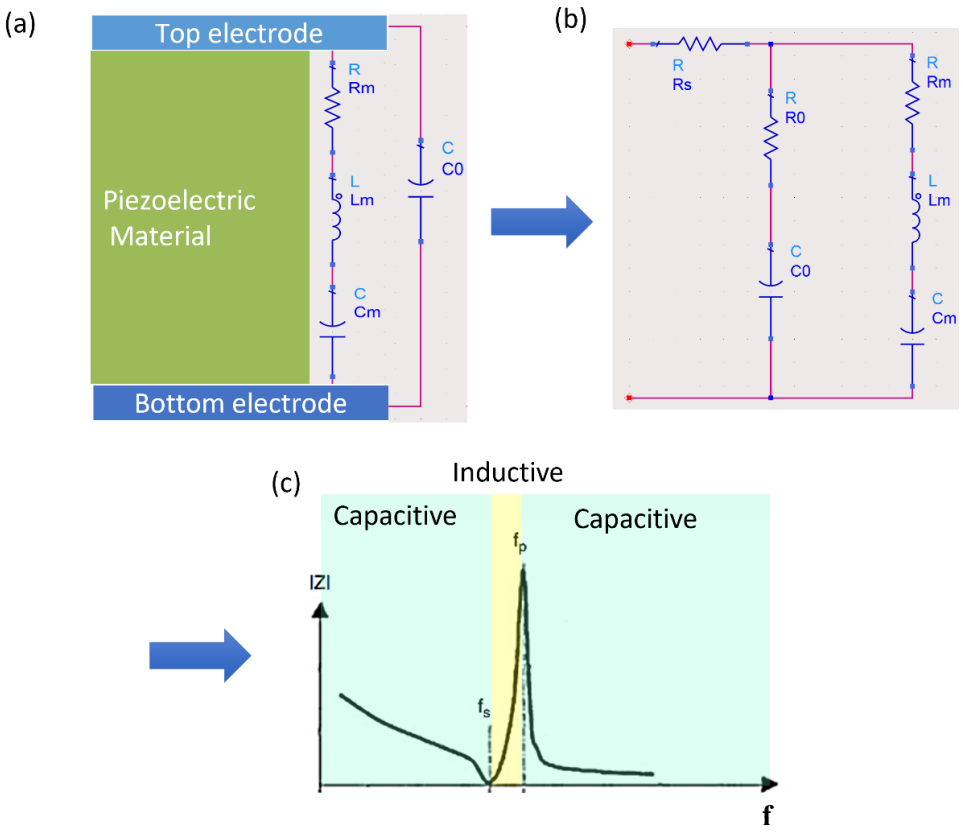

Figure 2-6 (a) BVD model and (b) MBVD model of FBAR. (c) Frequency response of a FBAR.[19]

When an AC signal is applied upon a piezoelectric material, mechanical energy and electrical energy are stored and converted inside the piezoelectric material. As a result, R_m, L_m and C_m series circuit can represent the electrical and mechanical behavior of a piezoelectric material, as shown in Figure 2-6 (a). Specifically, at the resonance, the electrical energy and mechanical energy are mutually converted through direct and reverse piezoelectric effect. This conversion can be represented as the energy conversion between one inductor L_m and one capacitor C_m in series, and the R_m represents the loss during the energy conversion. The capacitor C_0 in parallel in the circuit, represents the static capacitance between the two electrodes. Those parameters are described as:

$$C_0 = \frac{\varepsilon_{33}^T A}{2h} \tag{2.10}$$

$$C_m = \frac{8}{\pi^2} K_t^2 C_0 \tag{2.11}$$

$$L_m = \frac{h^2}{2K_t^2 C_0 v_l^2} \tag{2.12}$$

$$R_m = \frac{\pi^2 \eta_{33}}{8\rho K_t^2 C_0 v_l^2} \tag{2.13}$$

where ε_{33}^T is the out-of-plane dielectric constant of the piezo layer in-between under constant strain. A is the facing area of the two electrodes. h is the thickness of the piezoelectric material. K_t^2 is the electromechanical coupling coefficient. v_l is the longitudinal wave velocity. ρ is the density of the piezoelectric material. η_{33} is the damping coefficient. By using the BVD model, the coupling between the mechanical energy and electrical energy can be analyzed in electrical domain, which largely simplifies the design and analysis of the FBAR devices.

A main limitation of the BVD model is that it only considers the mechanical damping of the clamped piezoelectric material, while the dielectric loss of the piezoelectric material and the electrical loss of the electrodes are not included. The Modified BVD model was developed to describe the acoustic motional behavior of the FBAR more accurately, as shown in Figure 2-6 (b). The R_0 represents the dielectric loss of the piezoelectric material, and the R_s represents the electrical loss of the metallic electrodes.

According to the MBVD equivalent circuit shown in Figure 2-6 (b), the following equations hold respectively at resonant frequency f_s and anti-resonant frequency f_p:

In the resonance: $$2\pi f_s L_m = \frac{1}{2\pi f_s C_m} \tag{2.14}$$

In the anti-resonance: $$2\pi f_p L_m = \frac{1}{2\pi f_p C_0} + \frac{1}{2\pi f_p C_m} \tag{2.15}$$

From equations above, we can derive:

the Resonant frequency: $$f_s = \frac{1}{2\pi\sqrt{L_m C_m}} \tag{2.16}$$

and the anti-resonant frequency: $$f_p = \frac{1}{2\pi\sqrt{L_m(\frac{C_0 C_m}{C_0+C_m})}} \quad (2.17)$$

The electrical resonance of a FBAR device have a few features as shown in the Figure 2-6 (c). The f_s is smaller than the f_p. Near the resonant frequency, a low impedance stage shows up, while near the anti-resonant frequency, a high impedance stage shows up. A phase change from capacitive to inductive between the f_s and f_p can also be observed.

Electromechanical coupling coefficient K_t^2 is a crucial parameter for FBAR devices. It describes the conversion efficiency between electrical and acoustic energy. For a FBAR, the K_t^2 can be calculated using the resonant frequency (f_s) and the anti-resonant frequency (f_p) through Equation 2.18.

$$k_t^2 = \frac{\frac{f_r}{f_a}\cdot\frac{\pi}{2}}{tan\,(\frac{f_r}{f_a}\cdot\frac{\pi}{2})} \quad (2.18)$$

A large K_t^2 is required for wideband FBAR based filters. [1]

2.2.3 Filter design based on FBAR

FBARs are the basic components of RF filters. Figure 2-7 demonstrates three basic filter topologies based on FBARs: (a) ladder type, (b) lattice type and (c) mixed type.

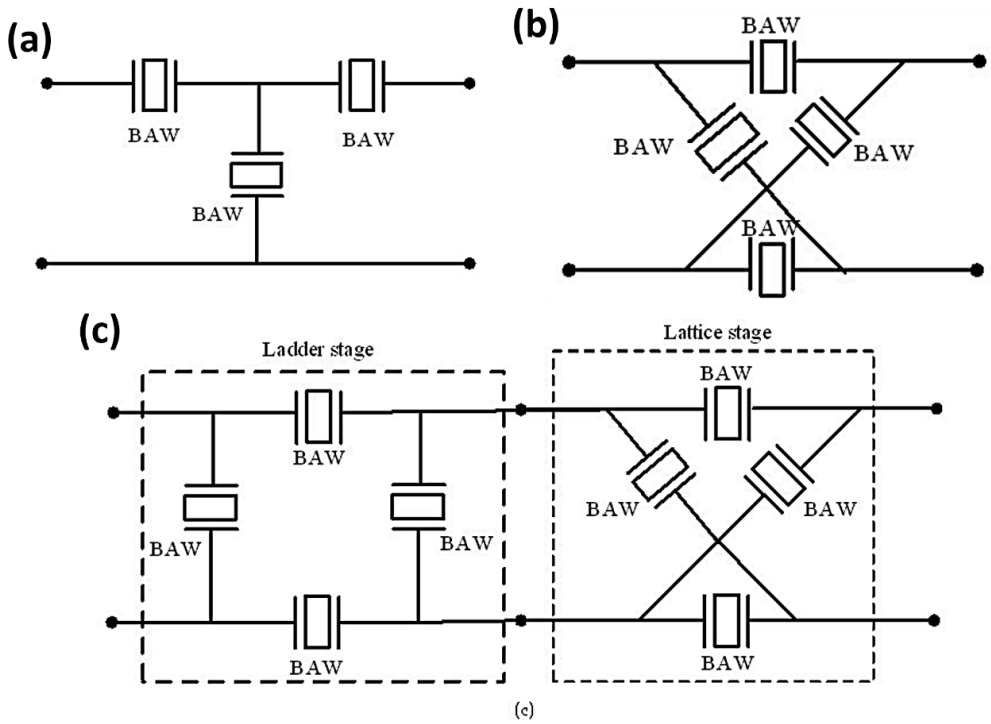

Figure 2-7 Three basic filter topologies based on FBARs:(a) Ladder type, (b) Lattice type and (c) Mixed type.[1]

Among them, the ladder type filters exhibit high rejection for the signals close to the passband but presenting low isolation for signals out-of-band. On the contrary, the lattice type filters have good isolation for signals out-of-band but presenting poor selectivity for signals close to the passband. The mixed type filters combine both ladder type and lattice type filters, as a result, exhibiting the advantages of both network types, i.e., steep response close to the passband and high isolation at undesired bands.

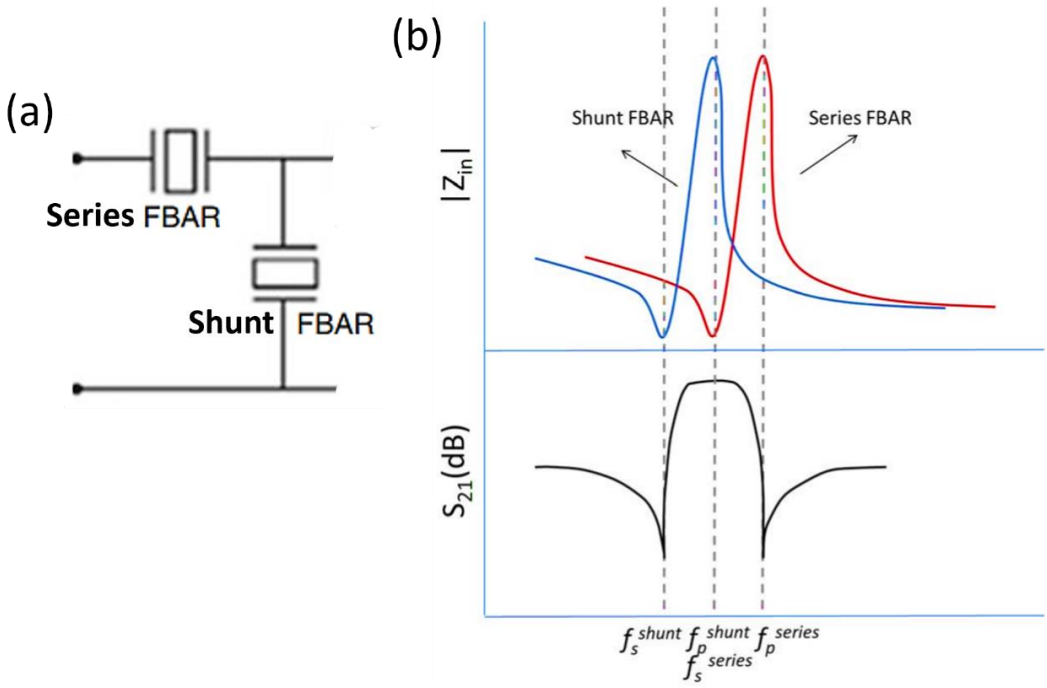

Figure 2-8 (a) A single stage ladder type filter. (b) The frequency responses of the single series and shunt FBAR devices and the cascading.[40]

Take a single stage series and shunt FBAR ladder type filter as an example to explain the principle of the filters based on FBARs, as shown in Figure 2-8 (a). The typical frequency response of the filter is shown in Figure 2-8 (b). The resonant frequency of the series FBAR is made slightly higher than that of the shunt FBAR. (Usually by tuning the thickness of top electrodes) When the frequency of the input signal is near the resonant frequency f_s of series FBAR, the series FBAR is in low impedance state, while the shunt FBAR are in high impedance state near its anti-resonant frequency f_p. As a result, this signal can pass the filter without much degradation. At resonant frequency f_s of the shunt FBAR, the shunt FBAR is in low impedance state, and major part of the input signal goes to the ground. At anti-resonant frequency f_p of series FBAR, the series FBAR have high impedance, and signal cannot pass through it. For signals out-of-band, both the series FBAR and shunt FBAR show medium impedance, therefore, certain level of isolation is achieved.

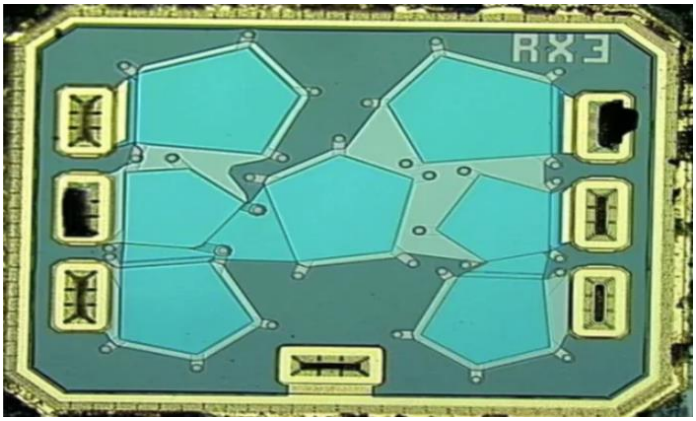

Figure 2-9 A real filter consisted by 7 FBAR.[41]

Figure 2-9 shows a real case of a RF filter consisting of 7 FBARs. This filter used a 3.5-order ladder structure, where 3 FBARs were in series and 4 FBARs were in parallel.

2.2.4 Characterization of FBAR

To characterize the performance of BAW devices, the scattering parameters of high frequency microwave network, *S* parameters, are always measured and analysed. Take the most used two port system as an example, the *S* parameters describe the energy transmission between Port 1 and Port 2. Figure 2-10 shows an example of a two-port network, a_j is signal input at Port j, b_i is signal detected at Port i (i,j=1,2).

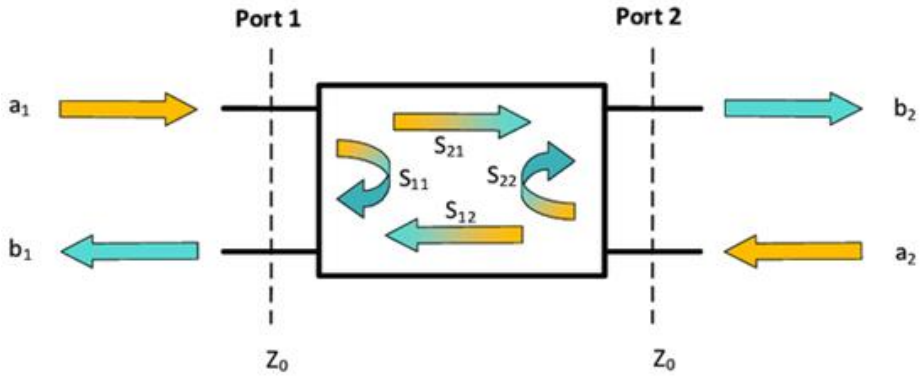

Figure 2-10 S parameters of a two-ports network[42]

The a_j and b_i in a two-port system are linked by the S matrix below:

$$\begin{bmatrix} b_1 \\ b_2 \end{bmatrix} = \begin{bmatrix} S_{11} & S_{12} \\ S_{21} & S_{22} \end{bmatrix} \begin{bmatrix} a_1 \\ a_2 \end{bmatrix} \tag{2.19}$$

The equations of *S* parameters of a two-ports network are:

$$S_{11} = \frac{b_1}{a_1}\Big|_{a_2=0} \quad S_{21} = \frac{b_2}{a_1}\Big|_{a_2=0}$$
$$S_{22} = \frac{b_2}{a_2}\Big|_{a_1=0} \quad S_{12} = \frac{b_1}{a_2}\Big|_{a_1=0} \tag{2.20}$$

The four S parameters are therefore defined as:

S_{11}: the reflection coefficient at Port 1 when Port 2 is terminated with a matched load.

S_{12}: the reverse transmission coefficient when Port 1 is terminated with a matched load.

S_{21}: the forward transmission coefficient when Port 2 is terminated with a matched load.

S_{22}: the reflection coefficient at Port 2 when Port 1 is terminated with a matched load.

As a one-port device, S_{11} is always used to characterize the BAW resonators and the corresponding impedance Z can be expressed as:

$$Z = \frac{1+S_{11}}{1-S_{11}} Z_0 \tag{2.21}$$

where Z_0 is normalized impedance of the transmission line, normally with the value of 50 Ω.

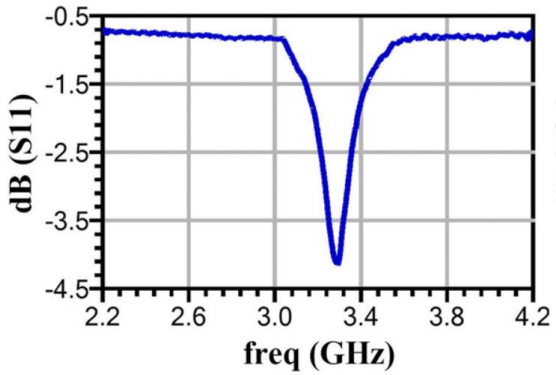

Figure 2-11 Example of S_{11} parameters of a FBAR.[43]

Figure 2-11 shows a typical S_{11} parameter versus frequency of a FBAR. The S_{11} peaks at the resonant frequency of around 3.3 GHz. When the frequency of the input signal is away from the resonant frequency, the device is of high impedance and almost all the electrical energy inputted from the source is reflected. As a result, S_{11} is near 0. When the frequency of the input signal is at the resonant frequency, the input impedance of the FBAR drops significantly so that more electrical energy inputted from the source can

pass the device, leading to a sharp S_{11} peak at the resonant frequency. The *S* parameter characterization is the most commonly used method to test the performance of FBAR devices and from the values and phases of *S* parameter results, the resonant frequency, quality factor (Q), anti-resonant frequency, electromechanical coupling coefficient and other information of the FBAR under test can be extracted.

Usually, a vector network analyzer (VAN) is used for the S parameter characterization. The VNA is then connected to the device under test (DUT) through a coplanar waveguide (CPW). The VNA provides the excited signal through the CPW to the DUT and receive the reflected or transmitted signals. Therefore, the results achieved by VNA are electronic performance of CPW cascaded with DUT rather than the pure performance of the DUT. To solve this issue, a technique call de-embedding was developed. The basic principle of the de-embedding is shown in the Figure 2-12.

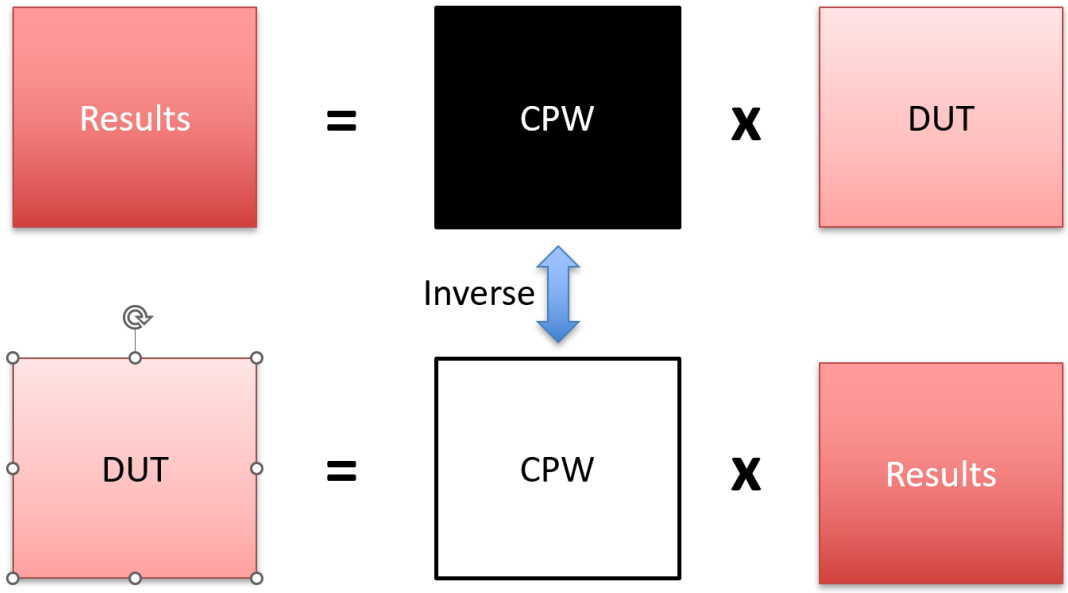

Figure 2-12 The principle of de-embedding.

Knowing that the results achieved by VNA are electronic behavior of CPW cascaded with DUT, in a de-embedding technique, CPWs with no device connected or few feature parts of CPWs (usually consisting of an open, short, and pad circuits, respectively) are fabricated and tested by VNA. Therefore, a matrix of the electronic behavior of CPW can be generated. Then, by multiplying the inverse CPW matrix and the results matrix, one can achieve the pure electronic performance of the DUT.

2.3 The State-of-art Development of FBARs

With the rapid development of modern telecommunication systems, FBARs with better performance are always in high demand. During the latest 20 years, great advancement has been made in the field of FBARs. Researchers and engineers have been keeping trying different technical approaches to introduce novel design, fabrication processes and new materials for advanced FBARs in order to achieve one or several of the following goals:

1. To increase the resonant frequency.

2. Increase the electromechanical coupling coefficient. (Increase the filter's bandwidth.)

3. Increase the quality factors and decreasing the insertion lose.

4. Suppress the spurious mode.

5. Simplify the design and fabrication process. (Reduce the cost.)

6. Develop additional functions. (Switchable and tunable FBARs.)

Several research directions have exhibited great potentials for the advancement of FBARs. The state-of-art development of FBARs is introduced as follows:

2.3.1 Introducing dopants to piezoelectric materials

AlN and ZnO are the most used conventional piezoelectric materials for FBARs. However, they have limited out-of-plane piezoelectric coefficient (around 7 pm/V and 11 pm/V,[44] respectively) and electromechanical coupling coefficient (around 6% and 4%,[44, 45] respectively). Fortunately, several researchers have found that doping Sc, Mg, Zr, Hf into AlN,[46-48] and Mg, Li into ZnO,[49-52] could make the crystal more 'asymmetric', as illustrated in Figure 2-13, increasing the piezoelectricity and electromechanical coupling coefficient of the doped piezoelectric materials.

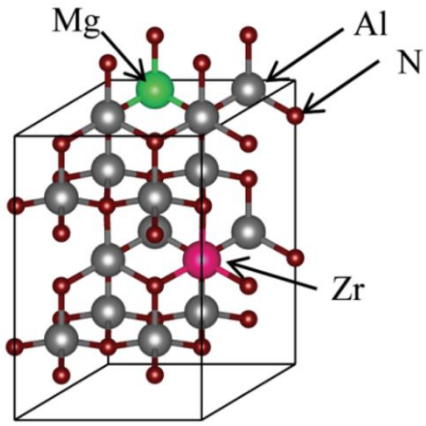

Figure 2-13 Atom structure of Mg, Zr doped AlN.[46]

Figure 2-13 showcases the doped AlN crystal with Mg and Zr by a triple-radio-frequency magnetron reactive co-sputtering system. Mg and Zr ions replace the Al ions in AlN crystal. The doped crystal with total Mg and Zr concentration of 35% exhibits an increase of out-of-plane piezoelectric coefficient d_{33} from ~5 pm/V to ~14 pm/V, and electromechanical coupling coefficient K_t^2 from 7.1% to 8.5%.[46] Similarly, a Mg doped ZnO film exhibits a raise of d_{33} from 12.4 pm/V to 41.7 pm/V with Mg molar fraction increasing from 0 to 30%.[53]

2.3.2 $LiNbO_3$ for FBARs

$LiNbO_3$ is considered to be the second generation of the piezoelectric materials used in FBARs, due to its good piezoelectricity, high electromechanical coupling coefficient and low cost.[54] The $LiNbO_3$ piezoelectric thin films fabricated by ion-implantation-exfoliation method can maintain their piezoelectricity with thickness of sub-micro. This piezoelectric thin film has attracted many attentions in recent years in the field of acoustic wave resonators. A typical ion-implantation-exfoliation fabrication process is shown in Figure 2-14.

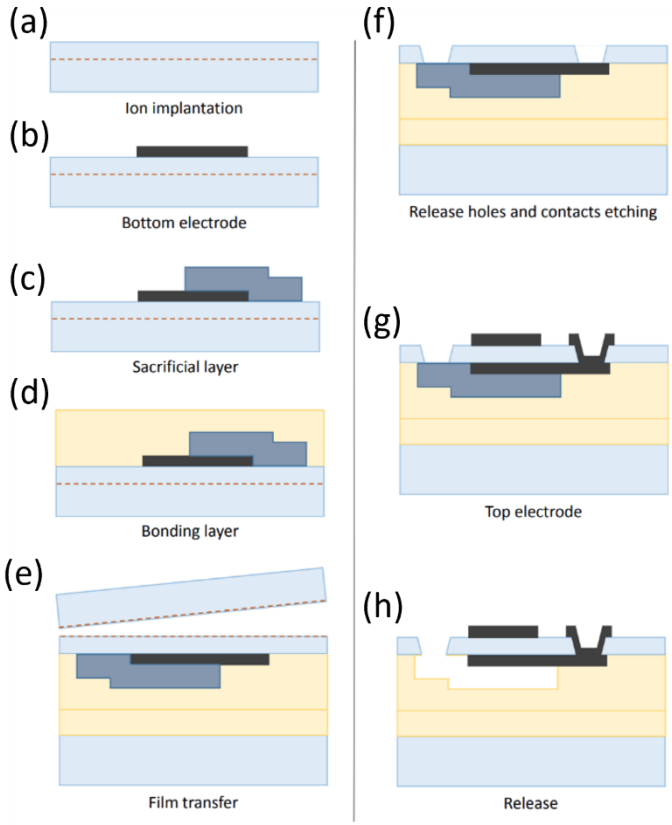

Figure 2-14 Fabrication process of $LiNbO_3$ based FBAR[55]

An X-cut $LiNbO_3$ wafer was ion-implanted (Figure 2-14 (a)), forming a weak interface at submicron meter beneath the top surface. Then the bottom electrode and sacrificial layer were deposited sequentially on the $LiNbO_3$ wafer (Figure 2-14 (b-c)). A bonding layer were attached to the wafer (Figure 2-14 (d)). Then the $LiNbO_3$ was physically exfoliated along the weak interface (Figure 2-14 (e)). After that, the release holes and contacts were defined (Figure 2-14 (f)) and the top electrode was deposited (Figure 2-14 (g)). Lastly, the sacrificial layer was removed by wet etching to form an air-cavity (Figure 2-14 (h)). The top view of the fabricated device is shown in Figure 2-15 (a), where the release holes, the cavity can be seen.[55]

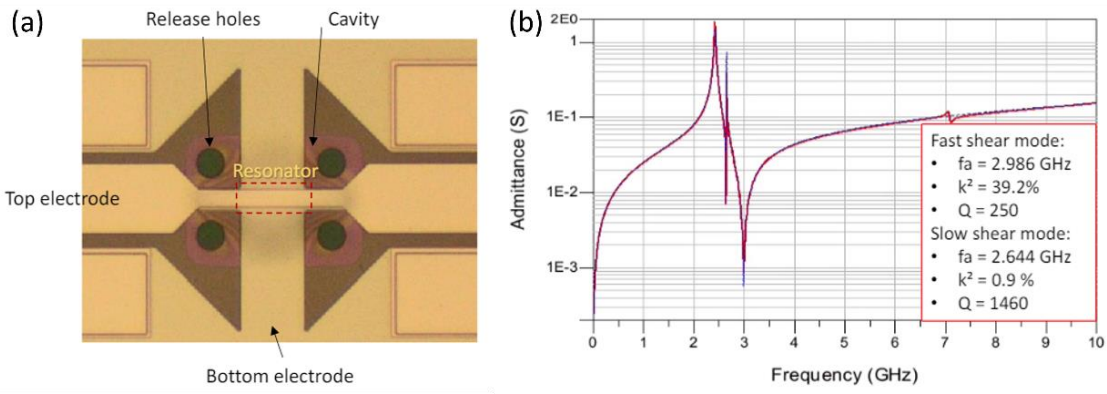

Figure 2-15 (a) Top optical view and (b) The electronic performance of the $LiNbO_3$ based FBAR.[55]

f_r of 2.4 GHz and a remarkable high K_t^2 of 39.2% as shown in Figure 2-15 (b) were obtained from a $LiNbO_3$ based FBAR.

Besides the thickness shear mode generated by out-of-plane electric field on X-cut $LiNbO_3$ thin film, recent study found that 128°Y-cut $LiNbO_3$ thin film are very promising for generating thickness shear mode by lateral-field excitation.[56] And those devices are called XBARs which will be discussed later in this chapter.

2.3.3 OBARs

Because of the inversely proportional relationship between the thickness of the piezoelectric layer and the resonant frequency of a FBAR, FBARs using the first order (fundamental) thickness extension mode (longitudinal mode) are usually with resonant frequencies below 10 GHz. (Significant degradation in the piezoelectricity of conventional piezoelectric materials occurs if their thickness is reduced to sub-micrometer.) To achieve higher resonant frequencies, some researchers make use of higher order modes of acoustic vibrations. The FBARs vibrate at overtone modes are called OBARs.[57, 58]

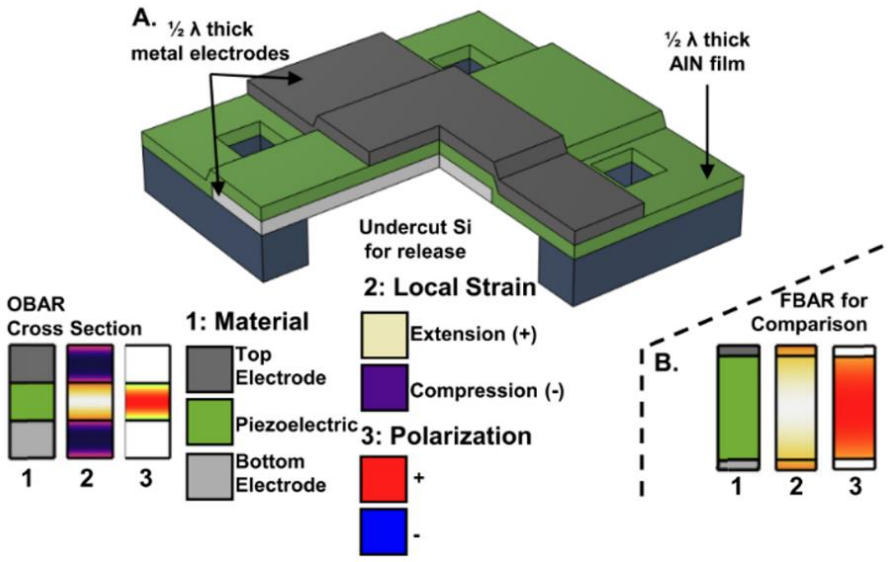

Figure 2-16 (a) Structure of a second overtone thickness extension mode bulk acoustic wave resonator with cross section views colored by 1. material, 2. local strain, and 3. polarization. (b) FBAR cross section view for comparison.[59]

Figure 2-16 (a) shows the structure of a second overtone thickness extension mode FBAR.[54] The AlN piezoelectric layer and two electrodes' thickness were precisely controlled to match with half of the wavelength of the acoustic wave, respectively, achieving the conditions under which the third overtone vibration mode was enhanced. Therefore, unlike the FBARs resonate at fundamental modes as shown in Figure 2-16 (b), where half of the wavelength travels inside the thickness of electrodes and the piezoelectric layer each time, an OBAR resonates at higher order of harmonic modes where one and a half of the wavelength travels inside the thickness of electrodes and the piezoelectric layer each time. (2/3 of the acoustic path length is in the electrodes)

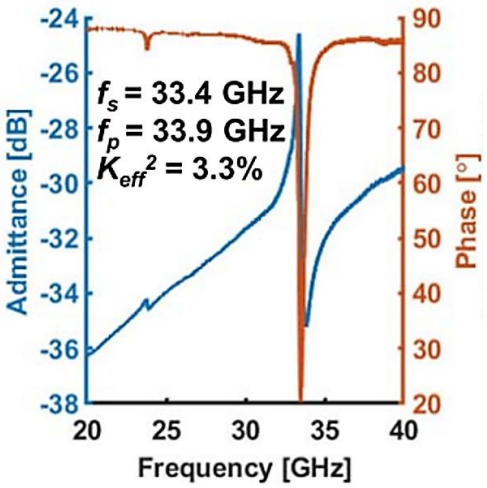

Figure 2-17 Measured performance of the OBAR.[59]

As shown in Figure 2-17, the f_r and f_a of the OBAR are at 33.4 GHz and 33.9 GHz, respectively. A phase change from conductive towards inductive can be observed. K_t^2 of 3.3% is achieved.[59]

OBAR is one effective way to achieve higher resonant frequencies without thinning the thickness of the piezoelectric materials. However, even carefully designed, the higher harmonic resonance modes are still much weaker than the fundamental mode, leading to lower Q and K_t^2. Additionally, due to the existence of the fundamental mode and other spurious modes, the filter has other passbands besides the desired higher harmonic resonance mode. To filter out those unwanted passband signals, more filters should be cascaded for the application. This significantly limits OBARs' application.

Besides OBARs with thickness extension modes, OBARs with lateral-field-excited thickness shear modes and lamb modes have also attracted many attentions.

2.3.4 XBARs

Conventional FBARs use the thickness extension mode of the piezoelectric layer in-between the top and bottom electrodes. In this case, three-layers (at least three masks) fabrication process should be implemented to deposit the bottom electrode, piezoelectric layer, and top electrode. Since 1990s, lateral-field-excited thickness shear mode and lamb mode have been utilized to form the resonances, and the lateral field-excited FBARs are called XBARs. Instead of clamping piezoelectric material between two

electrodes (Figure 2-18 (a)), XBARs only have electrodes deposited on the surface of the piezoelectric material (Figure 2-18 (b)). Usually, the electrodes are in the shape of IDTs (interdigital transducers) like SAW devices or just two square pads. Lateral electric field formed by the electrodes generates the piezo induced strains of the piezoelectric material, forming vibrations.

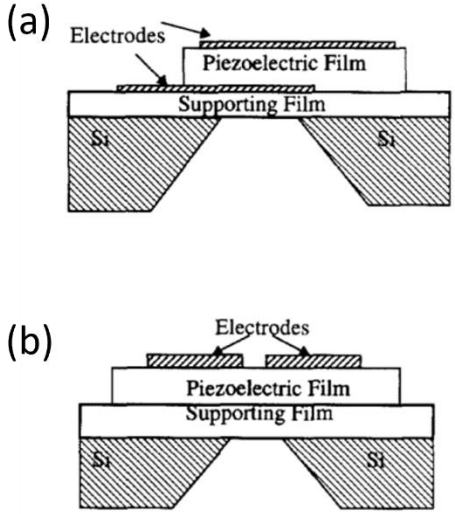

Figure 2-18 Structure of (a) thickness field excited and (b) lateral field excited FBAR. (c) 3D view and cross-section view of an IDTs excited FBAR.[60, 61]

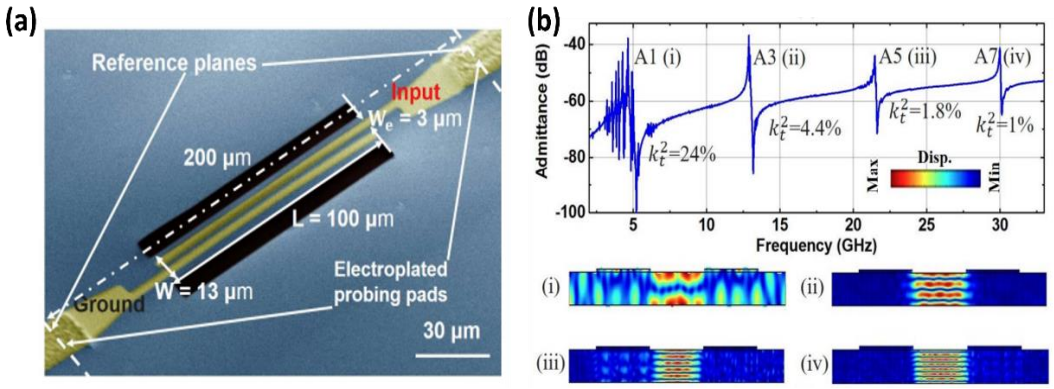

Figure 2-19 (a) Top view of an XBAR with two pads of electrode above the piezo layer. (b) Electronic performance of the XBAR with the motion of (i) A1, (ii) A3, (iii) A5, (iv) A7 mode.[62]

Figure 2-19 (a) shows an XBAR consisting of two pads of electrodes deposited on a Z-cut $LiNbO_3$ piezoelectric layer. The electric field between two electrodes excited the vibration with asymmetric modes. According to Figure 2-19 (b), this XBAR could vibrate at 4.5, 12.9, 21.4, 29.9 GHz with corresponding K_t^2 of 24%, 4.4%, 1.8% and 1%, respectively. From the simulated motion diagram one can see the fundamental thickness

shear mode (A1) at the resonance frequency of 4.5 GHz and higher overtone modes as well (A3-A7).[62]

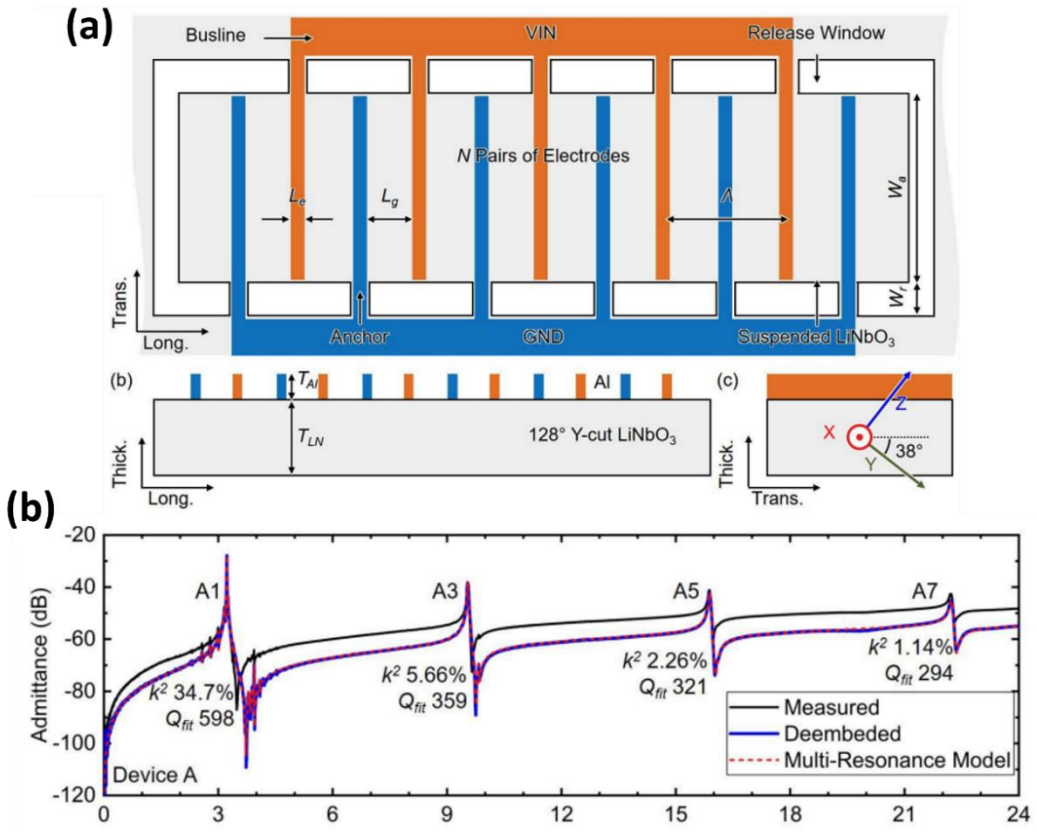

Figure 2-20 (a) Schematic top view of an XBAR with IDT on 128° Y-cut $LiNbO_3$. (b) The electric performance of the XBAR.[56]

Figure 2-20 (a) shows an XBAR consisting of an interdigital transducer (IDT) deposited above a 128° Y-cut $LiNbO_3$ piezoelectric layer. This XBAR mainly vibrates at 3.22, 9.55, 15.9 and 22.2 GHz with corresponding K_t^2 of 34.7%, 5.66%, 2.26% and 1.14%, respectively.[56]

XBAR technique largely simplifies the fabrication processes and increases the freedom of design. The designers can simply tune the shape, size, width, length of the electrodes to control the expected vibration modes and resonant frequencies with the piezo layer remaining unchanged. Additionally, with the development of the material science, the performance of XBAR is found to be enhanced with a certain piezoelectric material along a specific cutting angle.[56, 62, 63]

2.3.5 Tunable and switchable FBARs

A tunable FBAR can adjust its resonant frequency to meet specific needs. A switchable FBAR can be turned on/off in response to the external controls. Nowadays, telecommunication modules inside modern mobile phones and other multi-input multi-output (MIMO) systems are required to work in different frequency bands. Therefore, tens of filters with different center frequencies are usually integrated with extra duplexer control circuits to achieve this, leading to large size, high complexity, power consumption and cost of the module.[64] An ideal approach to reducing the complexity of the front-end communication module is to replace those filters with different center frequencies with the filters whose center frequencies can be reconfigured according to different working requirements and can be easily turned on/off.[65] As a result, high switchability and tunability of FBARs are in strong demand for advanced multi-band wireless communication systems, including 5G and beyond, and other specific systems where precise and adaptive frequency control is needed.[66, 67]

Generally, the switchability and tunability of a FBAR can be extrinsic and intrinsic. Intrinsic switchability and tunability involve the use of materials that can change their properties in response to external stimuli. For example, ferroelectrics in their ferroelectric and paraelectric phases are used because they can be tuned by applying an electric field. Extrinsic switchability and tunability employ external components like varactors and inductors to modify the resonant frequency and control the on/off behavior.

The extrinsic approaches usually reduce the quality factors of a FBAR and increase the complexity of the whole circuit, which highly limit their applications. As a result, the intrinsic switchability and tunability through the ferroelectric materials controlled by external electric field is the most promising approach.

AlN has been the most conventional piezoelectric material for FBARs. Although AlN is considered as a soft ferroelectric material (very hard to switch), it can become tunable and switchable if doped properly.

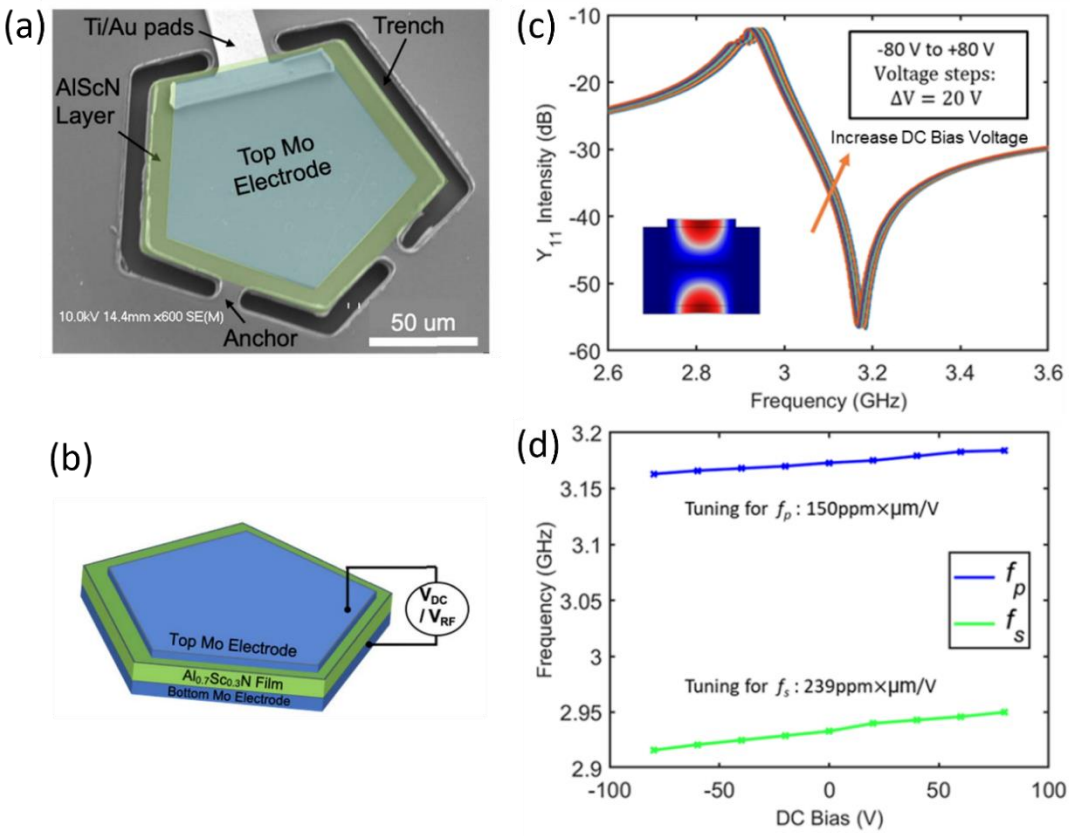

Figure 2-21 (a) Top view and (b) 3D schematic view of the AlScN based switchable and tunable FBAR. (c) Conductivity frequency response under different DC bias. (d) Frequency tuning versus DC bias.[68]

As shown in Figure 2-21 (a) and (b), a Sc doped AlN ($Al_{0.7}Sc_{0.3}N$) based FBAR with a pentagonal shape can function as a tunable and switchable FBAR. Surrounding trenches were made as via holes for etchant, forming an air cavity below the FBAR. A DC bias with RF excitation signal fed through the top and bottom Ti/Au electrodes of the FBAR. According to Figure 2-21 (c) and (d), this tunable Sc-doped AlN based FBAR with the center frequency near 2.93 GHz was of a tuning frequency window of 34 MHz under a bias ranged from – 80 V to 80 V, yielding a turning efficiency (i.e., the tuning frequency window divided by the voltage range) of 0.2 MHz/V and a tunability (i.e., the tuning efficiency divided by the center frequency) of 0.007%/V. Additionally, this FBAR could be switched off by a DC bias of 350 V.[68]

To achieve higher tunability, barium strontium titanate (BST) has been engaged due to its high electric-field-dependent permittivity and electric-field-induced piezoelectricity.[69]

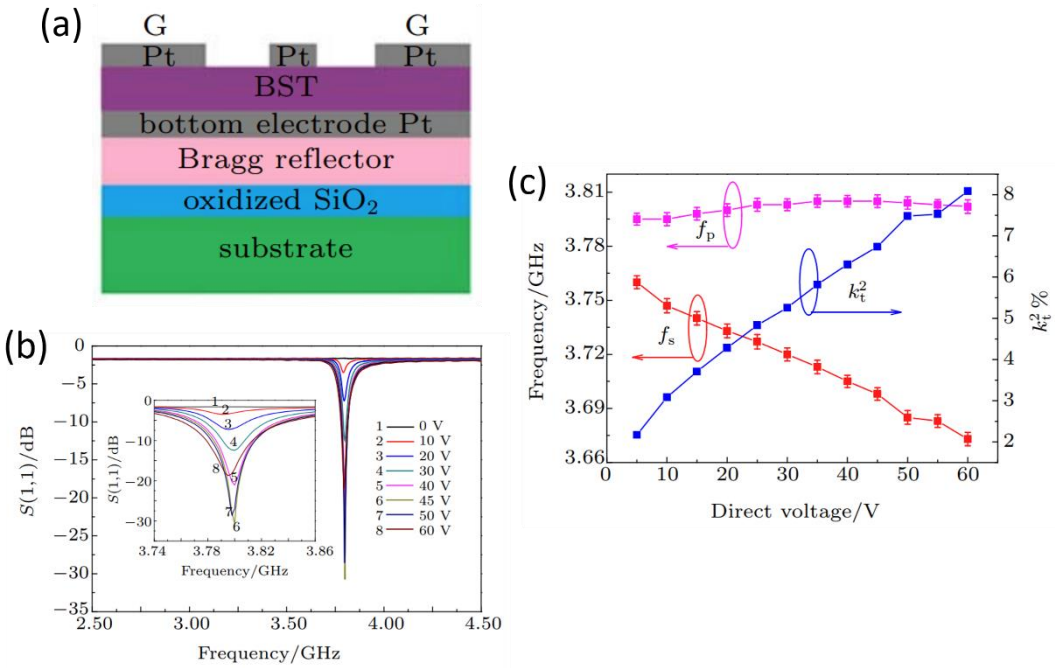

Figure 2-22 (a) Schematic diagram of the BST based FBAR. (b) Frequency response under different DC bias from 0 to 60 V. (c) Frequency tuning versus DC bias.[70]

Figure 2-22 (a) shows the structure of a BST based tunable and switchable FBAR. A 530 nm thick BST thin film was clamped by two Pt electrodes. A Bragg mirror reflector consisting of Mo and SiO_2 were fabricated forming a structure of SMR. The S_{11} parameter versus the DC bias voltage is shown Figure 2-22 (b). The S_{11} equal to 0 when no bias was applied, while S_{11} peak became deeper gradually when DC bias increased from 10 to 45 V. This BST based normally-off solid mounted resonator exhibited a tuning frequency window of ~87 MHz with DC bias from 5 V to 60 V (1.6 MHz/V) and a tunability of 0.04%/V at the center frequency of 3.76 GHz as shown in Figure 2-22 (c).[70]

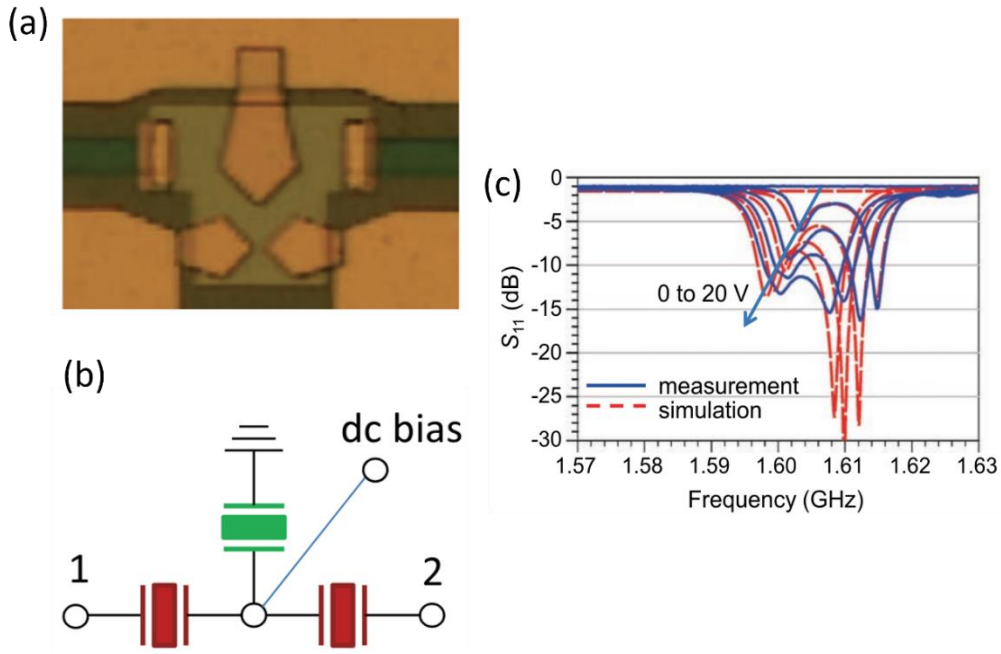

Figure 2-23 (a) A filter consists of three BST based FBARs. (b) Schematic diagram of the filter and the DC bias input port. (c) Frequency response under different DC bias from 0 to 20 V.[71]

Figure 2-23 (a) and (b) shows a filter consisting of three BST based tunable and switchable FBARs. The DC bias was applied to the common electrode of those FBARs. From Figure 2-23 (b) one can see the pass band of the filter was tuned to lower frequency end and the insertion loss decreased when the applied DC bias voltage increased from 0 to 20 V.[71]

2.4 Limitations of Conventional FBARs

Wireless communication technology has come a long way since the early days of analog cell phones and 2G networks. Today, with the advancement of 5G and 6G technology, the sub-6 GHz band become more and more crowded, the demand for communication devices working on high frequency band are growing rapidly. This requires FBARs to possess higher resonant frequencies. However, for FBARs based on conventional piezoelectric materials such as AlN, PZT, ZnO, the resonant frequencies can hardly exceed sub-6 GHz band. This is because that the resonant frequencies in sub-6 GHz band requires submicron thick conventional piezoelectric materials (Equation 2.3). Unfortunately, the conventional materials are hard to maintain their piezoelectricity

when their thickness is below submicron, mainly because of two reasons. One is the limitation of material deposition process. For the grown AlN thin film, first a few hundreds of nanometers thick AlN is nearly amorphous. AlN with the C axis dominants the structure only when the thickness is largen than a few hundreds of nanometers.[21, 72] The other one is the defects near the surface and the surface roughness scatter on acoustic wave propagation.

Although a few new technical approaches, like implantation of ion-implantation-exfoliation fabrication process and OBAR mentioned above have demonstrated to break through the limitation, they all have their drawbacks. The ion-implantation-exfoliation method could create submicron thick $LiNbO_3$ or $LiTaO_3$ so far, the surface defects and rough surface caused by the ion-implantation-exfoliation lead to significant acoustical scattering. OBARs use the high order of overtone modes which are usually weaker compared to the fundamental mode. Overtone modes usually possess smaller K_t^2 and Q. Additionally, due to the existence of the fundamental mode and other spurious modes, the filter has multiple passbands.

Despite the DC bias controlled tunable and switchable FBARs which introduce a lot of flexibilities in circuit design, the reported devices typically suffer from low tuning efficiency and very high off-voltage. For the BST based normally-off tunable and switchable FBARs, they have to be used as active devices rather than passive ones.

Due to the prementioned limitations of the conventional FBARs, FBARs based on novel piezoelectric materials with high performance are in high demand. Luckily, recent developments of two-dimensional (2D) piezoelectric materials create new opportunities in this perspective. Few 2D piezoelectric materials, such as In_2Se_3, 3R-MoS_2, CIPS ($CuInP_2S_6$), have been theoretically predicted and experimentally proved to possess strong piezoelectricity.[27, 29, 73] Those atomic flakes show piezoelectricity with thickness even down to one atomic layer.

2.5 Two Dimensional Piezoelectric Materials

Study of 2D piezoelectric materials for acoustic devices is motivated by their promising applications in a variety of fields such as flexible electronics, sensors, and energy harvesting devices. The capability to fabricate these materials at the nanoscale allows them to be integrated into micro-electromechanical systems (MEMS), where traditional bulk piezoelectric materials are not easily utilized.

2.5.1 Study of the piezoelectricity in 2H-MoS_2 and 3R-MoS_2

MoS_2 is a transition metal dichalcogenide (TMD) that consists of adjacent layers of molybdenum atoms sandwiched between two layers of sulfur atoms bonded by vdWs force. There are three phases of MoS_2, 1T, 2H and 3R. The atomic structures of the three phases are shown in Figure 2-24 (a). The 1T phase has octahedral coordination of Mo atoms, while each Mo atom is surrounded by six sulfur atoms in a distorted octahedral geometry. The 1T phase is a metallic phase and it is non-piezoelectric. The 2H phase is the most stable and common crystalline form of MoS_2 at ambient conditions. It has trigonal prismatic coordination of Mo atoms, while each Mo atom is surrounded by six sulfur atoms in a trigonal prism arrangement. 2H phase MoS_2 exhibits non-centrosymmetric atomic structure. The in-plane piezoelectricity of 2H-MoS_2 was studied by measuring the piezo response of the 2H-MoS_2 device shown in Figure 2-24 (b).[74] A 2H-MoS_2 flake was placed onto a flexible substrate, while two electrodes were deposited along the armchair direction of the 2H-MoS_2 flake. Figure 2-24 (c) shows the operation of the piezoelectric device. When the device is bended, the 2H-MoS_2 flake is stretched, piezo charges are shown up at the two ends, inducing a current in the circuit.

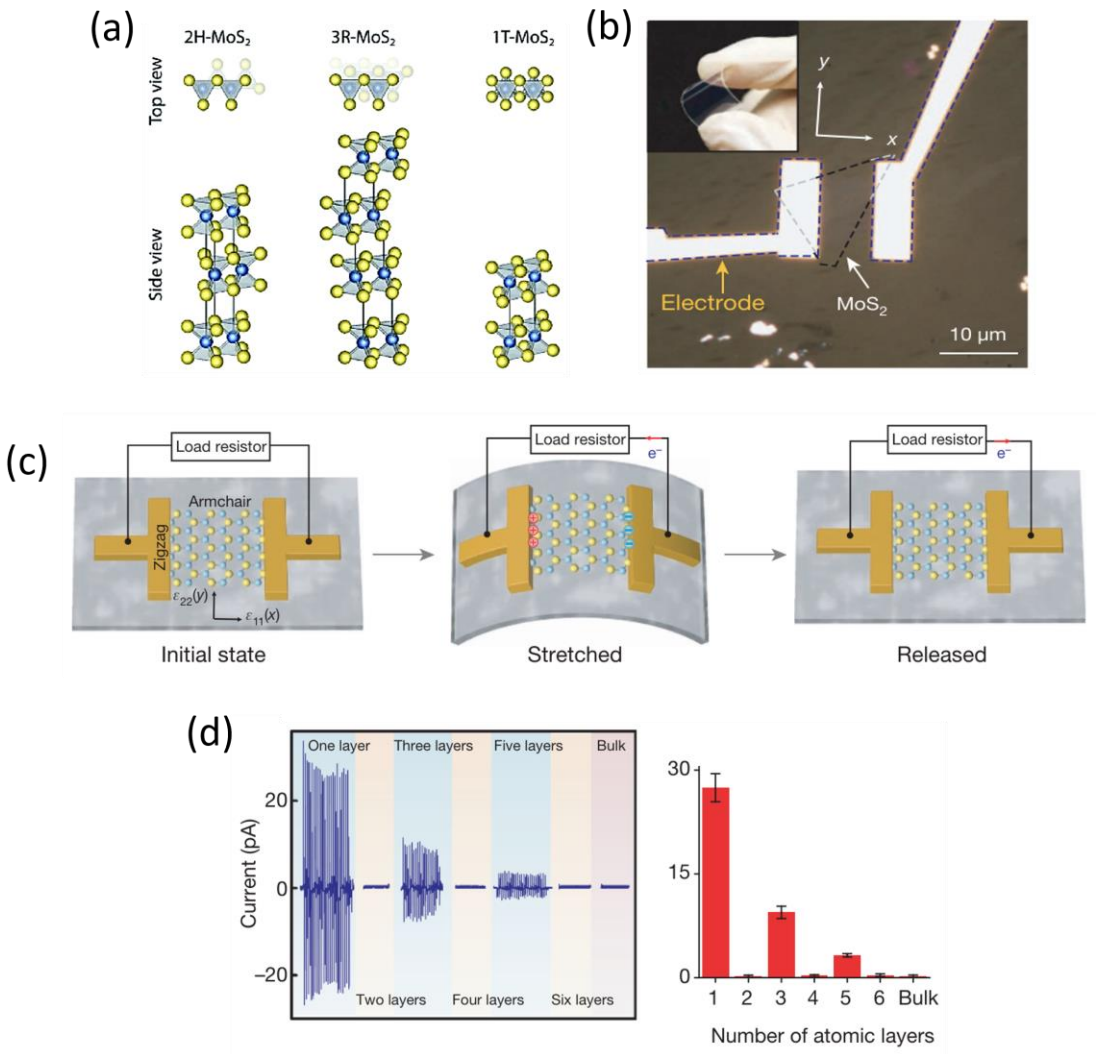

Figure 2-24 (a) Atomic structures of 1T, 2H, 3R phase of MoS_2. (b) Top view of 2H-MoS_2 placed between two electrodes on a flexible substrate. (c) Operation scheme of the 2H-MoS_2 piezoelectric device. (d) Piezoelectric output of the 2H-MoS_2 with different number of atomic layers.[74]

The piezo response of the device based on 2H-MoS_2 flake with different number of atomic layers is shown in Figure 2-24 (d). For 2H-MoS_2 flakes with odd number of layers, i.e., monolayer, three layers, and five layers, the piezo response can be detected. It was found that the piezo response decreased with the increase of the layer numbers. The 2H-MoS_2 flakes with even number of layers did not induce a detectable current, suggesting that 2H-MoS_2 flakes with odd layer numbers possess piezoelectricity while with even layer numbers and bulk are non-piezoelectric. This is because the adjacent layers of 2H-MoS_2 have opposite direction of crystalline orientations and cancel out the in-plane piezoelectricity of each other. [74]

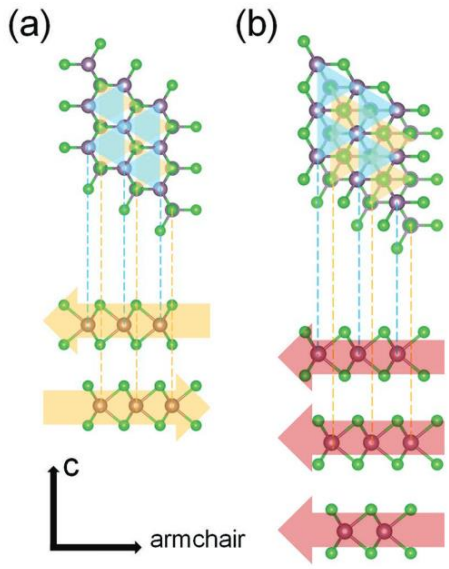

Figure 2-25 Top view and side view of atomic structure of (a) 2H-MoS_2 and (b) 3R-MoS_2.

Most of 2D piezoelectric materials possess this odd-even effect, which significantly limited their applications. Luckily, 3R-MoS_2 and α-In_2Se_3 are theoretically predicted and experimentally proved to possess piezoelectricity, regardless of the number of the atomic layers. The top view and side view of the atomic structure of 2H-MoS_2 and 3R-MoS_2 are shown in Figure 2-25. Unlike 2H-MoS_2, for 3R-MoS_2, three adjacent atomic layers are aligned in the same direction with a shift relative to each other, described as the ABC-ABC stacking order. Consequently, the broken inversion symmetry could be maintained from bilayer to multilayers.

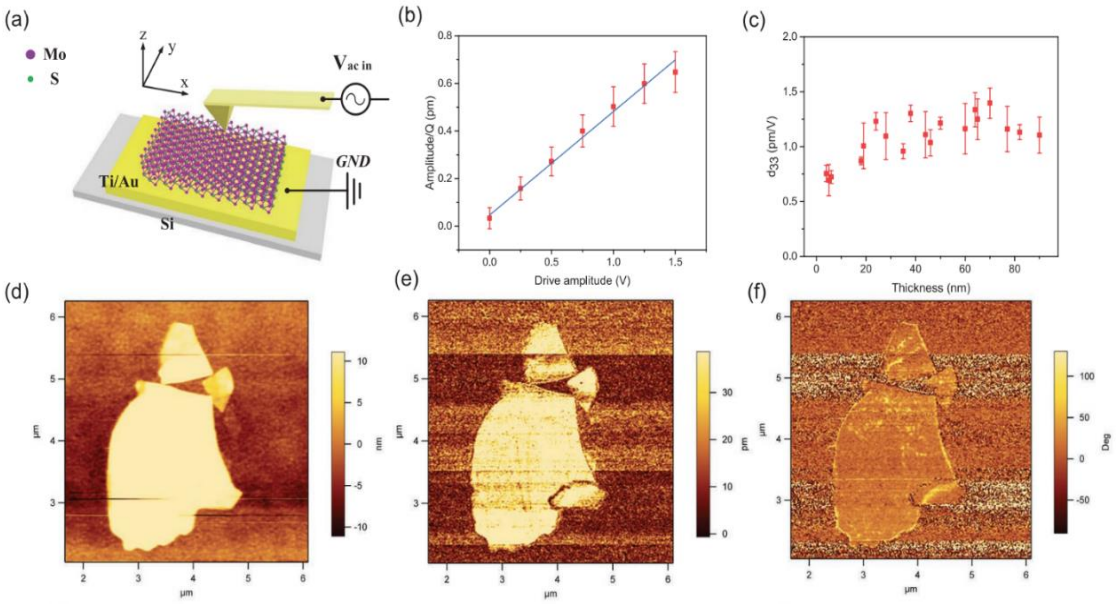

Figure 2-26 Out-of-plane piezo response study of 3R-MoS_2. (a) Schematic of PFM measurement set-up of out-of-plane piezoelectric coefficient d_{33}. (b) Out-of-plane piezo response amplitude for an 18 nm thick 3R-MoS_2 flake as a function of ac voltage applied. (c) Out-of-plane piezoelectric coefficient d_{33} as a function of 3R-MoS_2 flakes' thickness. (d) The AFM topography of the 18 nm thick flake. (e, f) Piezo response amplitude and phase, respectively, of the 18 nm thick flake in (d) at a bias of 0.75 V.[29]

The out-of-plane piezoelectricity of 3R-MoS_2 flakes was studied using Piezo-response Force Microscope (PFM). An exfoliated 3R-MoS_2 flake was transferred onto a Si substrate coated with Ti/Au conductive layer. The Ti/Au layer was connected to the ground while an alternative voltage was applied on the conductive PFM tip, which was landed on the flake, forming an out-of-plane ac bias across it. Due to the out-of-plane piezoelectricity of 3R-MoS_2, vertical displacement was detected up on a bias voltage was applied between the tip and the Ti/Au layer, as shown in Figure 2-26 (a).[29] The out-of-plane displacement of the flake can be calculated by the out-of-plane displacement amplitude of the tip divided by the sensitivity of the tip, and it was proportional to the amplitude of the ac bias applied, see Figure 2-26 (b). Out-of-plane piezoelectric coefficient d_{33} was not sensitively dependent with the film thickness. For 3R-MoS_2 flakes with thickness under 100 nm, the out-of-plane piezoelectric coefficient was measured to be from 0.7 ± 0.2 pm/V to 1.5 ± 0.2 pm/V, see Figure 2-26 (c). The thickness of the flake was measured from the topography of the flake, see Figure 2-26 (d). The PFM measurement results of amplitude and phase of the piezo response in Figure 2-26 (e,f) show clearly the out-of-plane displacement of the 3R-MoS_2 flakes generated by the vertical bias.[29]

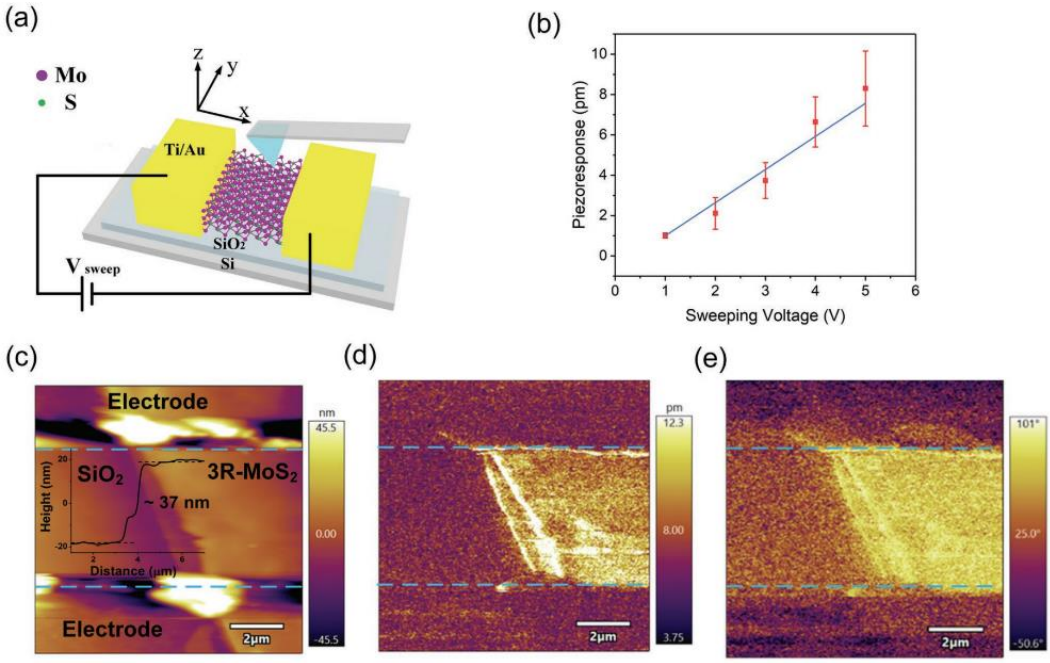

Figure 2-27 In-plane piezo response study of 3R-MoS_2. a) Schematic of PFM measurement set-up of in-plane piezoelectric coefficient d_{13} b) In-plane piezo response amplitude for a 37 nm thick 3R-MoS_2 flake as a function of lateral ac voltage applied. c) The AFM topography of the 37 nm thick flake between two electrodes. d, e) Piezo response amplitude and phase, respectively, of the 37 nm thick flake in (c) under a lateral ac bias of 3.0 V.[29]

The in-plane piezoelectricity of 3R-MoS_2 is also characterized using PFM, as shown in Figure 2-27. An exfoliated 3R-MoS_2 flake was transferred onto a Si substrate with a SiO_2 surface layer. Two Ti/Au electrodes were deposited at two ends of the 3R-MoS_2 flake. Ac voltage was applied between the two electrodes, the applied lateral electric field induced an in-plane strain, leading to an out-of-plane displacement which was detected by an AFM tip, as illustrated in Figure 2-27 (a). The in-plane strain of the flake was proportional to the amplitude of the ac bias applied (Figure 2-27 (b)). The piezoelectric coefficient d_{13} of a 37 nm thick 3R MoS_2 flake was estimated around 1.64 ± 0.16 pm/V. The flake buried by two electrodes (Figure 2-27 (c)) was characterized by PFM. The amplitude and phase of the piezo response in Figure 2-27 (d, e) show clearly the out-of-plane displacement of the 3R-MoS_2 flakes generated by the lateral bias. [29]

2.5.2 Study of the piezoelectricity in α-In_2Se_3

α-In_2Se_3 is another material that exhibits piezoelectricity regardless of the number of the atomic layers. An α-In_2Se_3 flake is constructed from a space group $P6_3mc$ with hexagonal stacking (2H). Adjacent Se-In-Se-In-Se quintuple layers with a 60 degree in-plane rotation are bonded by vdWs force. The non-symmetric atomic structure contributes to the piezoelectricity of α-In_2Se_3.

The out-of-plane and in-plane piezoelectricity were studied by PFM. The α-In_2Se_3 flakes were transferred onto an Au coated Si substrate. For out-of-plane piezoelectricity measurement, an AC signal was applied to the conductive PFM tips to generate the out-of-plane piezo response of the material under test. The d_{33} was characterized by the displacement sensed by the bending of the PFM cantilever under vertical PFM mode. For in-plane piezoelectricity measurement, the sample was placed between two electrodes which provide the AC lateral electric field. In-plane piezo response of the material under test was excited by the lateral electric field. And the in-plane displacement was characterized by the twisting of the PFM cantilever under lateral PFM mode.

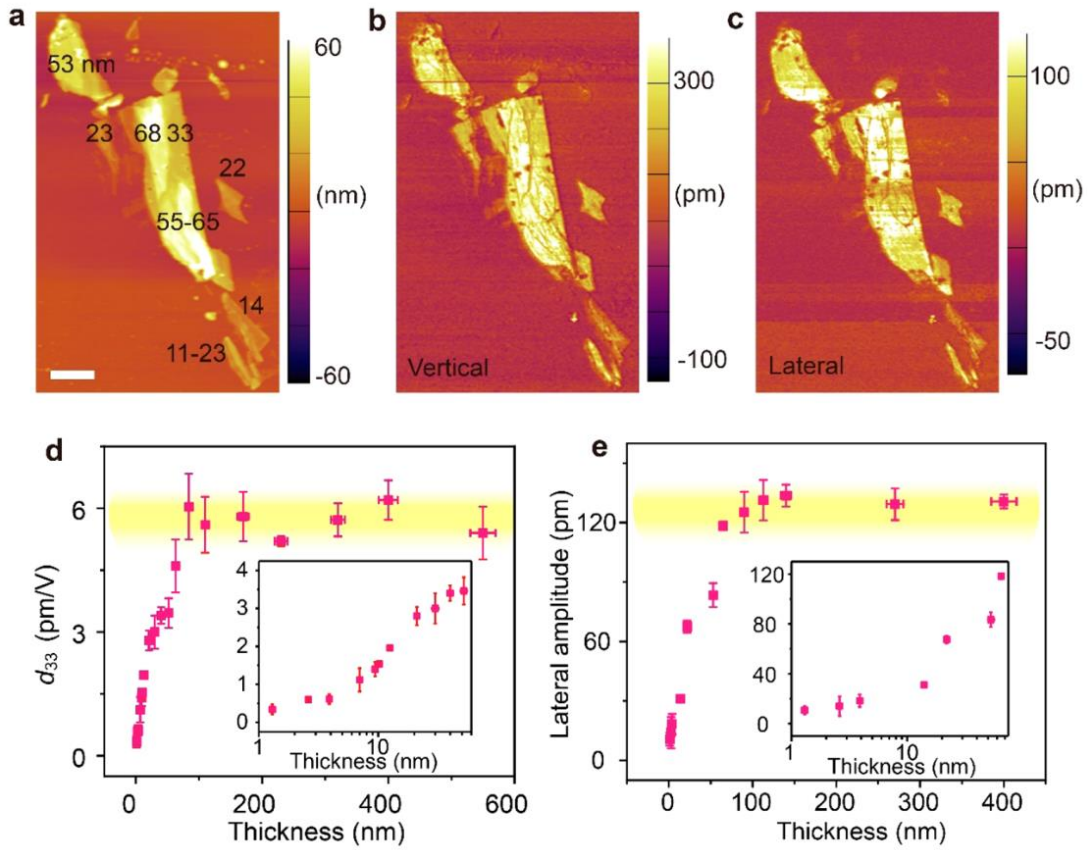

Figure 2-28 Piezo response study of α-In_2Se_3. (a) Topology of the α-In_2Se_3 flakes under test. (b) Out-of-plane piezo response amplitude for the α-In_2Se_3 flakes. (c) In-plane piezo response amplitude for the α-In_2Se_3 flakes. (d) d_{33} values as function of the film thickness. (e) lateral amplitude values as function of the film thickness.[26]

Figure 2-28 (a) is an AFM image of few α-In_2Se_3 flakes with different thickness. Figure 2-28 (b) and (c) are the vertical and lateral piezo response of the α-In_2Se_3 flakes, respectively. The d_{33} values were found to increase with the increase of the thickness till 90 nm, as shown in Figure 2-28 (d). When the thickness was larger than 90 nm, the d_{33} value saturated at a value of 5.6 pm/V.

The lateral piezoelectric response amplitude as function of the film thickness is shown in Figure 2-28 (e). Because of the coupling between the two-perpendicular piezoelectricity, accurate value of d_{11} cannot be achieved. But from the amplitude versus thickness shown in Figure 2-28, one can see that the in-plane piezoelectricity of α-In_2Se_3 increases in the same way with the sample thickness and saturates at around 90 nm. [26]

2.5.3 Challenges for Devices based on 2D Materials

It is worth pointing out that even plenty of individual devices made in laboratory based on 2D materials have exhibited excellent performance, engineering a consistent, reproducible platform of 2D materials at industrial scales is still facing significant challenges. Firstly, most of the 2D nano sheets are made by physically exfoliation method from a bulk crystal. Therefore, their thickness and uniformity are largely random. Additional processes should be conducted to choose the suitable flakes. Secondly, large-scale growth of 2D materials on Si wafer is still facing difficulties. Many 2D materials are synthesized on non-native substrates. As a result, transfer processes of the grown films towards targeted substrates are always required, which may introduce wrinkles, cracks, residues, and delamination. Additionally, achieving uniform doping profiles across a large substrate and ensuring process stability are significant challenges for 2D materials. All those factors limit the mass production of the devices based on 2D materials.

Development of FBARs based on 2D materials developed and reported in this thesis also faced the above challenges. Even if they could be reproduced in the laboratory, a lot of processes are involved. In other words, 2D-based FBARs reported in this thesis serve as the proof of the concept.

2.6 Summary

Chapter Two provides an overview of the fundamental theory and recent advancements related to FBARs. A FBAR consists of a piezoelectric layer placed between two electrodes, generating longitudinal acoustic waves that travel through its bulk. The resonance occurs at specific frequencies depending on the thickness of the piezoelectric layer. Conventional piezoelectric materials face significant challenges in maintaining their piezoelectricity when made ultrathin, significantly limiting the resonant frequencies of FBARs based on them. Several methods have been developed to improve the performance of FBARs, but each of these approaches has its own limitations. Introducing dopants to AlN and ZnO can increase their asymmetric and consequently increase the K_t^2 of the FBARs. However, this method has a very limited impact on

raising the resonant frequency. Using $LiNbO_3$ thinned down by ion-implantation-exfoliation process can effectively increase the resonant frequencies of the FBARs, but the process also introduces large defects, surface roughness and dangling bond at the interface. OBARs use high-order vibration modes to achieve resonance at ultrahigh frequencies; however, high-order resonances are usually much weaker than the fundamental mode. Additionally, extra filters are required to eliminate the passband caused by lower-order resonances.

According to recent studies, including our own, 2D piezoelectric materials such as 3R-MoS_2 and α-In_2Se_3 can maintain their piezoelectric properties even when reduced to a monolayer. As a result, embedding ultrathin 2D nanoflakes shows great promise for achieving FBARs with ultrahigh resonant frequencies. However, no related studies have been reported so far. The main results achieved in this PhD project are summarized in Chapters 3-6.

Chapter 3 Methodology and Experiment Set-up of Piezoelectricity Characterization of Two-dimensional Materials and Device Fabrication

PFM is the mostly used method for characterizing piezoelectricity in 2D materials because of its good sensitivity for nano-scale effects and its ability to provide high-resolution, localized measurements. In this PhD project, we utilized PFM technique to characterize the piezoelectricity/ferroelectricity of the 3R-MoS_2 flakes and the α-In_2Se_3 flakes. In this Chapter, we introduce the sample preparation process of 2D materials. The mechanism and experiment set-up of AFM/PFM characterization of the surface roughness and out-of-plane piezoelectricity/ferroelectricity of the 3R-MoS_2 flakes and the α-In_2Se_3 flakes are discussed.

3.1 Sample Preparation

Multilayers of 3R-MoS_2 flakes were fabricated using a physical exfoliation method from a bulk 3R-MoS_2 crystal provided by Prof Liu Zhen's group. The fabrication process is shown in Figure 3-1. A piece of bulk 3R-MoS_2 crystal was placed onto a segment of Scotch tape. (Figure 3-1 ①) Then this tape was folded and unfolded for several times so that the bulk materials could be peeled off into several thin flakes. (Figure 3-1 ②-③) Another segment of plain Scotch tape was attached to the tape with 3R-MoS_2 flakes. (Figure 3-1 ④) Then the two tapes were torn apart so that some thinner flakes with fresh surfaces would be peeled off from the flakes in ③. (Figure 3-1 ⑤-⑥) Single atomic layer and few layer 3R-MoS_2 flakes could be prepared by repeating this peeling off process.

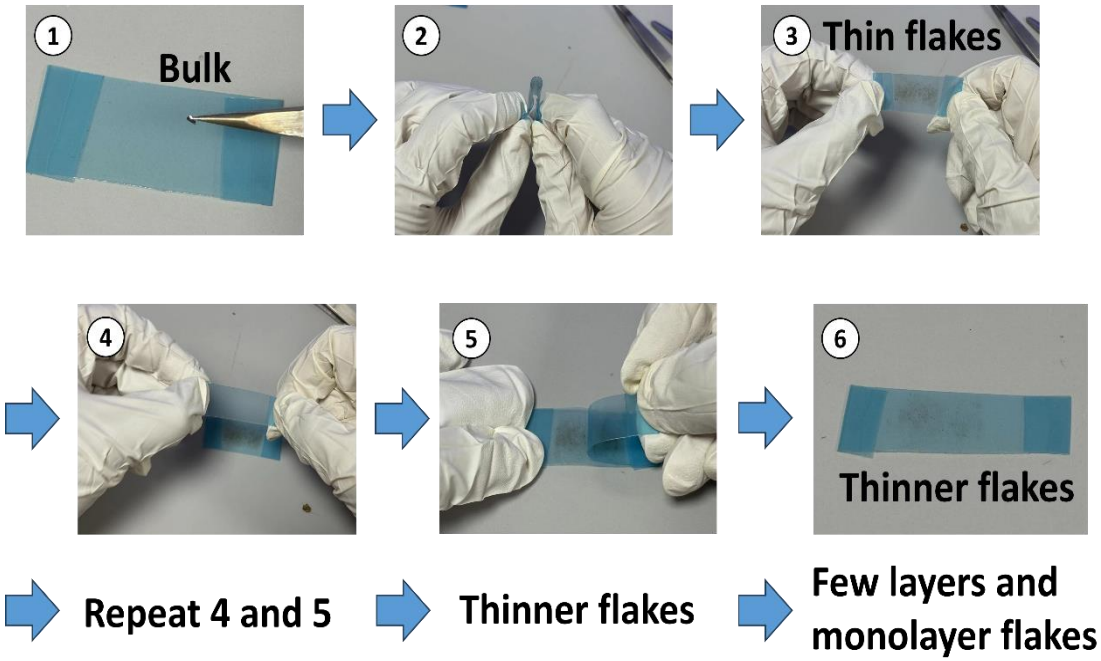

Figure 3-1 The fabrication process of 2D ultrathin flakes.

A conductive substrate was required to serve as the ground for PFM characterization. In most of experiments, the conductive substrates were made of doped Si wafers coated with 10 nm Ti and 50 nm Au through e-beam evaporation.

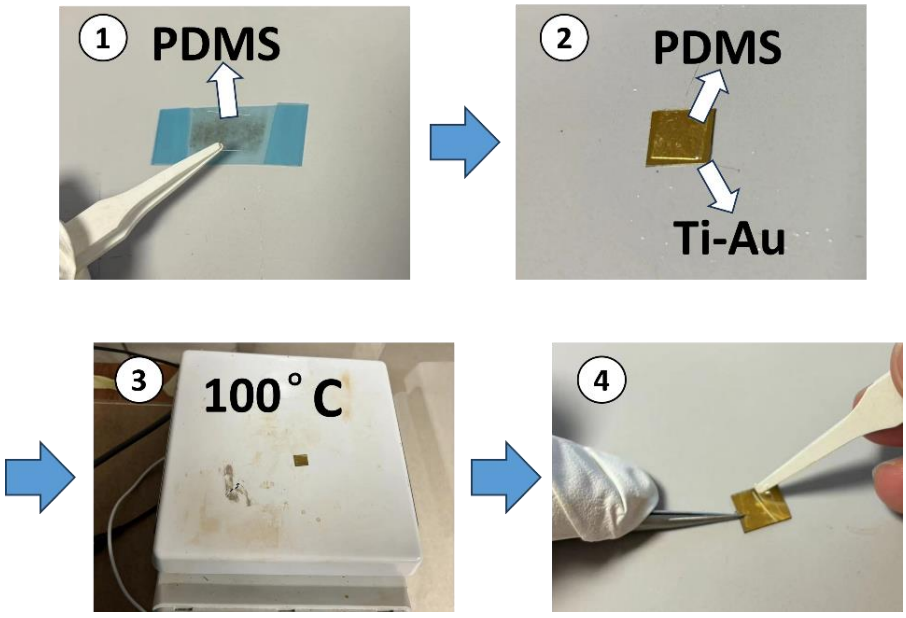

Figure 3-2 Transfer process of 2D flakes from Scotch tape to Ti-Au substrate.

To transfer the 3R-MoS_2 flakes onto a Ti-Au conductive substrate, those 3R-MoS_2 flakes fabricated by the above process were first transferred to a Gel-Pak PDMA polymer film (Figure 3-2 ①). The PDMS film with flakes were attached to the Ti-Au

substrate (Figure 3-2 ②). The whole stack was placed on a hot plate at 100°C, (Figure 3-2 ③) where the 3R-MoS_2 flake would be released from the PDMS film and attached to the Ti-Au substrate (Figure 3-2 ④). The ultrathin α-In_2Se_3 flakes were also prepared using the similar processes.

3.2 AFM Characterization

AFM is a powerful scanning probe microscopy that provides high-resolution imaging of the surface of the sample with a vertical resolution of the atomic scale. Its versatility and precision have made it indispensable in various fields, including materials science, biology, nanotechnology, and electronics.

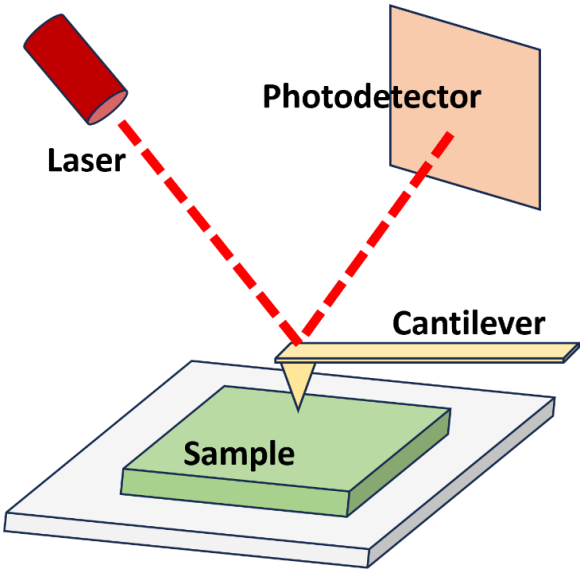

Figure 3-3 Basic component of an AFM.

Figure 3-3 shows the working principle and basic components of an AFM. The cantilever in AFM is a small flexible beam, usually made of silicon or silicon nitride, with a sharp probe at its free end. And the probe tip has a radius of curvature in the nanometer range. During measurement, the tip is brought close to the sample surface. The interaction force between the tip and sample surface leads to the bending of the cantilever. This deflection of the cantilever is characterized by a laser beam reflected off the back of the cantilever to a position-sensitive photodetector. Changes in the cantilever deflection cause a shift in the laser spot on the photodetector. The measured deflection directly reflects the topology of the sample.

For a FBAR device, the thickness of the piezoelectric layer directly determines its resonant frequency.[19] The roughness of the piezoelectric layer significantly influences the performance of the FBAR. Large roughness would lead to high acoustic energy loss and spurious resonance.[75] AFM technique is a powerful method in terms of accurate measurement of the thickness and surface roughness of the nanosheets. As a result, in this PhD project, the thickness and surface roughness of transferred 3R-MoS_2 flakes and α-In_2Se_3 flakes were characterized using AFM contact mode. Firstly, physically exfoliated 3R-MoS_2/α-In_2Se_3 flakes were transferred onto a flat substrate. A commercial PPP-CONTR tip fabricated by NANOSENSERS was attached to a tip holder, as shown in Figure 3-4 (a). The tip holder was then installed in an Asylum Cypher S AFM while the sample substrate was placed under the tip.

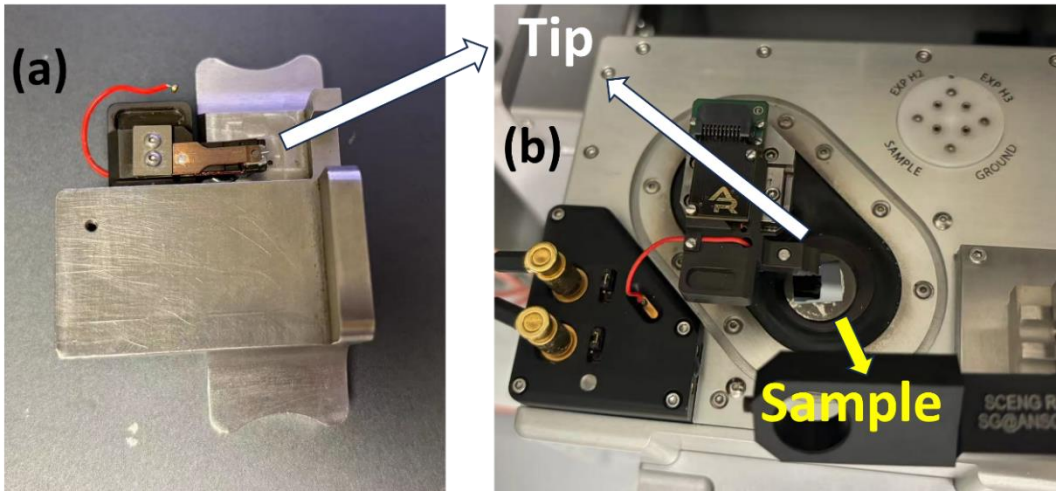

Figure 3-4 Experiment set-up of the AFM characterization. (a) Tip installation. (b) Top view of the sample under test.

3.3 PFM Piezoelectricity Characterization

A piezo-response force microscopy (PFM) is a variant of AFM used to investigate piezoelectric and ferroelectric properties of the sample. It operates by measuring the mechanical response of a sample to an applied AC voltage through a conductive AFM tip as shown in Figure 3-5.

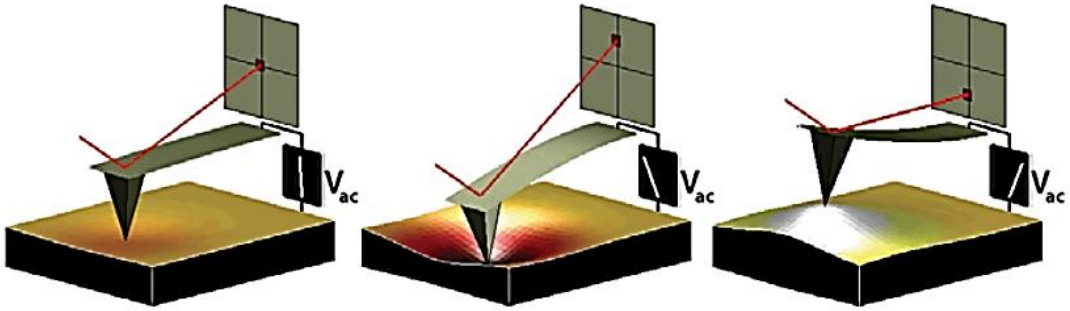

Figure 3-5 PFM out-of-plane piezoelectricity measurement mechanism.[76]

If the material under test possesses out-of-plane piezoelectricity, its out-of-plane deformation would be excited by the alternative electric field formed between the tip and the substrate. Then the deformation can be sensed by the displacement of the laser position on the photodetector.

PFM technique is the mainstream method for nano-scale piezoelectricity characterization. It provides spatially resolved measurements of the electromechanical response with nanometer-level precision. In this PhD project, the piezoelectricity/ferroelectricity of the nano flakes was characterized by PFM technique. And to improve the measurement accuracy of the piezo response, the dual AC resonance tracking (DART) mode was performed instead of the single frequency mode.

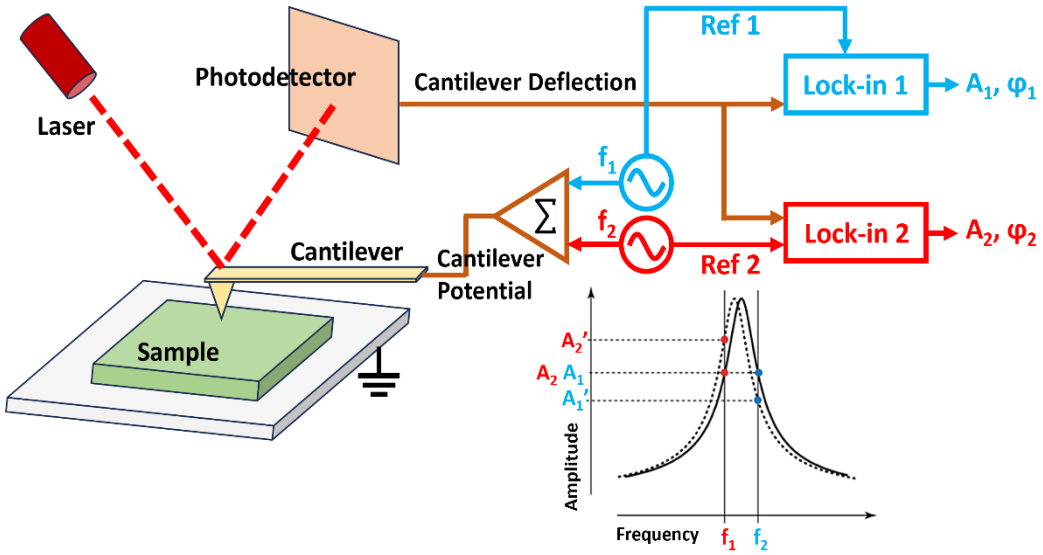

Figure 3-6 Mechanism of DART mode PFM.

For PFM measurement, the AC signal applied to the cantilever should be at its contact resonant frequency at which the cantilever exhibits maximum sensitivity to surface displacements. However, during the measurement, the contact resonant frequency always shifts because of the variation of the sample qualities and morphology. To solve this problem, DART mode, where applying two frequencies (f_1 and f_2) closed to the contact resonant frequency of the conductive tip. And two lock-in amplifiers independently measure the response of the cantilever at both frequencies. (Figure 3-6) The ratio of the amplitudes at f_1 and f_2 is used to track changes in the resonance frequency. A feedback loop continuously adjusts the excitation frequencies to follow the contact resonance frequency as it changes. This ensures that the cantilever is always operating near its maximum sensitivity point.

The Ti-Au substrate with 3R-MoS_2 or α-In_2Se_3 flakes was placed on a magnetic sample holder. A conductive magnet was connected to the Ti-Au substrate by silver paste as shown in Figure 3-7 (a). As shown in Figure 3-7 (b), a conductive tip was connected to the built-in signal pad of the PFM through the red wire of the Asylum high-voltage tip holder. While the Ti-Au substrate under the tip was connected to the built-in ground pad of the PFM through the white magnetic wire which was bonded to the conductive magnet through the magnetic force.

A schematic diagram Figure 3-7 (c) clearly shows the PFM characterization set-up for 3R-MoS_2 and α-In_2Se_3 flakes. An AC voltage V_{ac} from 0.25 V to 1.25 V with a step of 0.25 V, was applied to the conductive tip of the PFM, while the Ti-Au layer was

connected to the ground. A vertical electric field was formed between the PFM tip and the Ti-Au bottom electrode, generating the vertical piezo response of the 3R-MoS_2 flake.

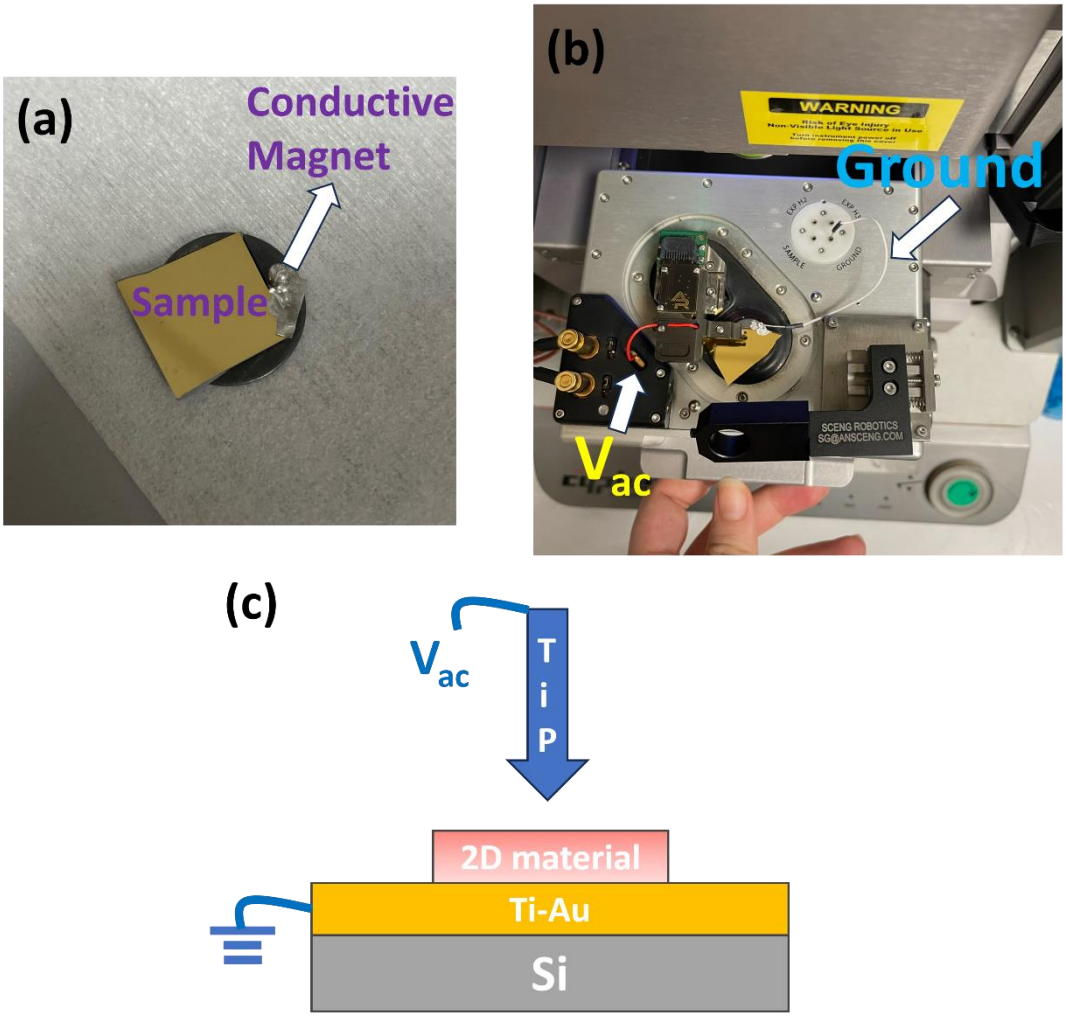

Figure 3-7 Experiment set-up for PFM piezoelectricity characterization. (a) Sample preparation. (b) Top view of sample inside the PFM. (c) Schematic diagram of the PFM out-of-plane piezoelectricity characterization for 2D flakes.

3.4 PFM Ferroelectricity Characterization

Ferroelectric materials exhibit spontaneous polarization that can be reversed by an external electric field. Additionally, due to their piezoelectric properties, they undergo mechanical deformation when subjected to an electric field. The PFM ferroelectricity characterization set-up as shown in Figure 3-8 (a) is similar to the PFM piezoelectricity characterization discussed above. However, unlike PFM piezoelectricity characterization, excitation signal for PFM ferroelectricity characterization is consisting

of two parts as shown in Figure 3-8 (b) and (c). A time changing DC bias V_{dc} with certain sequence of amplitude is applied to the conductive tip of the PFM. This DC signal functions as a poling force that tunes and switches the ferroelectric domains. At the same time, an AC signal V_{ac} is applied to generate the piezo response of the ferroelectric materials under test. The resulting mechanical deformation is detected by the cantilever deflection.

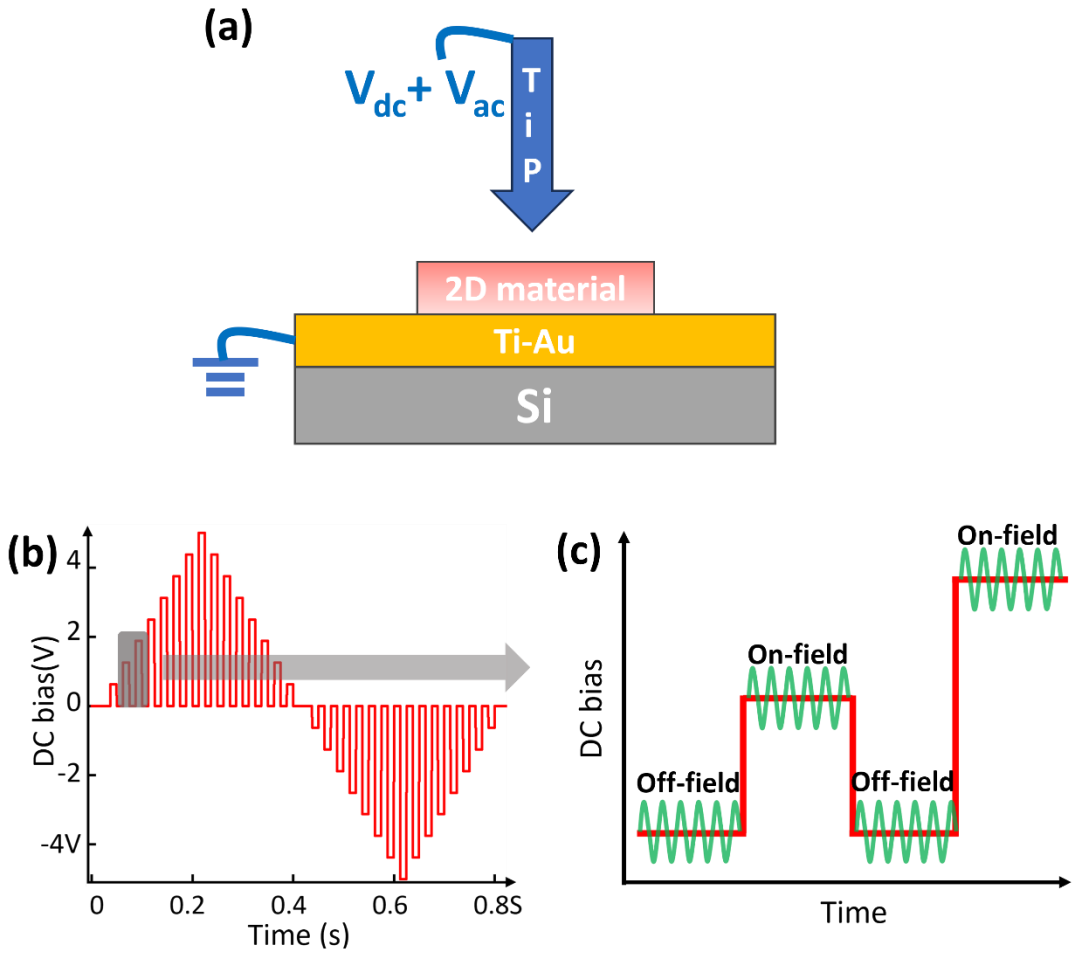

Figure 3-8 Experiment set-up for PFM ferroelectricity characterization. (a) Schematic diagram of PFM out-of-plane piezoelectricity characterization for 3R-MoS_2 flakes. (b) the DC bias voltages applied by PFM tips as a function of time, (c) AC signal loaded on the DC bias voltages.

For a ferroelectric material, the domains orientation could maintain for a certain time after poling. As a result, the test is conducted under both On-field and Off-field as shown in Figure 3-8 (c). The PFM ferroelectricity characterization was only conducted to thin α-In_2Se_3 flakes.

3.5 Fabrication Techniques of the Materials and Devices

The 3R-MoS_2 SMRs and α-In_2Se_3 FBARs were fabricated in the cleanroom of the School of Electrical and Electronic Engineering at Nanyang Technological University. Modern semiconductor manufacturing techniques, including lithography, wet and dry etching, and thin-film deposition, were utilized in the device fabrication. This section provides a concise introduction of these fabrication techniques and the corresponding characterization systems used in the fabrication of the resonator structures discussed in this thesis.

Lithography is a process used in semiconductor manufacturing to create intricate patterns on a substrate. In this project, a MABA8Gen4 Mask Aligner System was employed for the lithography process. During the lithography process, photoresist AZ5214E was first spin-coated to the surface of a substrate. After a prebake step of 2 minutes under 105 ℃ to remove solvents and harden the resist, the photoresist coated substrate was exposed to light of specific wavelengths through a mask that contains the desired pattern. After exposure, the sample was treated with a developer solution of AZ5214E, removing the unwanted photoresist while leaving the photoresist in the targeted pattern on the substrate. This patterned resist layer was then used for further processing, like etching and lifting off, to define the desired structures.

Sputtering, e-beam evaporation, and Chemical Vapor Deposition (CVD) were employed for thin-film deposition in this project. SiO_2/W layers and Al electrodes were deposited using sputtering with an Elite Sputter System. 3-inch SiO_2, W, and Al targets were used as the source materials. Table 3-1 below shows the recipe for SiO_2, W and Al growth.

Materials	Cathode	Power (W)	Gas (Torr)	Growth rate
SiO_2	RF	300	50 Ar / 8 O_2	2.5 nm/min
W	DC	100	50 Ar	8.5 nm/min
Al	DC	100	50 Ar	6.0 nm/min

Table 3-1 Sputter recipe for SiO_2, W and Al growth.

For the deposition of non-conductive materials such as SiO_2, an RF cathode was utilized, while DC cathodes were typically employed for depositing conductive materials like W and Al. During the deposition of W and Al, Ar gas was introduced into the chamber to generate high-energy ions required for the sputtering process. In contrast, for the

deposition of SiO_2, a mixture of Ar and O_2 gases was introduced into the chamber. This ensures an adequate supply of oxygen, preventing oxygen deficiency in the deposited SiO_2 film and maintaining its stoichiometric composition.[77]

In this project, Au sacrificial layers were deposited using e-beam evaporation with an Auto306 E-Beam system.

Si_3N_4 supporting layers were grown by CVD using an Aegis-20 Plasma Enhancement CVD system. SiH_4 and NH_3 were used as the reaction sources for the material deposition.

Reactive Ion Etching (RIE) technique was performed to remove Si_3N_4. SF_4 was used as the etching gas.

The detailed fabrication process of 3R-MoS_2 SMRs and α-In_2Se_3 FBARs are demonstrated in Chapter 5 and 6, respectively.

Chapter 4 Characterization of the out-of-plane Piezoelectricity of 3R-MoS_2 and α-In_2Se_3

In this chapter, we report the piezoelectricity characterization of the multilayers of 3R-MoS_2 and α-In_2Se_3. As the core piezoelectric materials involved in our FBAR devices, the out-of-plane piezoelectricity of these materials is critical for the device performance. It not only determines whether the longitudinal vibrations can be generated, but also largely influences the acoustical and electrical coupling. Besides the piezoelectricity, the influences of the piezoelectric flake thickness, surface roughness, etc. on the device performance are also studied.

4.1 Surface Roughness of 3R-MoS_2 and α-In_2Se_3

When a FBAR device vibrates, the displacement generated by the piezoelectric material would be reflected back and forth by the top and bottom surfaces, forming a standing acoustic wave propagated in the out-of-plane direction through the bulk of the piezoelectric material. Therefore, the quality of the surface of the piezoelectric material must be the reflection very flat to enhance coefficient of the acoustic waves. A rough surface would cause the scattering of the acoustic waves, leading to the attenuation of the vibration energy. Unfortunate, the surface roughness of conventional piezoelectric materials made by sputtering technique would become very poor as many defects are left behind on the sputtered surfaces. When their thickness reaches submicron, the ratio of the surface depth versus the bulk thickness increases, the negative impact of the defective surfaces on acoustic wave reflection become more significant. Rough surface is one of the disadvantages of the conventional thin piezoelectric materials.

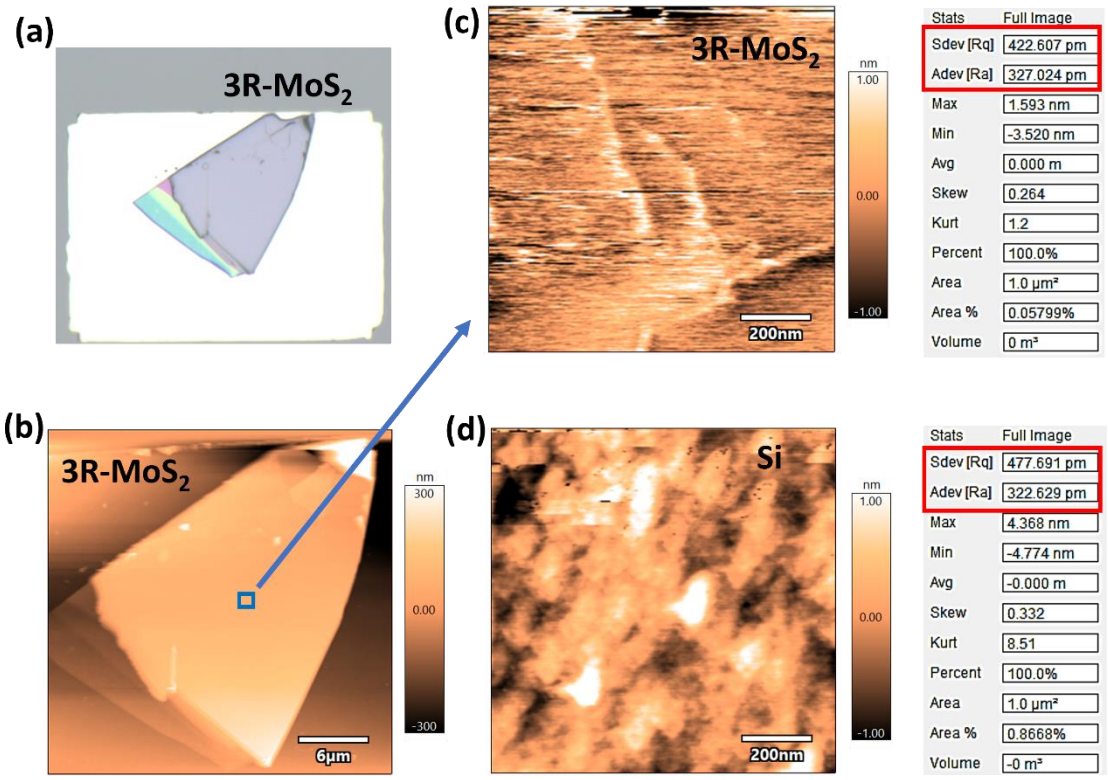

Figure 4-1 AFM characterization of a transferred 3R-MoS_2 flake. (a) Optical view, (b) AFM topology, and (c) surface roughness characterization results of the transferred 3R-MoS_2 flake. (d) Surface roughness characterization results of a standard polished Si wafer.

To overcome the problem of surface roughness of thin conventional piezoelectric materials, we utilized physically exfoliated-transferred 3R-MoS_2 or α-In_2Se_3 flakes for FBAR devices. Firstly, a physically exfoliated 3R-MoS_2 was transferred by a homemade 2D transfer stage to a targeted substrate. (Figure 4-1 (a)) The topology of the whole flake was characterized by AFM. (Figure 4-1 (b)) Then the AFM scanning area was focused to a small space of 1×1 µm on the 3R-MoS_2 flake. Figure 4-1 (c) shows the topology of the 3R-MoS_2 flake surface. The average surface roughness of this 3R-MoS_2 flake is around 327 pm, which is comparable for that of an industrial-grade high-quality Si wafer which is measured to be around 323 pm as shown in Figure 4-1 (d). While for sputtered C-axis AlN, which is the mostly used material for conventional FBARs, the average surface roughness is normally 1 to 5 nm.[78, 79]

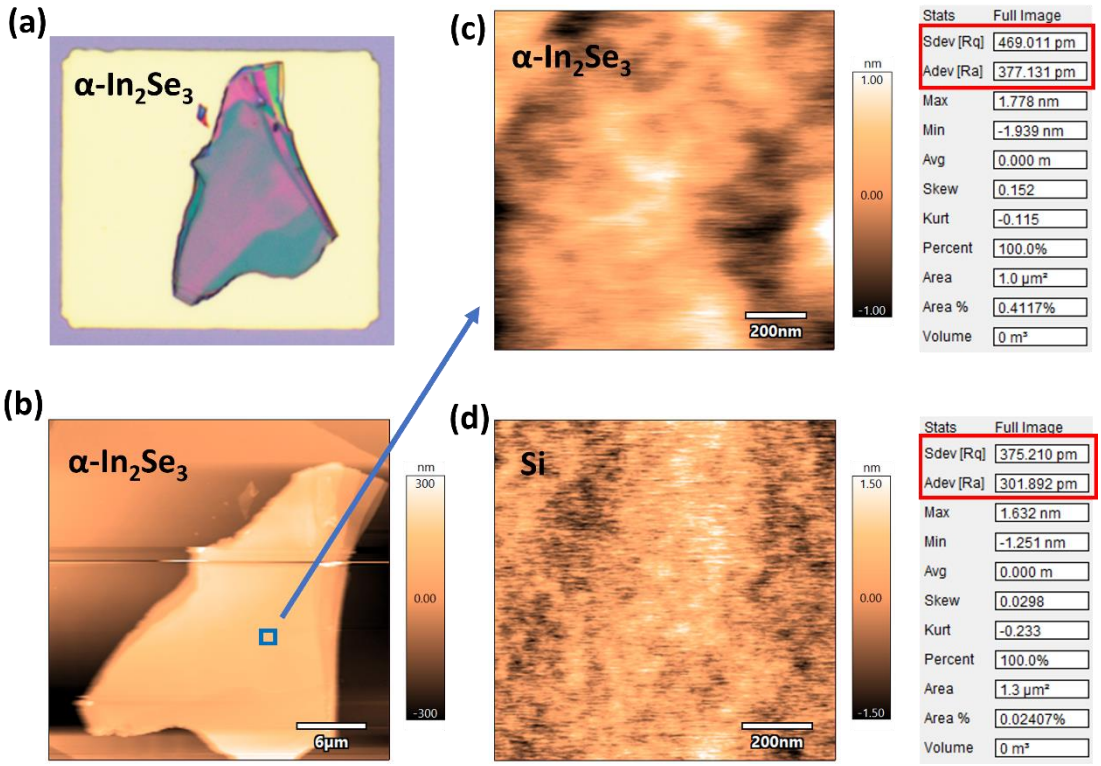

Figure 4-2 AFM characterization of a transferred α-In_2Se_3 flake. (a) Optical view, (b) AFM topology, and (c) surface roughness characterization results of the transferred α-In_2Se_3 flake. (d) Surface roughness characterization results of a standard polished Si wafer.

The surface roughness of α-In_2Se_3 flake was characterized using the similar method as 3R-MoS_2 as shown in Figure 4-2. Firstly, a α-In_2Se_3 flake was transferred to a targeted flat substrate. (Figure 4-2 (a)) Then the morphology of the whole flake and of the surface of a small area of 1×1 µm were characterized by contact mode AFM. (Figure 4-2 (a) and (b)) The average surface roughness of this α-In_2Se_3 flake is around 377 pm, which is comparable to the value 302 pm of the average surface roughness of industrial-grade high-quality Si wafer. While the Barium Strontium Titanate (BST), as the most promising material for dynamic FBARs, is normally with the average surface roughness higher than 3 nm.[80]

From the AFM characterization results, one can see that the surfaces of the exfoliated 3R-MoS_2/α-In_2Se_3 flakes are atomically flat. This originates from the multiple layer structure and the nature of the exfoliation process. 3R-MoS_2 and α-In_2Se_3 are layered material consisting of strong in-plane bonds and weak vdWs forces between layers. The weak interlayer bonding allows these materials to be easily separated into individual layers. The exfoliation process minimizes the surface roughness down to the atomic level, preserving the layer's integrity and smoothness. Additionally, the exfoliation

process does not significantly introduce new defects, leading to atomically flat and defect-free piezoelectric flakes.

4.2 Out-of-plane Piezoelectricity of Multilayer 3R-MoS_2

A high-quality piezoelectric layer is the key part of a FBAR device. The out-of-plane piezoelectricity of the piezoelectric material involved determines whether or how strong the longitudinal wave could be generated and the quality factor of the FBAR devices. Even though the piezoelectricity of the 3R-MoS_2 (and α-In_2Se_3) have been studied, due to the variation of the quality of 2D materials and the randomness introduced by the physically exfoliation process, the out-of-plane piezoelectricity of the piezoelectric flakes which are employed for novel FBARs should be characterized before device development.

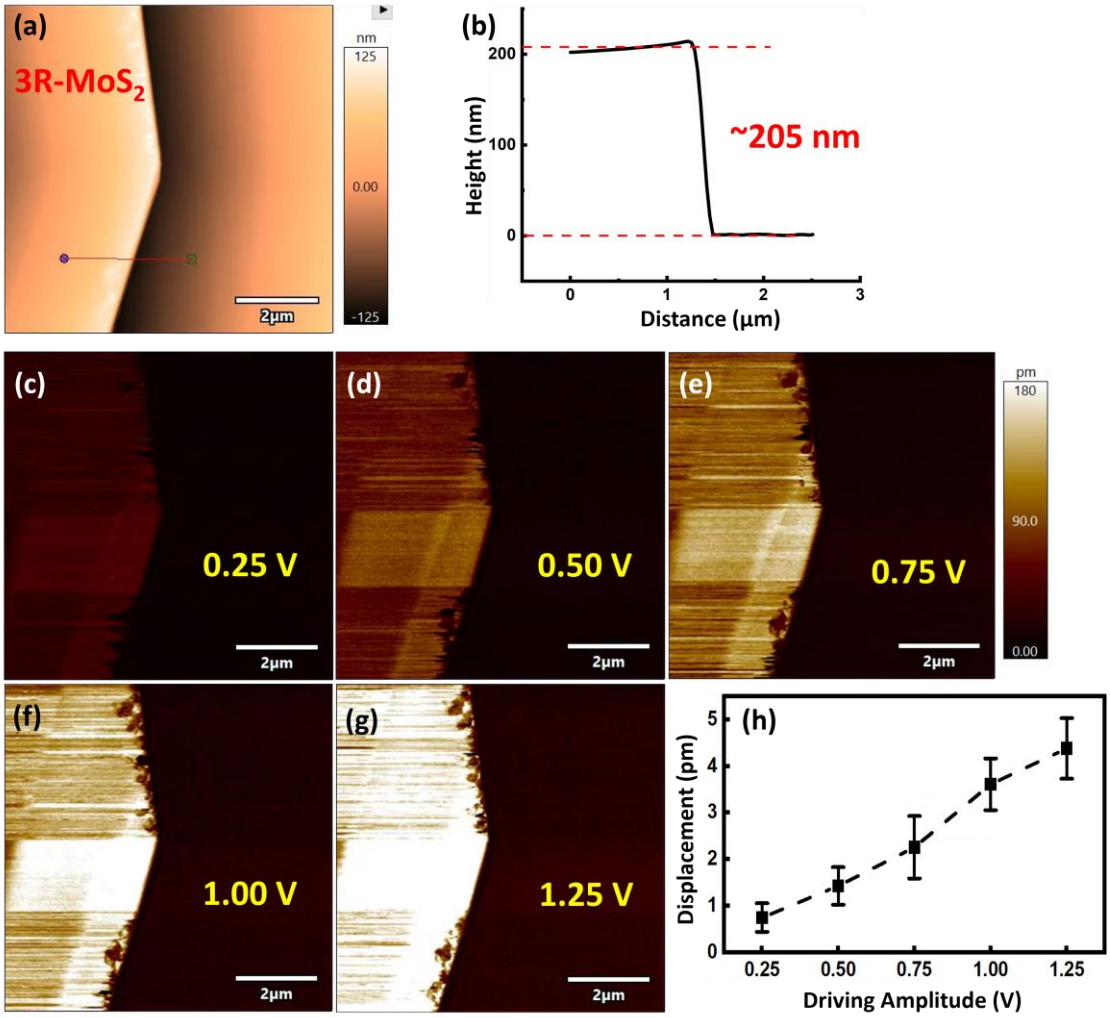

Figure 4-3 PFM piezoelectricity measurement of a 200 nm 3R-MoS_2 flake. (a) AFM image of the topology of the 3R-MoS_2 flake. (b) The thickness of this flake extracted from the red line marked in (a). (c)-(g) Piezo response of this flake with the driving amplitude from 0.25 V to 1.25 V with a step of 0.25 V. (h) The derived piezo induced displacement versus driving amplitude.

3R-MoS_2 flakes with targeted thickness ~200 nm are characterized by prementioned PFM method. Figure 4-3 shows the PFM characterization results of the 3R-MoS_2 flake. The topology of this flake (Figure 4-3 (a)) and the profile of the path from the 3R-MoS_2 flake to the substrate Figure 4-3 (b) indicate that the thickness of this flake is ~205 nm. Figure 4-3 (c)-(g) show the piezo response of this flake under driving amplitude from 0.25 V to 1.25 V with a step of 0.25 V. The piezoelectric displacement clearly increased with the voltage.

The vertical displacement of the flake as function of the applied voltage can be derived by multiplying the calibration of the inverse optical lever sensitivity (InvOLS) with the

deflection signals. Due to the ununiform electric field between the substrate and the sharp tip, only effective piezoelectric coefficient d_{eff} can be directly derived from the PFM measurement by following equation:

$$Amp = V_f \times \sigma = Q_{tune} \times d_{eff} V_{ac} \quad (2.1)$$

where Amp is the amplitude, V_f is the vertical motion of the tip, σ is the calibration constant, Q_{tune} is the quality factor of tip tuning, V_{ac} is the driving amplitude of the AC signal applied on the conductive tip. As the AFM tip was in week indentation with the flakes, the value of d_{33} and d_{eff} approximately follow the equation: $d_{33} = 2 \times d_{eff}$. [29, 81] The Amp is derived from the response of the flake minus the response of the non-piezoelectric substrate. The displacement versus different driving amplitude of this 3R-MoS_2 flake calculated by $2Amp/Q_{tune}$ is shown in Figure 4-3 (h). The d_{33} value of this 3R-MoS_2 flake is calculated to be ~3.5 pm/V. The measured d_{33} value of 3R-MoS_2 is found to be sensitive to the quality of the of 3R-MoS_2 flakes. According to our PFM measurement of several 3R-MoS_2 flakes with thickness ~200 nm, the d_{33} value was found to vary from 2.0 pm/V to 3.5 pm/V. This 3R-MoS_2 flake is employed in an FBARs discussed in Chapter 4.

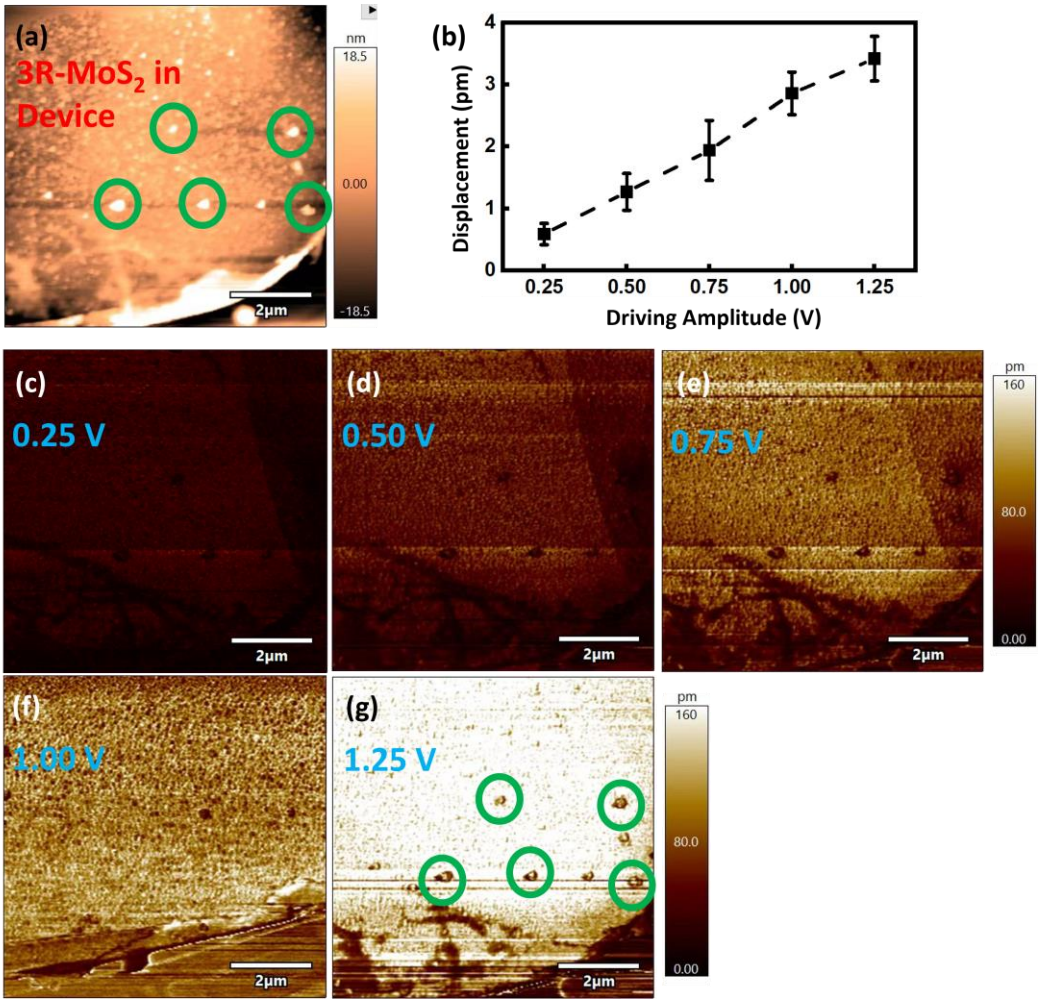

Figure 4-4 PFM piezoelectricity measurement of a 3R-MoS_2 flake in a fabricated FBAR. (a) AFM measurement of the topology of the 3R-MoS_2 flake. (b) The derived piezo induced displacement versus driving amplitude. (c)-(g) Piezo response of this flake with the driving amplitude from 0.25 V to 1.25 V with a step of 0.25 V. (Green circuits in (a) and (g) indicate a few non-piezoelectric contaminations)

To further characterize the piezoelectricity of the transferred 3R-MoS_2 flakes involved in the FBAR device, a 3R-MoS_2 flake inside a fabricated FBAR device was also characterized by PFM. Figure 4-4 (a) shows the topology of the 3R-MoS_2 flake (with 20 nm Al top electrode on top). A bottom electrode serves as floating ground in the characterization. Figure 4-4 (c)-(g) show the piezo response of this flake under the applied voltage from 0.25 V to 1.25 V with a step of 0.25 V. The Amp is derived from the response of the surface minus the response of the non-piezoelectric contaminations as shown in the green circles drawn in Figure 4-4 (a) and (g). The derived displacement versus driving amplitude of this flake is shown in Figure 4-4 (b). The d_{33} value of this flake is measured to be ~2.8 pm/V.

Non-piezoelectric impurities on the surface of the 2D flakes can cause damping of the

acoustic waves, leading to attenuation of the acoustic vibrations in an FBAR. Therefore, for FBAR fabrication, only impurity-free flakes were selected, and the fabrication process was carefully controlled to prevent the introduction of impurities.

4.3 Out-of-plane Piezoelectricity of Multilayer α-In_2Se_3

The characterization methodology of the out-of-plane piezoelectricity of multilayer α-In_2Se_3 flakes is similar to that used for 3R-MoS_2 flakes. The topology of a 120 nm α-In_2Se_3 flake is shown in Figure 4-5 (a, b). The piezo responses of this flake with the driving amplitude from 0.25 V to 1.00 V with a step of 0.25 V are shown in Figure 4-5 (c)-(f). The derived displacement of this flake is found to increase linearly with the driving amplitude as shown in Figure 4-5 (g).

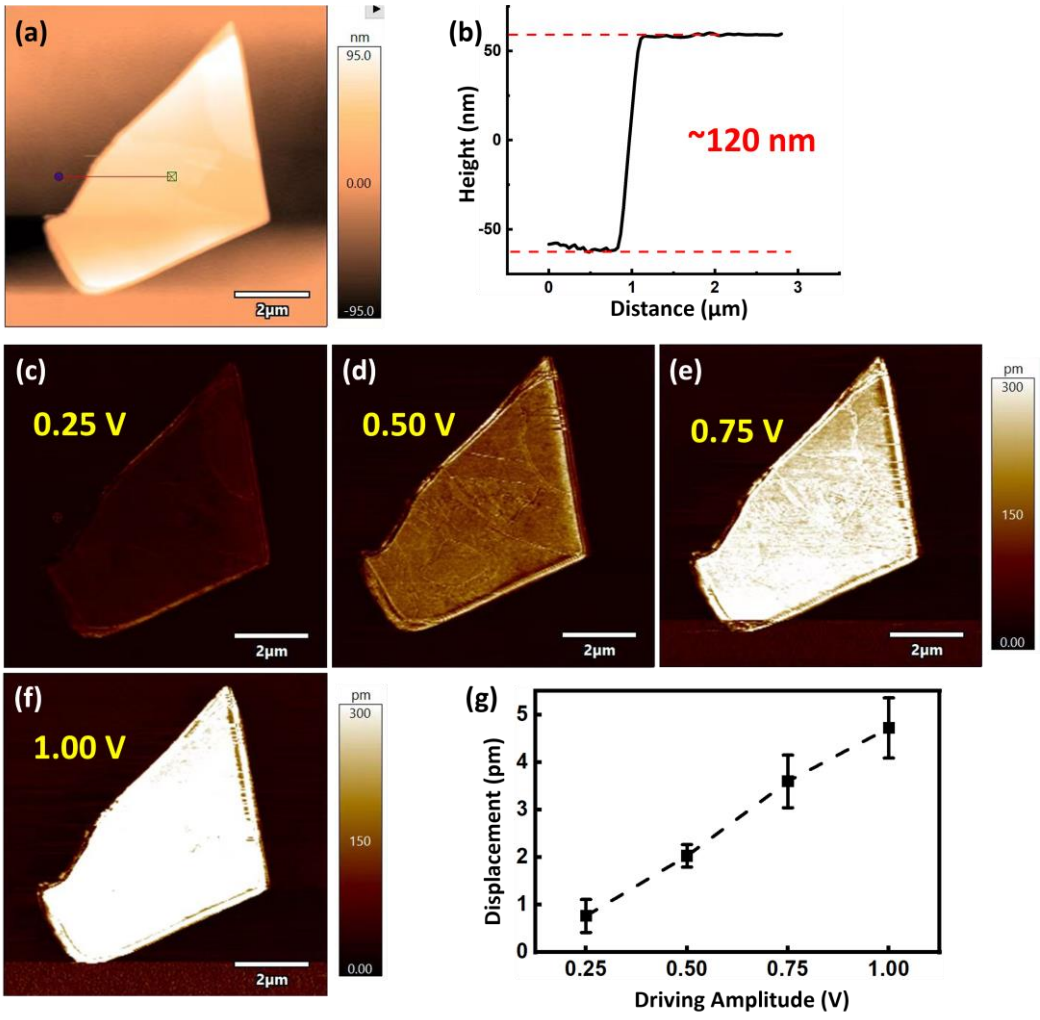

Figure 4-5 PFM piezoelectricity measurement of an α-In_2Se_3 flake. (a) AFM measurement of the topology of the α-In_2Se_3 flake. (b) The thickness of this flake achieved from (a). (c)-(f)

Piezo response of this flake with the driving amplitude from 0.25 V to 1.00 V with a step of 0.25 V. (g) The derived piezo induced displacement versus driving amplitude.

d_{33} of the α-In_2Se_3 flake is measured to be around 5.4 pm/V. According to the PFM results of several α-In_2Se_3 flakes, d_{33} of α-In_2Se_3 flakes varies from 4 to 7 pm/V for the flakes with the thickness increasing from 50 to 200 nm.

4.4 Out-of-plane Ferroelectricity of Multilayer α-In_2Se_3

Ferroelectric materials have a natural electric polarization, meaning they have a built-in electric field even without an external voltage. The polarization can be switched between different states by applying an external electric field in certain direction.

The out-of-plane ferroelectricity of transferred multilayer of α-In_2Se_3 flakes were characterized by DART mode PFM. Time changing DC voltage with amplitude of – 5 V to 5 V together with an AC excited signal with amplitude of 0.5 V were applied through the PFM conductive tip. The polarization states of the α-In_2Se_3 flake were revealed by measuring the change in the piezo response of the flake as function of the voltage applied.

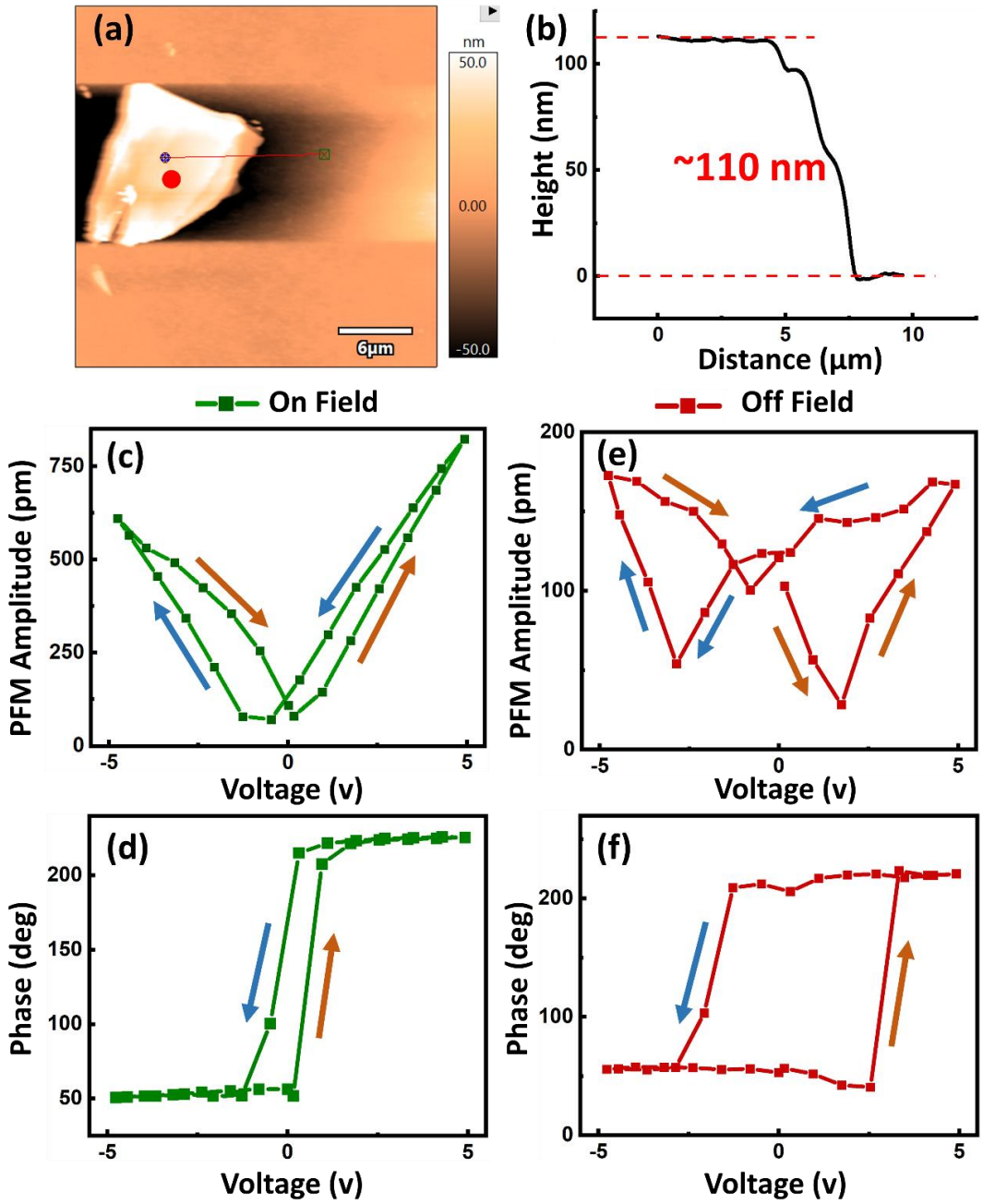

Figure 4-6 PFM ferroelectricity measurement of a 110 nm α-In_2Se_3 flake. (a) The AFM image of the α-In_2Se_3 flake under test. (b) The thickness of this flake extracted from the red line marked in (a). (c) PFM amplitude and (d) phase as function of the bias voltage between – 5 and + 5 V under the On-field. (e) PFM amplitude, and (f) phase under bias voltage between – 5 and + 5 V under the Off-field.

The 110 nm α-In_2Se_3 flake under test are shown in Figure 4-6 (a), where the red dot marked the place where the tip was landed for ferroelectricity characterization. The PFM amplitudes versus the DC bias show clear hysteresis loops with a butterfly shape in both On-field (the DC bias was on) and Off-field (the DC bias was removed after on for a certain time) as shown in Figure 4-6 (c) and (e). Those loops indicate the capability of

the material to retain its polarization state even after the external electric field is removed. A 180° phase change can be observed through Figure 4-6 (d) and (f) indicating that the electric polarization of the flake can be reversed through tuning the electric field/voltage applied.

Ferroelectricity in α-In_2Se_3 arises from its non-centrosymmetric crystal structure. This asymmetry enables the material to display spontaneous polarization, meaning it can form an inherent electric dipole moment even in the absence of an external electric field.

4.5 Summary

In this Chapter, the surface roughness, out-of-plane piezoelectricity of 3R-MoS_2 and α-In_2Se_3 flakes, and out-of-plane ferroelectricity of α-In_2Se_3 flakes are characterized by contact mode AFM and DART mode PFM technique. The 3R-MoS_2 and α-In_2Se_3 flakes fabricated by physically exfoliation method are of atomically flat surfaces, with an average surface roughness around 300-400 pm, due to their unique vdWs force bonded layered structure.

Multilayer of 3R-MoS_2 and α-In_2Se_3 flakes exhibit clear out-of-plane piezoelectricity. 200 nm 3R-MoS_2 flakes chosen for the FBARs discussed in Chapter 4 possess the value of d_{33} in a range of 2.0-3.5 pm/V. It is also found that d_{33} of α-In_2Se_3 flakes with thickness from 50 to 200 nm increases from 4 to 7 pm/V. Variations in the d_{33} value may lead to slight differences in device performance. They do not significantly affect the resonant frequency of the devices. The resonant frequency is primarily determined by the thickness and mechanical properties of the piezoelectric layer.

The atomically flat surfaces and strong out-of-plane piezoelectricity with sub-micron thickness make 3R-MoS_2 and α-In_2Se_3 flakes promising for novel FBARs with ultrahigh resonant frequencies and high performance.

Additionally, α-In_2Se_3 flakes show clear out-of-plane ferroelectricity at room temperature. It is found that their electrical polarizations could be switched by a small external electric field. As a result, α-In_2Se_3 flakes are promising for novel sensitively DC bias tunable and switchable FBARs.

Chapter 5 3R-MoS_2 Flakes based Solid Mounted Resonators with Ultrahigh Resonant Frequencies

Due to the reversely proportional relationship between the piezoelectric film's thickness and the FBAR's resonant frequency, ultrathin piezoelectric layer is required for a FBAR with ultrahigh resonant frequencies. As discussed previously, conventional piezoelectric materials lose their piezoelectricity with their thickness less than submicron. Fortunately, recent advance in several 2D piezoelectric materials provides another category of materials for high performance FBAR devices.

In this chapter, we report on the development of 3R-MoS_2 based SMR type FBARs with fundamental resonant frequencies above 20 GHz. The structure design, fabrication process, and characterization method of the 3R-MoS_2 based SMR are introduced in this chapter. This work demonstrates a proof of concept for employing 2D piezoelectric materials for high performance FBAR devices. To the best of our knowledge, this is the first batch of the FBARs based on 2D piezoelectric materials.

5.1 Structure Design

The schematic of our designed 3R-MoS_2 based SMR is shown in Figure 5-1 (a). In the top part, a 3R-MoS_2 flake is clamped by two metal electrodes, while in the bottom part, a SiO_2/W Bragg acoustic mirror is deposited on a fused quartz substrate. An AC alternative signal applied on two electrodes generates the vertical displacement/vibration of the 3R-MoS_2 flake, forming longitudinal acoustic waves. The longitudinal acoustic waves are reflected back and forth within the two electrodes. The longitudinal wave whose half wavelength corresponds to the thickness of the piezoelectric material can form a standing wave and cause strong vibration of the 3R-MoS_2 flakes. The side view of the 3R-MoS_2 based SMR is shown in Figure 5-1 (b). The area of the top electrode is designed to be around 150 μm^2 and the bottom electrode is designed with the size of 35 × 60 μm^2, as the average size of an exfoliated multilayer 3R-MoS_2 flake is usually of a few hundreds of μm^2.

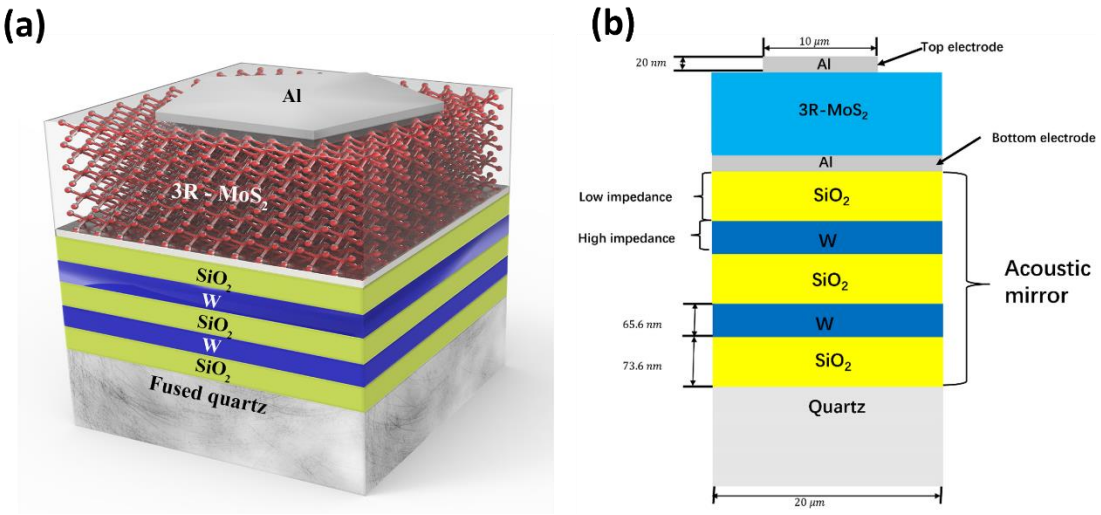

Figure 5-1 Schematic of the structure of a 3R-MoS_2 based SMR. a) Whole 3D view, b) side view.

As discussed in Section 2.2.1 of Chapter 2, the resonance occurs when half of the wavelength of the longitudinal wave propagating through the material is equal to the thickness of the piezoelectric material. (Equation 2.9: $h_p = \lambda/2$) Therefore, the fundamental resonant frequency can be generally described by the following equation:

$$f_r = \frac{V_l}{2h_p} \tag{4.1}$$

where f_r is the fundamental resonant frequency of the FBAR, V_l is the longitudinal acoustic wave velocity, h_p is the thickness of the piezoelectric layer. When the acoustic wave frequency f satisfies Equation (4.1), half wavelength of the wave is equal to the flake thickness. In this situation, the phase of reflected longitudinal waves is equal to the phase of the original longitudinal wave, those waves interfere each other and form a standing wave.

Longitudinal acoustic wave velocity V_l of a uniform piezoelectric material can be described as:

$$V_l = \sqrt{\frac{c_{33}^E + d_{33}^2/\varepsilon_{33}^S}{\rho}} \tag{4.2}$$

where c_{33}^E is the elastic constant of the piezo flake under a fixed electric field, d_{33} is piezoelectric coefficient, ε_{33}^S is the dielectric constant under a fixed press and ρ is the mass density.

Since the longitudinal wave velocity in 3R-MoS_2 nano flakes is not clear yet, we estimate it by substituting the piezoelectric coefficient d_{33} of 3.5 pm/V from measurement results, the elastic constant c_{33}^E of 92 GPa and dielectric constant ε_{33}^S of 2.6 from reported DFT[82], and the mass density of 5.06 g/cm^3 from the density of bulk MoS_2 into Equation 4.2. The longitudinal acoustic wave velocity V_l of 3R-MoS_2 is estimated to be around 5 km/s for the structure design. Since the targeted resonant frequency f_r is around 20 GHz, the thickness of the 3R-MoS_2 flakes h in the devices should be around 125 nm. Since the elastic property of 3R-MoS_2 is not clear yet, 3R-MoS_2 flakes with thickness from tens to hundreds nm were utilized to fabricate the devices in this project.

For a standard design of SMRs, the top and bottom Al electrodes are designed as 10% - 20% of the thickness of piezo layer in between. Considering that the electrode cannot be too thin to prevent discontinuity of the Al electrodes, the top and bottom electrodes are designed to be 20 nm. The top electrode is designed to be pentagon-shaped to suppress the lateral spurious mode.

The function of the Bragg acoustic mirror is to prevent the leakage of acoustic energy by reflecting the acoustic wave back to the piezo layer. The Bragg acoustic mirror consists of alternative stacking of low acoustic impedance material (SiO_2 in our devices) and high acoustic impedance material (tungsten). The acoustic reflection by interface between two different media is described as:

$$R_p = I_p \frac{Z_2 - Z_1}{Z_2 + Z_1} \tag{4.3}$$

where R_p is the reflected portions of the acoustic wave, and I_p is the total incident portions of the wave. Z_2 and Z_1 are the acoustic impedance of the two media, respectively. According to Equation (4.3), the larger difference between Z_2 and Z_1, the more acoustic energy can be reflected. Table 4-1 lists the acoustic velocity and impedance of several materials.

Materials	Acoustic velocity (m/s)	Acoustic impedance (kg/m^{2}s)
SiO_2	5800	13.2×10^6
Al	6320	17×10^6

Si_3N_4	9900	21.8×10^6
AlN	11000	36.3×10^6
Copper	4700	41.6×10^6
Mo	6190	63.8×10^6
Tungsten	5180	100×10^6

Table 5-1 Acoustic velocity and impedance of different materials

The acoustic impedance Z_a can be calculated using the following relation:

$$Z_a = \rho V'_l \tag{4.4}$$

where V'_l is the velocity of the longitudinal waves in the material, ρ is the density of the material. When designing a Bragg acoustic mirror, thermal expansion coefficients and temperature frequency coefficients are also considered. In our design, SiO_2 with low acoustic impedance and W with high acoustic impedance were chosen for the Bragg mirror (Table 4-1). Each layer of the Bragg mirror was designed to have the thickness equal to a quarter wavelength of the resonant acoustic wave.

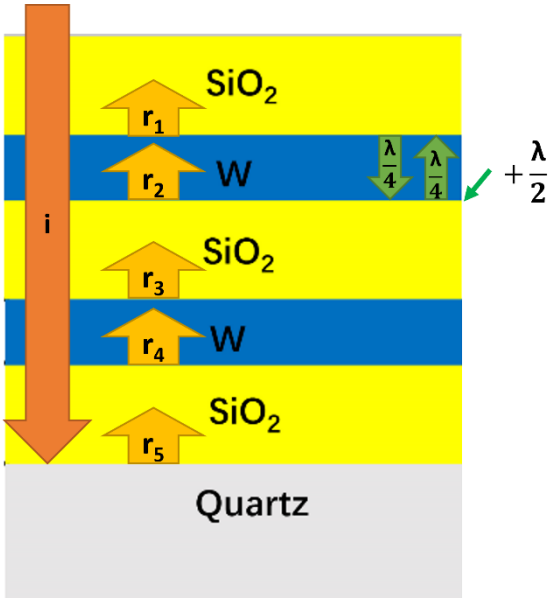

Figure 5-2 Schematic of acoustic wave propagation through the Bragg Mirror

Figure 5-2 illustrates the working principle of the Bragg mirror. When a longitudinal acoustic wave is incident (i) towards the Bragg mirror, a portion of the incident wave is reflected (r) by the SiO_2/W and W/SiO_2 interface. Taking the reflected wave r_1 by the first interface of SiO_2/W and r_2 by the second interface of W/SiO_2 interface as examples,

the thickness of the W layer in-between the first and second interface was designed to be a quarter of wavelength of the acoustic wave. As a result, when r_2 propagates to the SiO_2/W interface of r_1, there is a phase difference equal to $\left({}^{\lambda}/_{4} + {}^{\lambda}/_{4} + {}^{\lambda}/_{2}\right)\left({}^{2\pi}/_{\lambda}\right) = 2\pi$, which means r_1 and r_2 have the same phase, and their energy can gather together to form a stronger reflected wave. The same design principle is appliable to the rest layers of the Bragg mirror. All the reflected waves r_1-r_5 have the same phase so that this Bragg mirror can reflect the incident acoustic wave efficiently at the resonant frequency and prevent it from leaking to the supporting substrate.

Therefore, the thickness h_{BM} of the SiO_2 and W layers should be:

$$h_{BM} = \frac{\lambda_{BM}}{4} = \frac{V_l'}{4f_{rt}} \tag{4.5}$$

where λ_{BM} and V_l' are the wavelength and speed of the longitudinal waves propagating in a certain material of Bragg mirror, respectively. f_{rt} is the target frequency at which the strongest reflection occurs by the Bragg mirror. In this project, the target resonant frequency is above 20 GHz, i.e., $f_{rt} = 20\,\text{GHz}$. The thicknesses of the SiO_2 layer and W layer were selected to be around 72 nm and 65 nm, respectively.

Theoretically, the reflectivity of a Bragg mirror increases with the number of alternating layers. However, in practice, an optimal number of the layers must be selected in line with a balance between achieving sufficient reflectivity and managing fabrication complexity. According to Equation 4.3, the reflection ratio *R* vs number of high reflection interfaces *N* for a SiO_2/W Bragg mirror can be roughly calculated by:

$$R_N = 1 - \left(1 - \frac{Z_W - Z_{SiO_2}}{Z_W + Z_{SiO_2}}\right)^N \tag{4.6}$$

where Z_W and Z_{SiO2} are the acoustic resistivity of tungsten and SiO_2 respectively. For a 3/5/7 layers Bragg mirror, where *N* is 1/2/3, the calculated reflection ratio R_N are 76.7%, 94.6% and 98.7%, respectively. A five-layer structure offers an optimal balance between the reflection properties and fabrication complexity, and therefore it was chosen for this project.

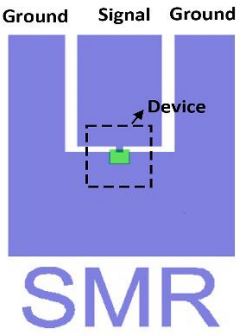

Figure 5-3 Schematic diagram of a ground-signal-ground coplanar waveguide employed in our SMR devices.

For RF measurements, an adapted Ground-Signal-Ground (GSG) coplanar waveguide (CPW) (see Figure 5-3) was carefully designed and fabricated to get the impedance matching of 50 ohms.

5.2 Device Fabrication

The fabrication of the 3R-MoS_2 based SMRs was performed in a clean room using the modern semiconductor fabrication technique. The fabrication processes of the 3R-MoS_2 based SMRs are shown in Figure 5-4.

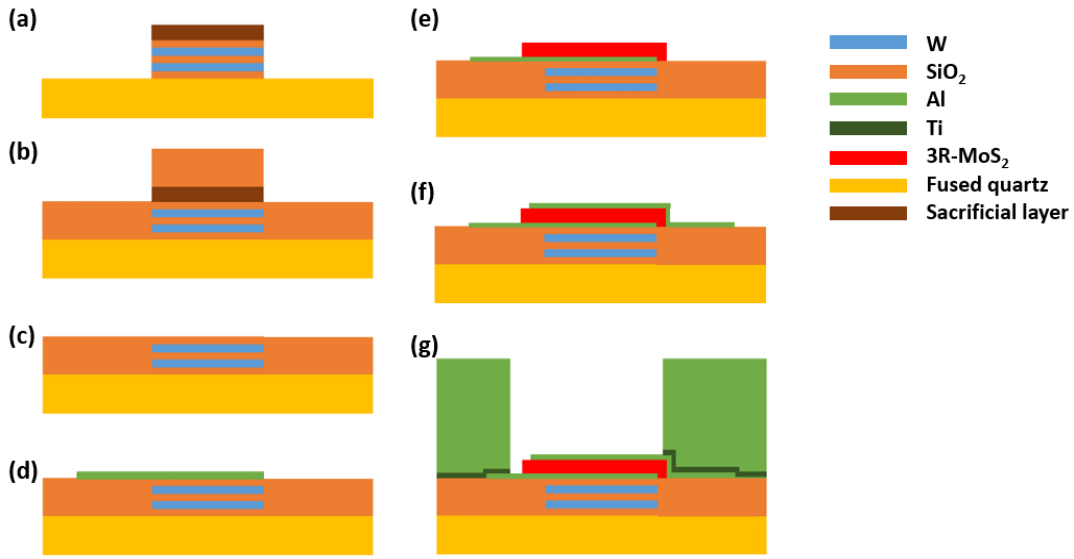

Figure 5-4 Schematic diagram of the fabrication processes of the 3R-MoS_2 based SMRs: (a) Bragg mirror and sacrificial layer deposition. (b) SiO_2 passive layer deposition. (c) Sacrificial

layer removal. (d) Bottom electrode deposition. (e) 2D material transfer. (f) Top electrode deposition. (g) CPW deposition.

First, low acoustic impedance SiO_2 layers with thickness of 65-75 nm and high acoustic impedance W layers with thickness of 60-70 nm were alternately deposited on a double-side polished fused quartz substrate using a RF sputter system and a DC sputter system respectively, forming a Bragg acoustic reflector with 3 SiO_2 layers and 2 W layers (Figure 5-4 (a)). The vacuum for both RF and DC sputter chambers was kept around 2×10^6 Pa before venting. For SiO_2 sputter process, 300 RF power, 50 Torr Ar gas and 8 Torr O_2 gas were selected under room temperature. The deposition rate was near 2.5 nm/min, and it was influenced by the surface of the substrate. For W sputter process, 100 DC power, 50 Torr Ar gas were settled under room temperature. The deposition rate was near 8.5 nm/min. The thickness of each layer is the most important parameter for the Bragg mirror, and the deposition process should be well controlled.

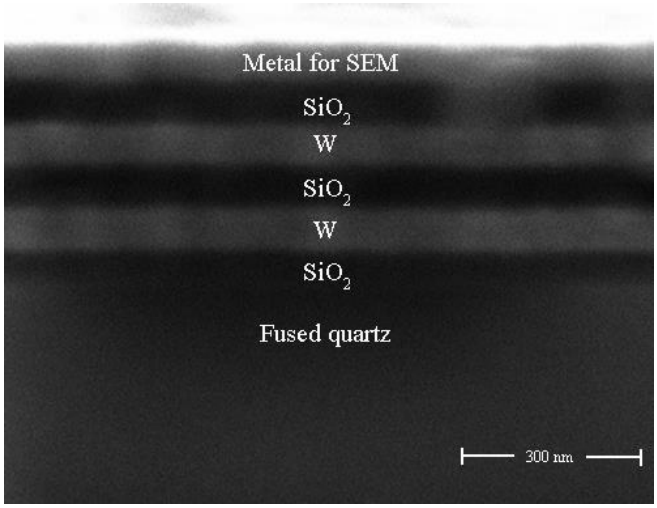

Figure 5-5 SEM side view of a fabricated Bragg mirror.

The fabricated Bragg mirror is characterized by the SEM as shown in Figure 5-5. The black stripes are the nonconductive SiO_2 layer, and the light stripes in between are the conductive W layer. Additionally, a sacrificial layer of Cr around 100 nm was deposited over the Bragg mirror for better SEM image.

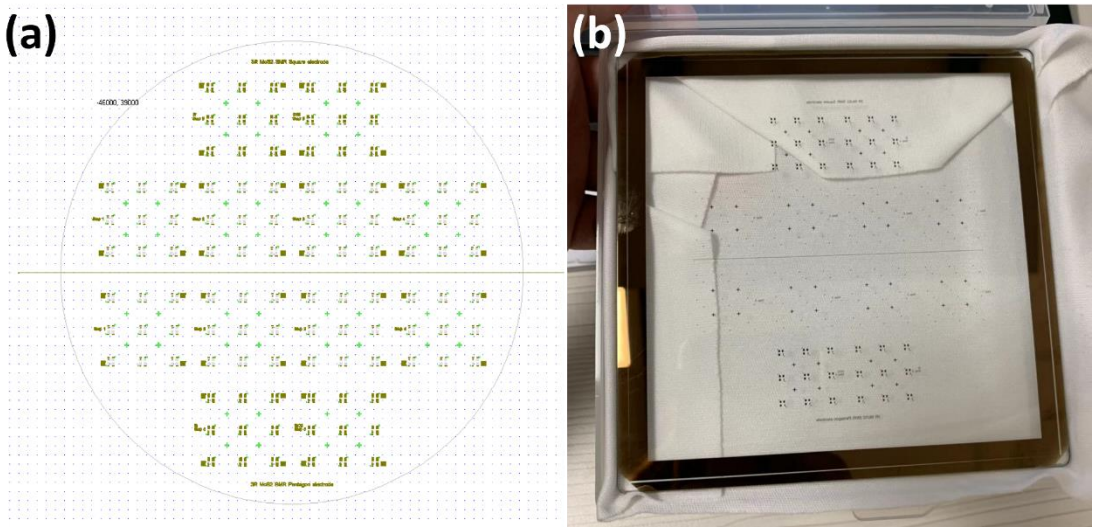

Figure 5-6 (a) The design of the mask and (b) the fabricated mask for 3R-MoS_2 based SMR fabrication.

The lithography and lift-off process are used to fabricate Bragg mirror and other parts of the 3R-MoS_2 based SMR with certain mask patterns. The lithography mask layout for the fabrication of 3R-MoS_2 based SMR was designed in a 5-inch demi wafer. (Figure 5-6 (a)) The light-field mask (Figure 5-6 (b)) with negative photoresist was used for the sake of lift-off process involved.

Then, around the Bragg mirror, a SiO_2 passivation layer with the same thickness as that of the Bragg mirror was deposited to prevent any possible connection and crosstalk between the waveguide and the W layers in the Bragg reflector (Figure 5-4 (b)). The SiO_2 on top of the sacrificial Cr layer was removed together with the Cr layer in a lift-off process. (Figure 5-4 (c)).

After that, a bottom Al electrode with an area of 35 × 60 μm, thickness of 20 nm was then deposited onto the top of the Bragg reflector using a DC sputtering system (Figure 5-4 (d)). 100 DC power, 50 torr Ar gas were settled. The deposition rate was 5 nm/min.

A 3R-MoS_2 flake was transferred onto the bottom electrode (Figure 5-4 (e)). The 3R-MoS_2 flake was exfoliated from a bulk 3R-MoS_2 crystal and then transferred with a PDMS carrier. The material transfer was realized by a homemade transfer stage shown in Figure 5-7. The PDMS carrier with the 3R-MoS_2 flake was attached to the bottom surface of a glass slide fix on one end of the stage, while sample was placed on the plate at the other end as shown in Figure 5-7 (a). The flake on the PDMS carrier was aligned under an optical microscope and then pressed to the bottom electrodes as shown in

Figure 5-7 (b). The 3R-MoS_2 flake could be transferred onto the bottom electrode after heating.

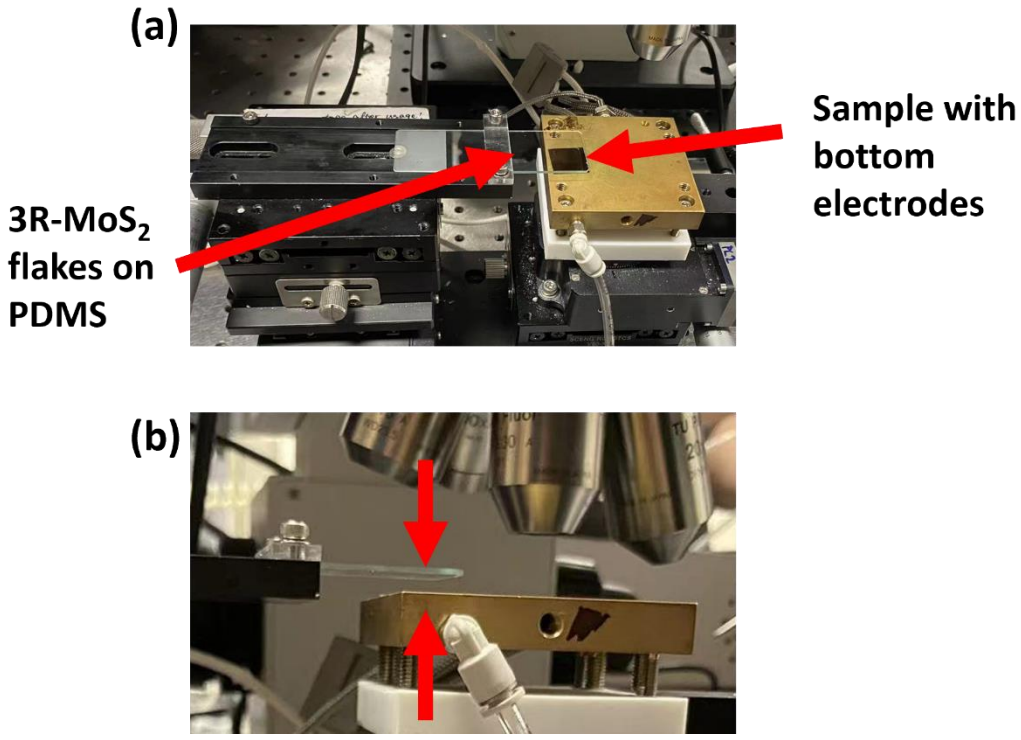

Figure 5-7 2D material transfer using a homemade transfer stage: (a) whole view, and (b) side view.

After the transfer, anneal at 200 °C for 10 minutes was performed to enhance the adhesion between the transferred 3R-MoS_2 flakes and the bottom Al electrode.

It is worth noting that, unlike conventional FBARs where the piezoelectric layer is deposited directly onto the bottom electrodes, 2D-based FBARs feature piezoelectric nanoflakes placed on the surface of the bottom electrodes. As a result, the bonding of the nanoflakes and the bottom electrodes may be relatively weak. This may affect the efficiency of the coupling between the acoustical and electrical energy and decrease the K_t^2.

Next, a 20 nm thick pentagonal top Al electrode with area around 150 μm^2 was deposited on the transferred MoS_2 flake using the sputter process and lithography technique (Figure 5-4 (f)). Lastly, a 1 μm thick Ti-Al CPW was deposited using the DC sputter system (Figure 5-4 (g)). For Ti sputtering, 100 DC power, 50 torr Ar gas were settled. The deposition rate was 4 nm/min. For Al waveguide sputtering, 200 DC power, 50 torr Ar gas were settled. The deposition rate was 12.5 nm/min.

5.3 Results and Discussion

5.3.1 Optical view of the fabricated 3R-MoS_2 based SMR devices

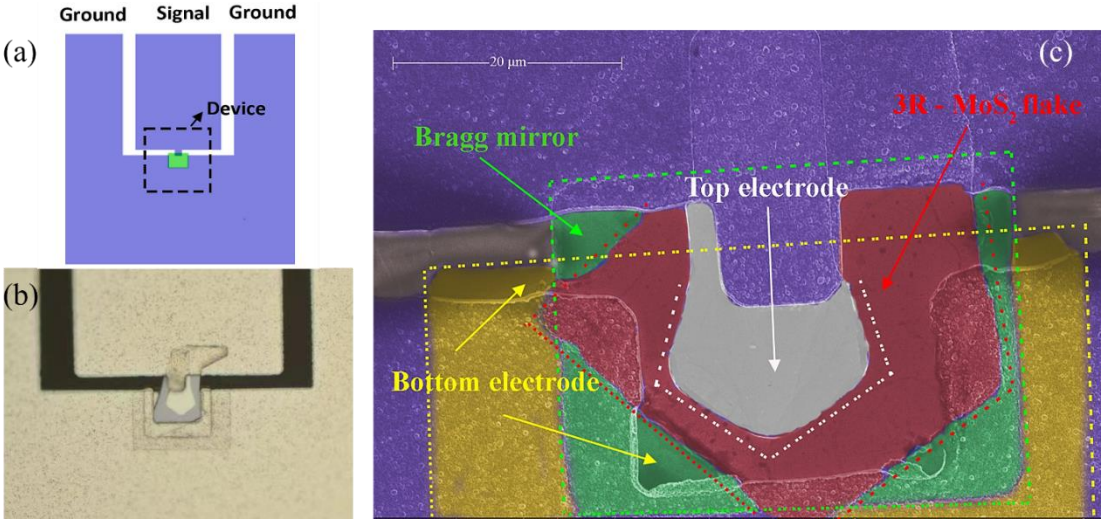

Figure 5-8 (a) Schematic of a top view of a 3R-MoS_2 based SMR with GSG waveguide. (b) Optical microscope image of top view of a 3R-MoS_2 based SMR. (c) SEM image of top view of a 3R-MoS_2 based SMR

Figure 5-8 shows a fabricated 3R-MoS_2 based SMR device. The 3R-MoS_2 based SMR device is at the center of the waveguide (Figure 5-8 (a)). An opticle microscope image of top view of the device is shown in Figure 5-8 (b). Figure 5-8 (c) shows the colored SEM image of a zoom-in top view of a 3R-MoS_2 based SMR. A 3R-MoS_2 flake (red) was clamped by the pentagonal shaped top electrode (grey) and the bottom electrode (yellow). The Bragg mirror (green) was below the 3R-MoS_2 flake and the bottom electrode. The ground waveguide (purple) was connected to the bottom electrode while the signal waveguide (purple) was connected to the top electrode.

5.3.2 RF characterization results of 3R-MoS_2 based SMR devices

The RF characterization was performed through a Keysight N5244A (frequency range from 10 MHz to 43 GHz) Vector Network Analyzer (VNA) and a Form Factor Infinity GSG RF probe. A VNA open-short-load calibration was performed before the measurement. An open-short-pad method [83] was applied to remove electrical inductive and capacitive impedance of the GSG waveguide. The open, short and pad waveguide patterns are shown in Figure 5-9. A homemade Python program was developed to perform this de-embedding analysis.

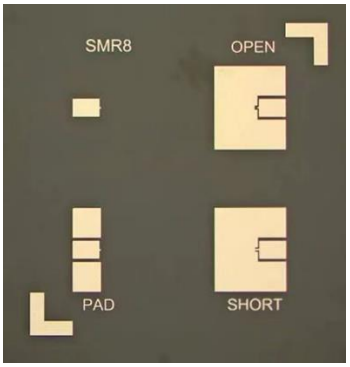

Figure 5-9 Open-short-pad pattern for de-embedding.

As discussed in Chapter Two, S_{11} parameter is defined as the reflection coefficient at Port 1 of the network analyser when Port 2 is terminated with a matched load. When a resonance occurs, a minimum value in S_{11} at the resonant frequency can be observed.

Several 3R-MoS_2 based SMRs with 3R-MoS_2 thickness from 60 nm to 300 nm were fabricated and characterized. Five samples with 3R-MoS_2 thickness of 210 nm (Sample 1), 220 nm (Sample 2), 235 nm (Sample 3), 240 nm (Sample 4) and 290 nm (Sample 5) showed sharp downward peaks in S_{11} versus the frequency curves as shown in Figure 4-2 with frequencies from 20.3 GHz to 27.5 GHz. All 5 devices demonstrated clear resonance characteristics at the frequencies larger than 20 GHz. The 210 nm 3R-MoS_2 based SMR showed a fundamental resonant frequency up to 27.5 GHz, which is the highest among all reported bulk acoustic wave resonators so far, to the best our knowledge.

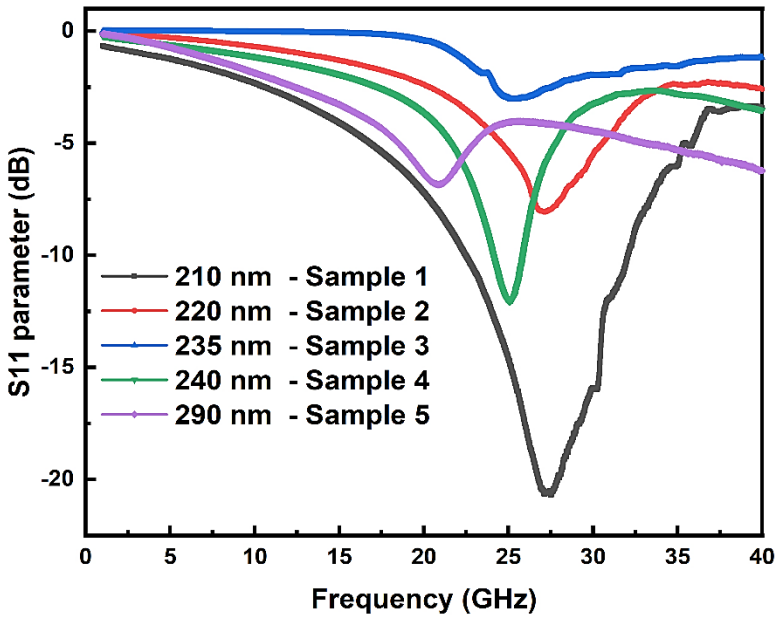

Figure 5-10 S_{11} parameters versus the frequency of the five 3R-MoS_2 based SMR.

The different performance among the five samples may come from several reasons. First, the matching between the resonant frequency with the multilayer thicknesses of the Bragg mirror could greatly influence the strength of the resonant vibration in the FBAR. If the resonant vibration in the top part the FBAR device does not very well match the reflected waves by the bottom part, the acoustic energy cannot be refined inside the piezo layer. Under the worst circumstance, the resonance may not occur. Second, the complex fabrication processes would introduce several uncertainties and non-uniformities that affect the device performance badly. For example, the impedance of the CPW, top electrode and in-between connections were found to be sensitively dependent on the fabrication processing details. Additionally, the quality, morphology, adhesion of 3R-MoS_2 flakes with the bottom electrode could introduce fluctuations in the device performance.

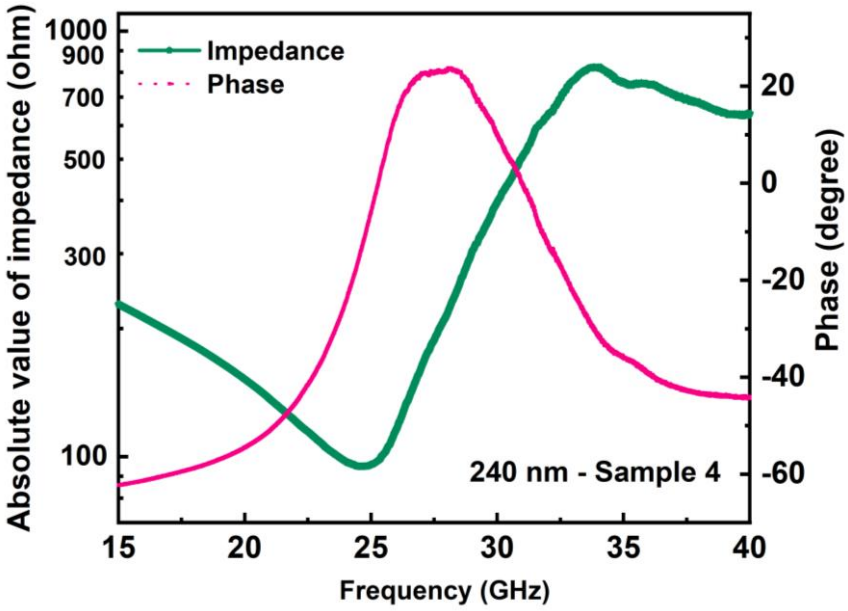

Figure 5-11 The absolute impedance (log-scale) and phase of Sample 4

Figure 5-11 shows the impedance and phase of Sample 4 which exhibits the best resonance. The 240 nm 3R-MoS_2 based SMR (Sample 4) has a minimum impedance around 70 Ω at f_r ~25 GHz and a maximum impedance around 800 Ω at an anti-resonant frequency f_a~33 GHz, which is the typical feature of an acoustical resonance according to the MBVD model introduced in Chapter two. Phase change from capacitive to inductive can also be observed within the resonant frequency and the anti-resonant frequency.

The electromechanical coupling coefficient (k_t^2) of this 3R-MoS_2 based SMR can be

calculated using equation 2.18, as relisted below for convenience.

$$k_t^2 = \frac{\frac{f_r}{f_a}\cdot\frac{\pi}{2}}{tan\left(\frac{f_r}{f_a}\cdot\frac{\pi}{2}\right)} \tag{2.18}$$

For Sample 4, the k_t^2 is estimated to be 47.6%.

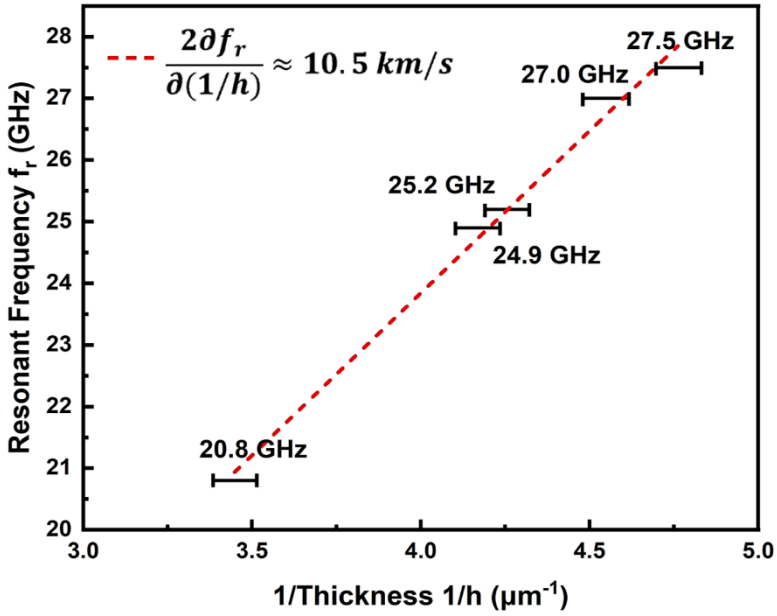

Figure 5-12 The resonance frequency vs. one over the thickness of the 3R-MoS_2 flakes used in Samples 1 to 5.

From Figure 5-12, the linear proportional relationship between the resonance frequency versus the thickness of the 3R-MoS_2 flakes can be seen. These findings are consistent with the feature of the thickness extension mode (longitudinal wave). The longitudinal acoustic velocity in 3R-MoS_2 flakes shown in Figure 5-12 can be calculated using Equation (4.1), around 10.5 km/s. This velocity is higher than that in ZnO (~3 km/s), PZT (~4 km/s) and quartz (~5.8 km/s), but comparable to that in AlN (~11 km/s).

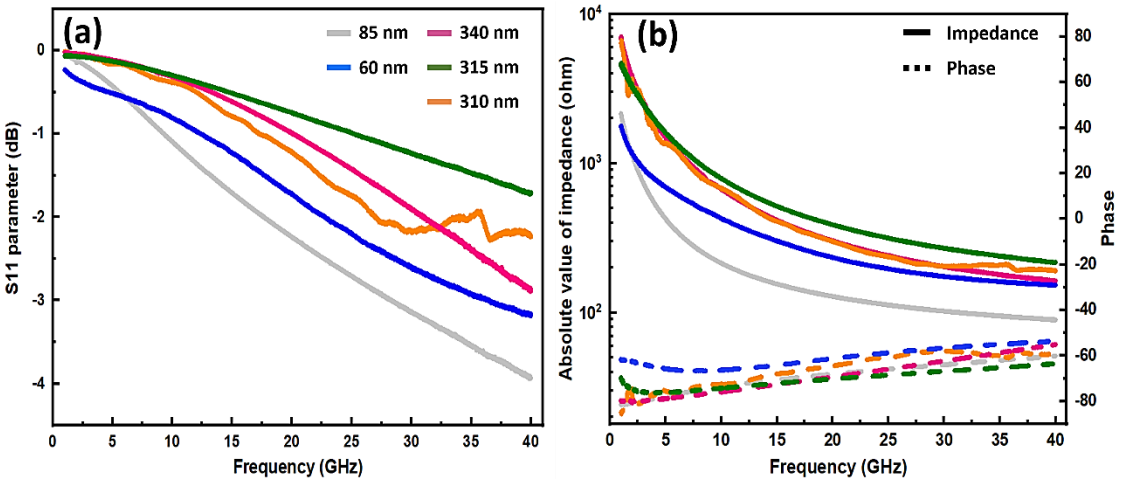

Figure 5-13 S_{11} measurement results and (b) absolute value and phase of the impedance of two samples with 3R-MoS_2 with thickness outside the range of 210 nm – 290 nm.

3R-MoS_2 flakes with thickness from tens to hundreds of nanometers were transferred to the Bragg mirror substrate which contained three low impedance 65-75 nm SiO_2 layers and two high acoustic impedance 60-70 nm W layers. However, due to the mismatch between the eigen frequencies of 3R-MoS_2 flakes and the frequency of the reflected waves by the Bragg mirror, only the devices with a 3R-MoS_2 flake whose thickness was between 210 nm and 290 nm showed apparent resonance characteristics.

Figure 5-13 shows S_{11} parameters for another 5 samples with 3R-MoS_2 flakes whose thicknesses were 60, 85, 310, 315 and 340 nm, respectively. No obvious S_{11} peak could be observed from 1 up to 40 GHz. No high impedance state and low impedance state could be observed in the impedance frequency response shown in Figure 5-13 (b). The impedance of the 5 samples decreased as increasing the frequency of the excited signal, exhibiting the features of a capacitor. From the phase frequency response shown in Figure 5-13 (b), no clear phase change was observed. All those findings support that no resonant acoustical vibrations were generated for those samples in which the 3R-MoS_2 flake thickness were beyond the frequency of the reflected waves from the Bragg mirror.

5.3.3 Finite element method (FEM) simulation of a 3R-MoS_2 based SMR

To help us in-depth understanding of the mechanical and electrical behavior of the 3R-MoS_2 based SMRs during resonance, a 2D FEM simulation was performed to simulate the mechanic and electric coupling inside the 240 nm thick 3R-MoS_2 flake based SMR.

The physical properties of the 3R-MoS_2 flake used in the simulation are listed below.

The volumetric mass density $\rho = 5.06\ \mathrm{g}/cm^3$ for bulk MoS_2 crystals[84] was used as the density of the 3R-MoS_2 flakes.

The elastic stiffness matrix (GPa):[82]

$$s^E = \begin{pmatrix} 247 & 67.7 & 32.2 & -10.7 & 0 & 0 \\ 67.7 & 247 & 32.2 & 10.7 & 0 & 0 \\ 32.2 & 32.2 & 900 & 0 & 0 & 0 \\ -10.7 & 10.7 & 0 & 38.6 & 0 & 0 \\ 0 & 0 & 0 & 0 & 38.6 & -10.7 \\ 0 & 0 & 0 & 0 & -10.7 & 89.65 \end{pmatrix}$$

The dielectric constant: [82]

$$\varepsilon^T = \begin{pmatrix} 16.3 & 0 & 0 \\ 0 & 16.3 & 0 \\ 0 & 0 & 2.6 \end{pmatrix}$$

The piezoelectric constants (pm/v):

$$d = \begin{pmatrix} 0 & 0 & 0 & 0 & -4.1 & -3.6 \\ -3.6 & 3.6 & 0 & -4.1 & 0 & 0 \\ -0.21 & -0.21 & 3.5 & 0 & 0 & 0 \end{pmatrix}$$

The piezoelectric constants were imported partly from the DFT calculation.[82] The most important out-of-plane piezoelectric constant $d_{33} = 3.5\ pm/v$ was measured from our PFM measurement described above.

1.0 V potential was applied to the top electrode as the excitation signal while 0 V (ground) was applied to the bottom electrode.

The coupling relation between the solid mechanics and electrostatics modules is solved according to the constitutive piezoelectric equations (strain-charge form) prementioned in Chapter 2:

$$D_{3\times1} = d_{3\times6} \cdot T_{6\times1} + \varepsilon^T_{3\times3} \cdot E_{3\times1} \tag{2.5}$$

$$S_{6\times1} = s^E_{6\times6} \cdot T_{6\times1} + d^t_{6\times3} \cdot E_{3\times1} \tag{2.6}$$

where D is the electrical displacement, ε^T, the permittivity constants under fixed stress, T, the stress matrix, S, the strain matrix, s^E, the elastic stiffness constants under fixed

electric field, d, the piezoelectric constants, and E, the electric field.

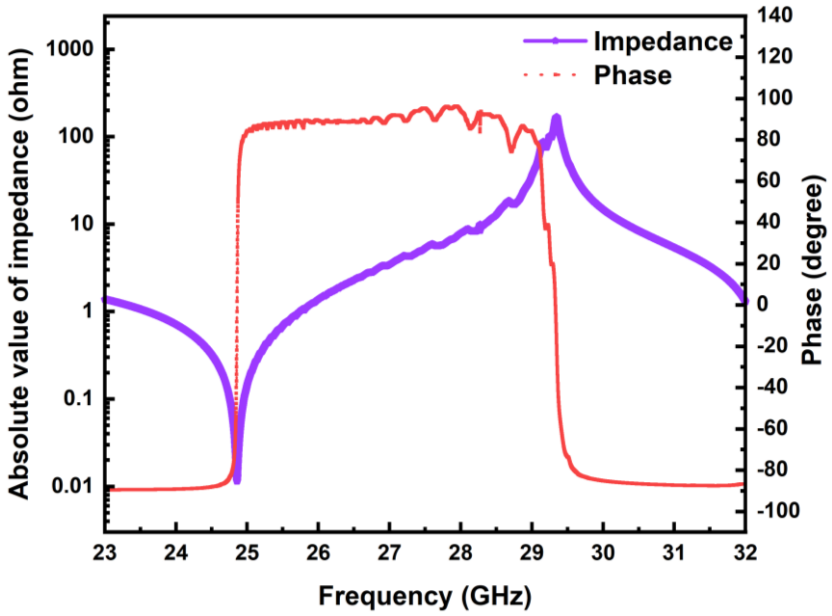

Figure 5-14 The simulated electrical absolute impedance frequency spectrum and phase frequency spectrum.

The simulated electrical absolute value of impedance and phase as a function of frequency for a 240 nm 3R-MoS_2 flake based SMR are shown in Figure 5-14. The simulated f_r was found to occur at 24.9 GHz and the f_a at 29.4 GHz, reasonably matched with the experimentally observed f_r and f_a in Figure 5-11. The k_t^2 of 32.6% could be calculated using Equation (2.18). Several spurious modes could be observed from the simulated curves, which could be attributed to the thickness shear modes, lateral modes or waves reflected from the Bragg mirror. A phase change from inductive (90°) at f_r to capacitive (-90°) at f_a could also be observed in the simulation results. It is the ideal phase change for a typical FBAR device. A similar phase change could be observed in the experimental results shown in Figure 5-11.

The displacement distribution and the acoustic wave propagation during the resonance were also simulated.

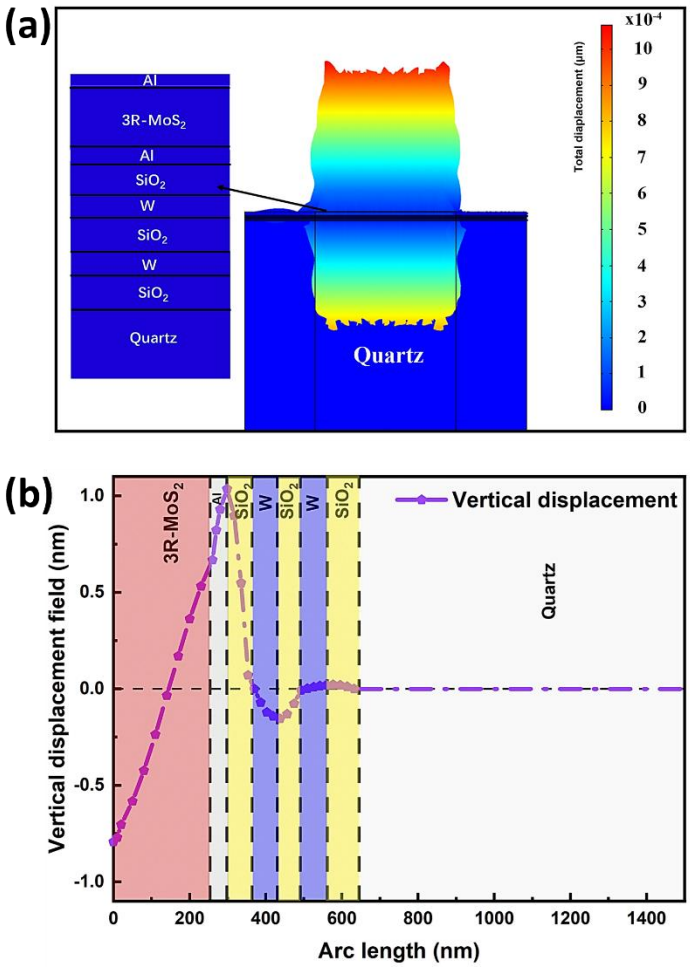

Figure 5-15 The simulated (a) mechanical mode shape and (b) vertical mechanical displacement field at the resonant frequency of 24.9 GHz.

As shown in Figure 5-15 (a), within the active region where the vertical electric field is generated by two electrodes, symmetric vertical displacements are formed at both sides of the 3R-MoS_2 piezo layer, suggesting that the resonance mode are associated with the thickness extension (longitudinal) acoustic mode. The mechanical displacement along the 3R-MoS_2 flake and the Bragg mirror at f_r is plotted in Figure 5-15 (b). The acoustic wave propagates from 3R-MoS_2 towards the substrate of the structure. Nearly half a wavelength of the wave stands through the 3R-MoS_2 layer, and a quarter wavelength through each layer of the Bragg mirror. Obvious acoustical displacement attenuation of the wave can be observed at two SiO_2/W interfaces. The acoustical displacement becomes very weak at the bottom of the Bragg Mirror, demonstrating that most of the energy is reflected by the Bragg mirror at the resonant frequency. It is worth noting that, for the design and simulation, the interfaces between the W/SiO_2 Bragg mirror were

treated as perfect interfaces. However, in practice, non-ideal factors such as roughness could cause scattering of acoustic energy, leading to a decrease in the reflection rate. More information about the simulations of the project can be found in the thesis of our collaborator.[85]

5.3.4 Comparison of our devices with other FBAR devices

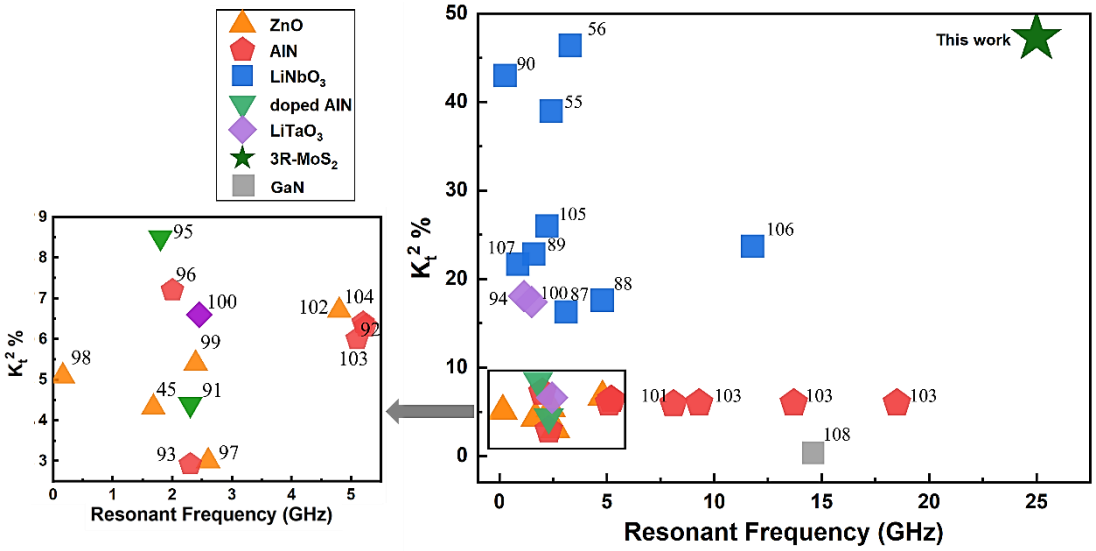

Figure 5-16 Resonance frequencies and electromechanical coupling coefficients of several thin film resonators reported by different groups and this work.[45, 55, 56, 86-108]

Figure 5-16 shows the comparison of the performance of several fundamental thickness extension mode FBARs reported by different groups since 2000 and the 3R-MoS_2 SMR introduced in this work in aspect of the resonant frequencies f_r and electromechanical coupling coefficients k_t^2.[45, 55, 56, 86-107] The mostly used and commercialized conventional piezoelectric material ZnO/AlN based FBAR normally have resonant frequencies from hundreds of MHz to 6 GHz and k_t^2 below 8%.[45, 91, 92, 96-98, 101, 103] A bench of special dome-shaped AlN based air-gap FBARs developed by Fujitsu Laboratories LTD. achieve very high resonant frequencies around 20 GHz.[102] $LiNbO_3$/$LiTaO_3$ based FBAR could have much higher k_t^2 up to ~50% compared to ZnO/AlN based FBARs and they usually possess resonant frequencies from 1 to 6 GHz.[55, 56, 86-89, 104, 106] Compared to those conventional material based FBARs, the 3R-MoS_2 based SMR-typed FBARs designed and fabricated by us have achieved advance in aspect of the resonant frequency and electromechanical coupling

coefficient.[108]

5.4 Summary

The first batch of SMR-typed FBARs based on 3R-MoS_2 thin flakes have been successfully designed, fabricated and characterized. The devices can operate at frequencies higher than 20 GHz with a size of 35×60 μm^2. Boost of the operating frequencies originates from the excellent piezoelectricity of the sub-micron thick 2D 3R-MoS_2 flakes, which is hard to be achieved using conventional materials. The physically exfoliated 3R-MoS_2 flakes could possess atomically flat surface and strong piezoelectricity with the thickness even down to a single atomic layer. This work illustrates that employing 2D piezoelectric materials in FBAR devices is a promising strategy to achieve high performance FBAR devices with superhigh operation frequencies.

Chapter 6 α-In_2Se_3 Flakes based Tunable and Switchable FBARs

A tunable FBAR is capable of toggling its acoustic resonance in real time to work in different frequency bands or match a specific target frequency. While a switchable FBAR allows the FBAR to be controlled or isolated from a specific signal path. The tunability and switchability can be realized at the same time by employing a ferroelectric material in the devices. However, conventional thin ferroelectric materials-based DC voltage-controlled switchable and tunable FBARs are facing challenges for advanced radio frequency applications because a DC voltage up to hundreds of volts is required to switch off the devices and/or create a considerable tuning range of their resonant frequencies. Since several 2D materials have been recently found to possess ferroelectricity under room temperature, advance in those 2D ferroelectric materials may create an opportunity to develop tunable and switchable ultrahigh frequency FBARs with higher tuning efficiency and lower switch on/off voltage.

In this Chapter, we present the first batch of α-In_2Se_3 based tunable and switchable FBARs. The structure design, devices fabrication processes, characterization method and measurement results of the α-In_2Se_3 based FBARs are discussed. The work discussed in this Chapter suggests that 2D ferroelectric materials are promising for tunable and switchable FBARs for next generation of wireless communication systems.

6.1 Structure Design

As mentioned in Chapter 5, mismatch between the thickness of piezoelectric materials and the targeted reflection frequency of the Bragg mirror leads to no resonant vibration of the device. Additionally, the quality of Bragg mirror would significantly affect the performance of the device. In comparison, an air gap structure was adopted for the α-In_2Se_3 based FBAR devices. Unlike Bragg mirror in a SMR which could only reflect acoustic waves with a certain frequency, the air gap structure could provide acoustical isolation for acoustic waves with all frequencies. Therefore, the mismatch problem between acoustic generator and reflector in a SMR can be avoided in the air-gap

structure.

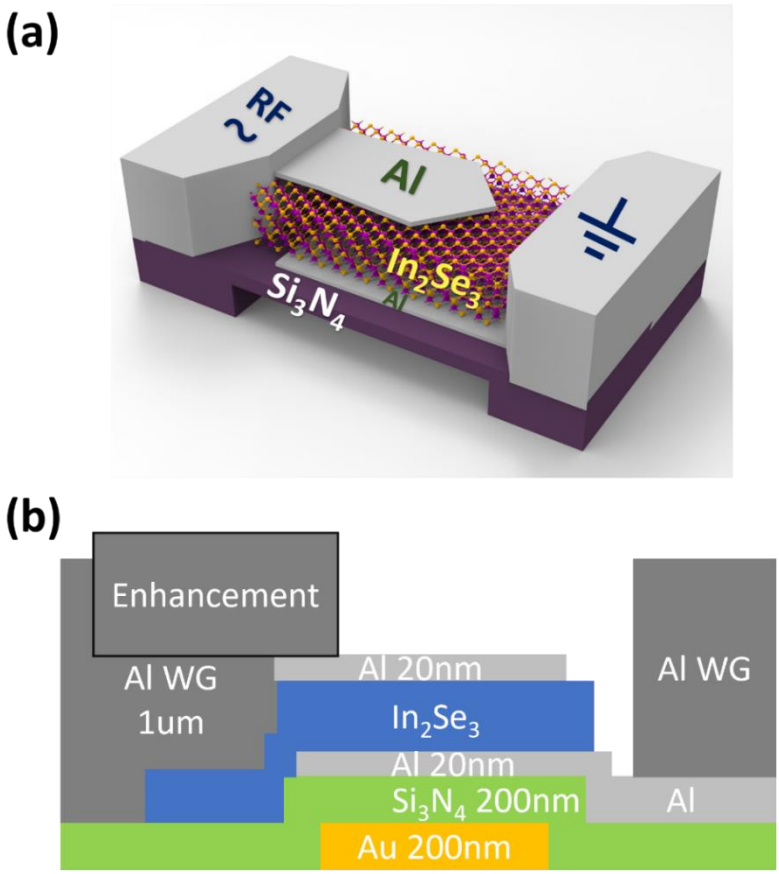

Figure 6-1 (a) 3D schematic structure and (b) Side view of the α-In_2Se_3 based FBAR.

Figure 6-1 (a) shows the 3D schematic structure of an air gap type α-In_2Se_3 based FBAR. The α-In_2Se_3 flake is clamped by two Al electrodes, serving as the longitudinal acoustic wave generator. The clamped α-In_2Se_3 flake is landed on a Si_3N_4 supporting layer which is suspended away from the substrate. An air cavity is formed between the Si_3N_4 layer and the substate. Due to the large difference of acoustic impedance between the air cavity and the clamped flake, the interface in between serves as a strong acoustical reflector that reflects the acoustic waves back to the clamped α-In_2Se_3 flake.

Figure 6-1 (b) shows the side view of the α-In_2Se_3 based FBAR. To form the air cavity between the Si_3N_4 layer and the substrate, a ~200 nm thick Au sacrificial layer with certain pattern was deposited on the substrate before the deposition of Si_3N_4. Si_3N_4 was employed as the supporting layer because it is mechanically strong and with high acoustical speed. It prevents the clamped flake from in touch with the substrate. The thickness of Si_3N_4 was ~200 nm to provide solid support to the clamped flake above. The thickness of the Al electrodes was ~25 nm to ensure the continuity of the thin metal

film. The thickness of the Al CPW was ~800 nm to ensure the good connection between two electrodes and the GSG probe which provides the signal for the device under test. An enhancement Al layer was introduced to enhance the connection between the top electrode and the signal waveguide.

6.2 The Device Fabrication

The α-In_2Se_3 nanoflakes were fabricated through mechanical exfoliation from α-In_2Se_3 crystals as is the case with 3R-MoS_2, as mentioned in Section 3.1 of Chapter 3. The fabrication of α-In_2Se_3 based FBARs was performed in a clean room using the modern semiconductor fabrication technique. The fabrication processes of the α-In_2Se_3 based FBARs are illustrated in Figure 6-2.

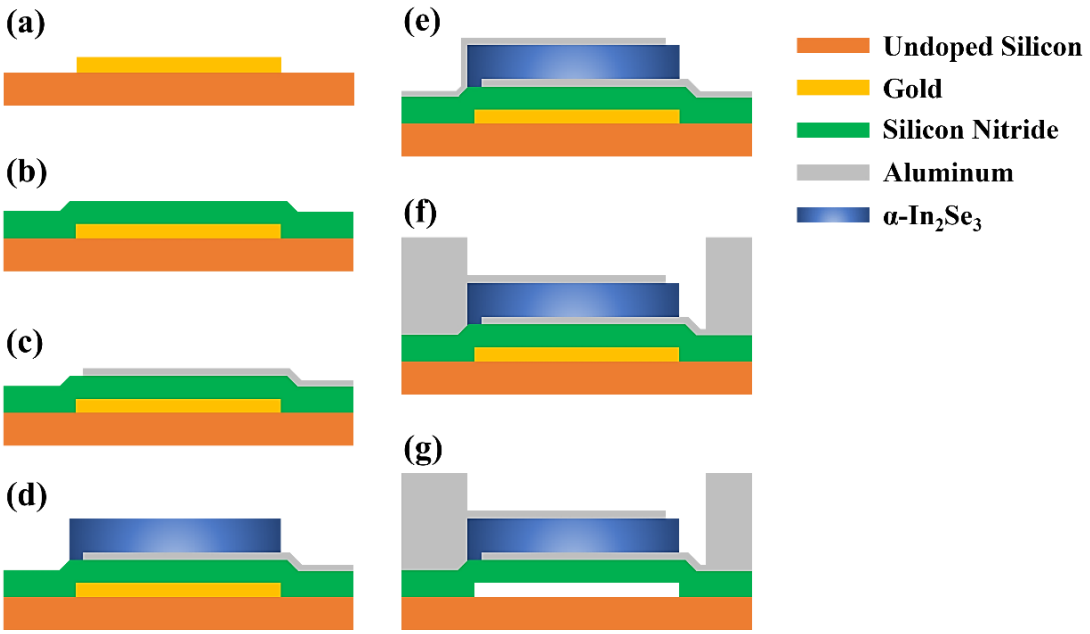

Figure 6-2 Schematic diagram of the fabrication processes for the α-In_2Se_3 based FBARs. (a) Gold deposition. (b) Silicon Nitride deposition. (c) Bottom Aluminum electrode deposition. (d) α-In_2Se_3 transfer. (e) Top Aluminum electrode deposition. (f) Aluminum waveguide deposition. (g) Gold sacrificial layer etching and formation of a thin air cavity.

First, an Au sacrificial layer with thickness around 200 nm was deposited on a high resistivity undoped silicon substrate with e-Beam evaporation (Figure 6-2 (a)). A sacrificial Au layer was of a size of 20×120 μm^2, made by lithography. On the Au sacrificial layer, a Si_3N_4 supporting layer with thickness around 200 μm was deposited by Plasma-Enhanced Chemical Vapor Deposition (PECVD) (Figure 6-2 (b)). A bottom

Al electrode with thickness around 25nm was then deposited on the Si_3N_4 supporting layer using a sputter system (Figure 6-2 (c)).

Ultrathin α-In_2Se_3 flakes with thickness from 95 nm up to around 200 nm were exfoliated from a bulk α-In_2Se_3 crystal. Then they were transferred onto the bottom Al electrode using the prementioned homemade 2D transfer stage (Figure 6-2 (d)). Thereafter, anneal at 150 °C for 60 min was performed to enhance the adhesion between the transferred α-In_2Se_3 and the bottom Al electrode. To avoid that α-In_2Se_3 flakes transfer to β-In_2Se_3 at 200 °C and above,[109] the annealing temperature was controlled below 200 °C.

Then, a 25 nm thick pentagonal top Al electrode was deposited on the α-In_2Se_3 flake using the DC sputter system (Figure 6-2 (e)). An 800 nm thick Al CWP was introduced using the DC sputter system to provide the connection between the signal/ground waveguides and the top/bottom electrodes (Figure 6-2 (f)). An Al layer was deposited to cover the step of the edge of the sacrificial layer, and therefore to enhance the connection between the signal waveguide located by side of the sacrificial layer and the top electrode located above the sacrificial layer.

Lastly, reactive-ion etching (RIE) was performed to create a via hole through the Si_3N_4 supporting layer. The Au sacrificial layer was etched by a gold etchant through the via hole, forming an air gap between the Si_3N_4 supporting layer and the silicon substrate in an active region (Figure 6-2 (g)).

6.3 Results and Discussion

6.3.1 Optical view of the fabricated α-In_2Se_3 based FBARs

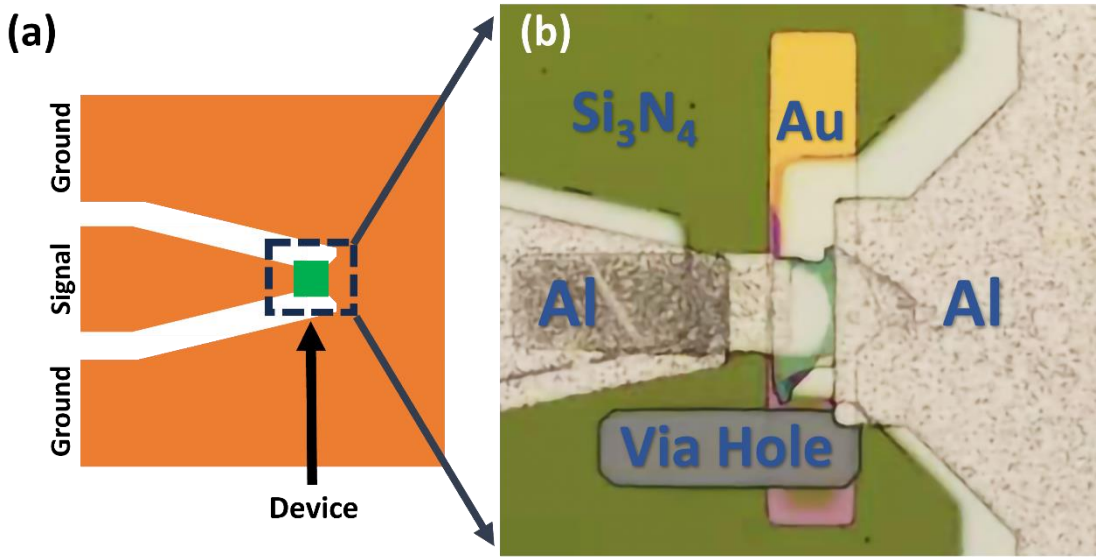

Figure 6-3 (a) Schematic layout of the device with GSG waveguide. (b) Optical view of an α-In_2Se_3 based FBAR.

The α-In_2Se_3 based FBAR is at the center of the GSG waveguide (Figure 6-3 (a)). An α-In_2Se_3 based air-gap FBAR consists of an α-In_2Se_3 flake (green flake in the center) clamped by a pentagon shaped top Al electrode and a square shaped bottom Al electrode which was prepared on the Si_3N_4 supporting layer in green, as illustrated in Figure 6-3 (b). The thick Al waveguide at the left side of the Figure 6-3 (b) was to feed signal to the top electrode, while the thick Al waveguide at the right side provides ground was in contact with the bottom electrode.

6.3.2 RF characterizations of α-In_2Se_3 based FBARs

One port *S* parameter characterization was performed using a Keysight N5244A VNA and a Form Factor Infinity GSG RF probe.

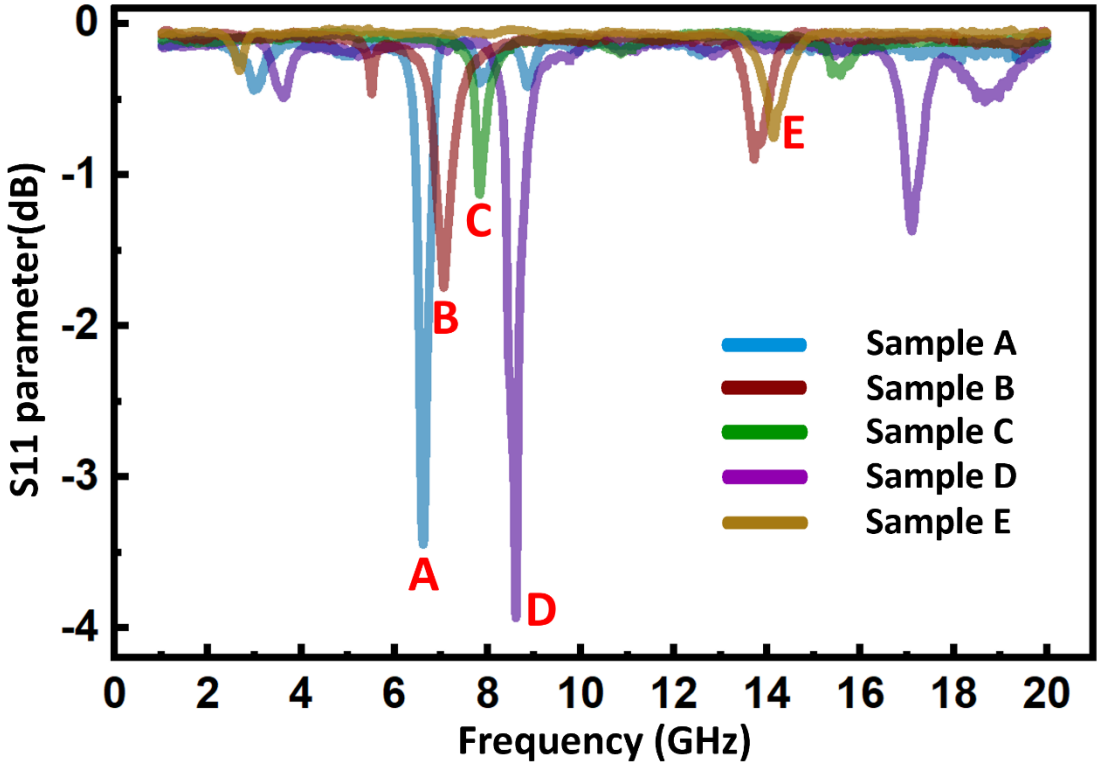

Figure 6-4 S_{11} parameters of five α-In_2Se_3 based FBAR.

Five α-In_2Se_3 based air-gap FBARs (Samples A-E) were fabricated and characterized. The α-In_2Se_3 flake thickness in Samples A-E was 205, 200, 185, 160, 95 nm, respectively. The experimental scattering parameters S_{11} over a frequency range of 1-20 GHz for the 5 samples are shown in Figure 6-4. All 5 samples show clear resonance characteristics, where downwards S_{11} peak could be observed at certain frequencies. Additionally, for Samples A-D, the second harmonic resonances at the double frequencies of the fundamental modes can be observed, suggesting that the acoustical waves are longitudinal waves.[19] According to the S_{11} characterization results, Samples A-E possess f_r around 6.60 GHz, 7.04 GHz, 7.78 GHz, 8.60 GHz, and 14.14 GHz, respectively.

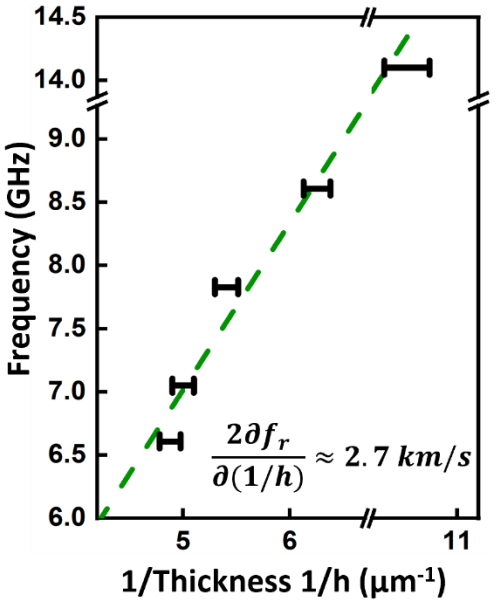

Figure 6-5 The resonant frequencies versus one over thickness of the α-In_2Se_3 flakes of Samples A-E.

According to the equation 4.1, for a FBAR, the resonant frequency is inversely proportional to the thickness of the α-In_2Se_3 flake involved. The resonant frequencies of Sample A-E in Figure 6-5 vary linearly with the reciprocals of the thickness of the α-In_2Se_3 flakes involved. The acoustic velocity of α-In_2Se_3 flakes could be evaluated from the slope of f_r versus 1/h, around 2.7 km/s. The acoustic velocity observed in our experiments is consistent with that of 3.0 ± 0.2 km/s measured by picosecond ultrasonic probing technique.[110] The little difference may come from the influence of the electrodes and the supporting layers in our α-In_2Se_3 based FBARs.

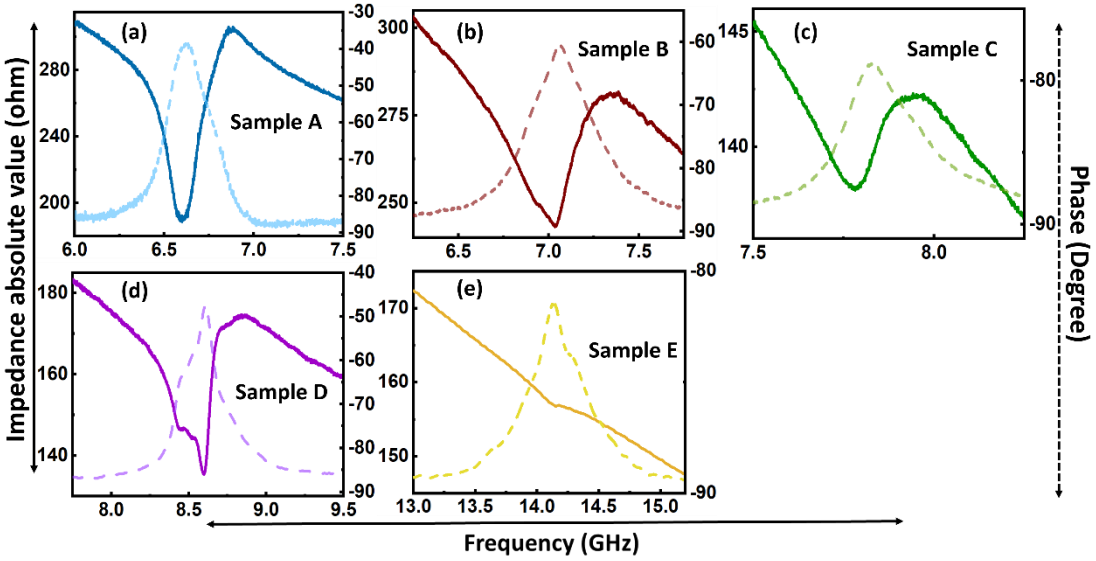

Figure 6-6 (a) - (e) the absolute impedance and phase of Samples A-E of α-In_2Se_3 based FBARs

Figure 6-6 shows the absolute values of impedance and phase of the five α-In_2Se_3 based FBARs. Samples A-E possess the minimum impedance at 6.60, 7.04, 7.78, 8.60, and 14.14 GHz. The frequency of the minimum impedance did correspond very well to the peak frequency or the resonance frequency f_r in the S_{11} parameter spectrum shown in Figure 6-4. The frequency of the maximum impedance at 6.88, 7.39, 7.97, 8.84, and 14.23 GHz is the anti-resonance frequency f_a for Sample A-E, respectively. Phase change from conductive towards inductive in between f_r and f_a can be observed for all the samples.

The K_t^2 of the five α-In_2Se_3 based FBARs can be derived from the f_r and f_a accordingly using Equation 2.18. The value of K_t^2 is estimated to be 9.6%, 11.2%, 5.7%, 6.5%, and 1.4% for Sample A-E, respectively. The resonant performance fluctuation could come from the processing condition fluctuation and different quality and thickness of the α-In_2Se_3 flakes involved.

6.3.3 Tunability and switchability of an α-In_2Se_3 based FBAR (Sample D)

To test the tunability and switchability of the α-In_2Se_3 based FBARs, RF excitation signals and DC bias voltages were applied to the top electrode of the samples at the same time. The RF and DC signal form an electric field through the α-In_2Se_3 flake in the out-of-plane direction. The RF&DC test has been performed to Samples A, D and E, respectively. Unfortunately, Sample A was destroyed during the test under high DC voltage applied, while Sample E has relatively weak vibration. The results of Sample D are presented as follows.

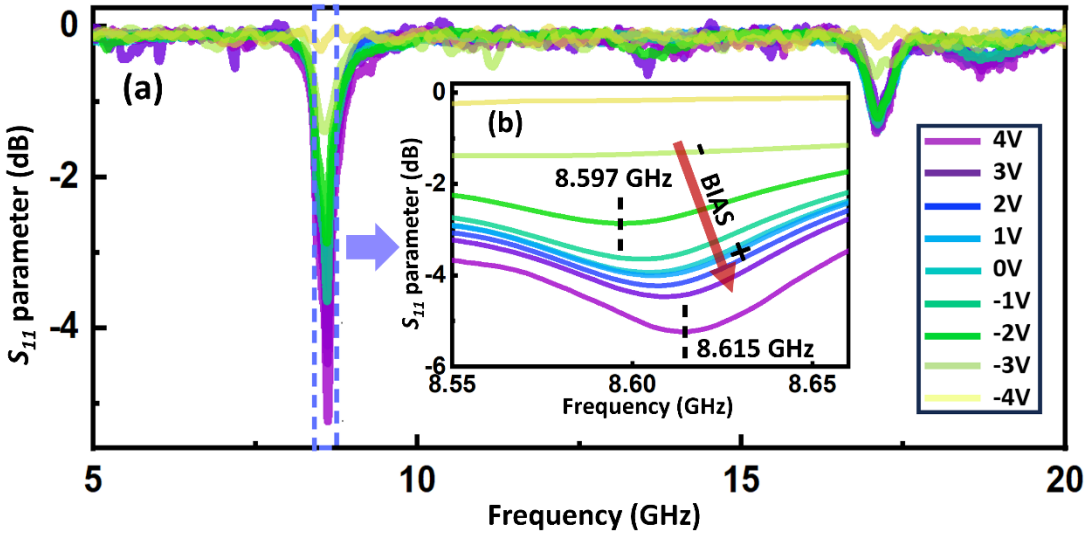

Figure 6-7 (a) Measured S_{11} parameter under DC bias from 4 V to – 4 V with a step of 1 V for Sample D. The inset (b): a zoom in view of the resonance peak.

Figure 6-7 (a) displays the measured scattering parameter S_{11} of Sample D over a frequency range of 5-20 GHz, under a DC voltage between 4 V and – 4 V with a step of 1 V. Tuning of the f_r by DC bias could be clearly observed from the zoom in view in Figure 6-7 (b). The minimum value of the measured S_{11} parameters increased from – 5.24 dB (8.615 GHz) at 4 V, through – 3.93 dB (8.604 GHz) at 0 V, up to – 2.86 dB (8.597 GHz) at – 2 V. When – 4 V was applied, the S_{11} curve fell into the noise background, suggesting that no resonance occurs, or the device is switched off under a bias voltage of – 4 V.

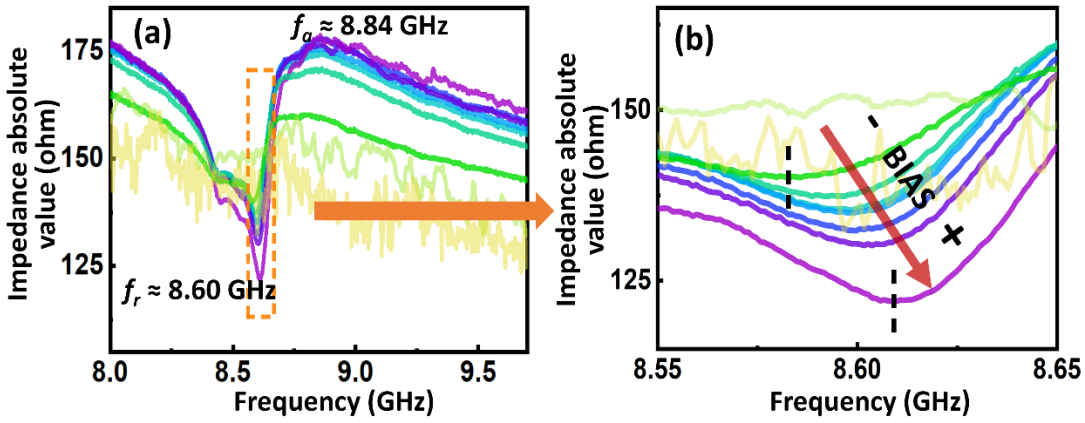

Figure 6-8 (a) Measured absolute impedance versus frequency under different DC bias voltage for Sample D. (b) The zoom in view near f_r.

The absolute impedance versus frequency for Sample D under different DC bias is shown in Figure 6-8 (a). When the DC bias voltage was tuned from 4 V to – 2 V, the absolute impedance at the f_r increases, while that at f_a decreases. The resonant and anti-resonant responses can hardly be observed under the DC bias voltage of – 4 V, suggesting that no resonant vibration could occur under such a bias voltage.

As shown in the zoom in view in Figure 6-8 (b), f_r was modulated from 8.609 GHz at 4 V to 8.583 GHz at – 2 V, realizing a tuning frequency window of 26 MHz, a tunability of 0.05%/V and a remarkably high tuning efficiency of 4.3 MHz/V. To the best of our knowledge, this is the first tunable FBAR that can function beyond the sub-6 GHz band with a high tuning efficiency and smallest switchsw-off voltage so far.[70, 71]

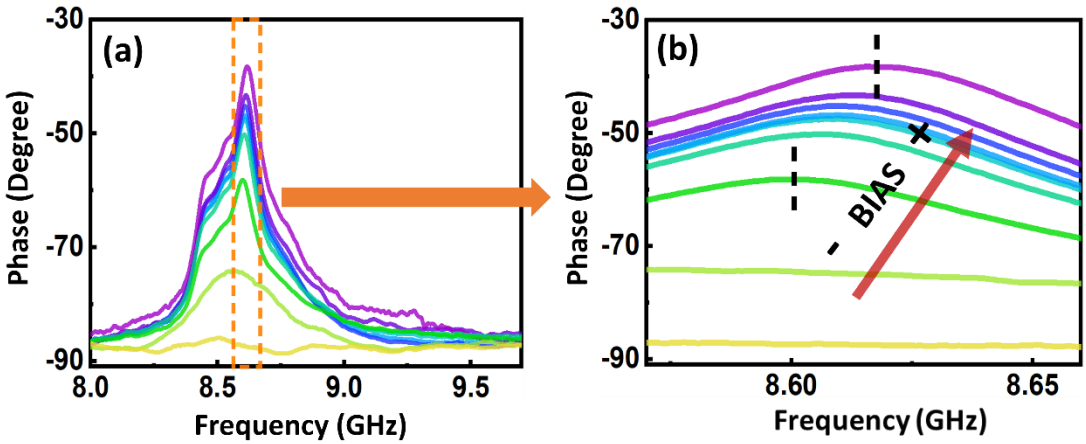

Figure 6-9 (a) Measured phase versus frequency under different DC bias voltages for Sample D. (b) The zoom in view near f_r.

It can be observed from Figure 6-9 (a) that, near f_r, Sample D experienced a phase

change from capacitive to inductive. The peak phase decreased from – 38.32° (8.618 GHz) at 4 V, through – 47.55° (8.608 GHz) at 0 V, down to – 60.53° (8.577 GHz) at – 2 V. No measurable phase change can be observed under – 4 V.

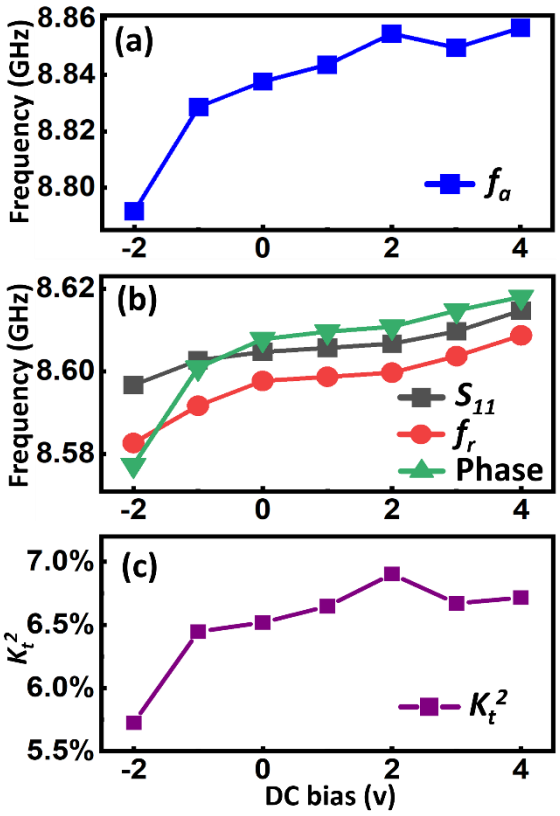

Figure 6-10 The DC bias dependence of the peak frequency for (a) f_a, (b) S_{11} parameter, f_r, and the phase and (c) K_t^2 for Sample D.

Figure 6-10 summarizes the tuning of the peak frequency for f_a, f_r, S_{11} peak, phase peak by different DC bias voltage. The peak frequency for f_a, f_r, S_{11} and the phase display a similar response to the DC bias voltage, as shown in Figure 6-10 (a) and (b). The K_t^2 attenuated with the decrease of the DC bias voltage as shown in Figure 6-10 (c), suggesting that the α-In_2Se_3 flake involved gradually loses its piezoelectricity when the DC bias voltage was increased negatively

.

6.3.4 Tunability and switchability of another α-In_2Se_3 based FBAR (Sample E)

Sample E showed the similar DC response as Sample D. However, due to thin α-In_2Se_3 flake (~95 nm), the vibration of Sample E was found to be relatively weak in comparison with Sample D.

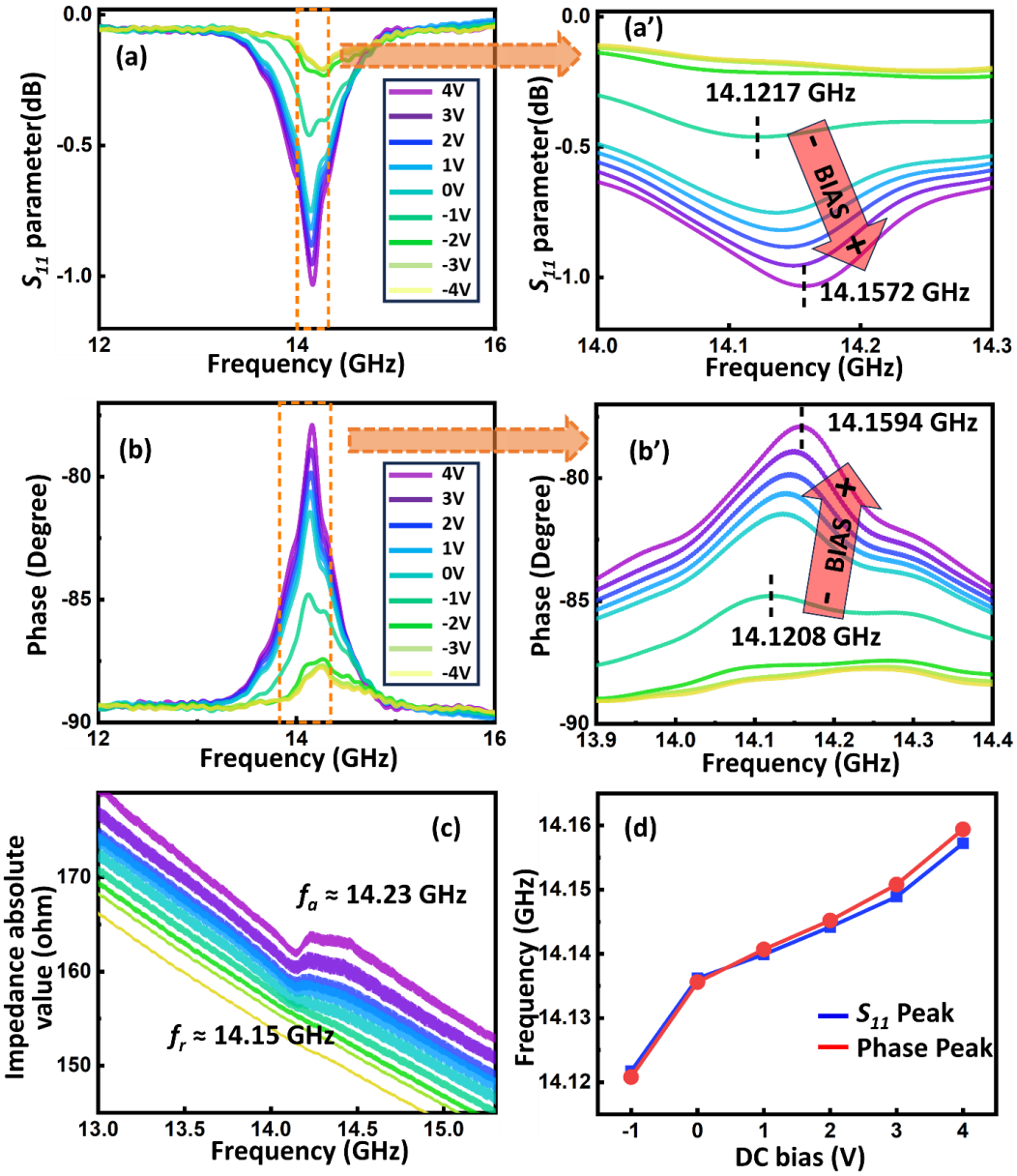

Figure 6-11 (a) Measured S_{11} parameter of an α-In_2Se_3 based FBAR (Sample E) under DC bias from 4 V to – 4 V with a step of 1 V. (a') Zoom in view of (a). (b) Electrical phase under different DC bias. (b') Zoom in view of (b). (c) Absolute impedance versus frequency under different DC bias (Figure a-c share the same color bar of DC bias voltage) (d) The peak frequency for S_{11} parameter and phase versus DC bias voltage.

DC bias voltages from – 4 V to 4 V were applied to the top electrodes of Sample E forming an electric field through the 95 nm α-In_2Se_3 flake in the out of plane direction. Figure 6-11 (a) and the zoom in view (Figure 6-11 (a')) show the S_{11} parameter around

the resonant frequency. The minimum S_{11} parameter (frequency) increased from – 1.03 dB (14.157 GHz) at 4 V, through – 0.75 dB (14.136 GHz) at zero bias, up to – 0.46 dB (14.122 GHz) at – 1.0 V. When negative DC bias voltage from – 2.0 V to – 4.0 V were applied, the S_{11} curve was buried by the noise level, no resonance was observable.

Figure 6-11 (b) and the zoom in view (Figure 6-11 (b')) show the phase near the resonant frequency of Sample E. The maximum phase (frequency) was changed from – 77.88° (14.159 GHz) at 4 V, through – 81.43° (14.136 GHz) at zero bias, down to – 84.78° (14.121 GHz) at – 1 V. No phase change was observable when negative DC biases of – 2.0 V or larger were applied.

From the absolute impedance near the resonant frequency of Sample E (Figure 6-11 (c)), one can see that the resonant frequency and the anti-resonant frequency were around 14.15 GHz and 14.23 GHz, respectively. With tuning the DC bias voltage from 4 V to – 4 V, the impedance curve gradually evolved into a straight line.

The S_{11} peak and phase peak of Sample E display an analogous way in responsible to the DC bias voltages shown in Figure 6-11 (d), suggesting a tuning efficiency (tunability) around 7 MHz/V (0.05%/V) for the 95 nm α-In_2Se_2 based FBAR under a small DC bias voltage range from – 1 V to 4 V.

6.3.5 Tunability and Comparison of our devices with other dynamic FBARs

Comparison of the performances between our α-In_2Se_3 based FBARs and FBARs based on several mainstream ferroelectric materials is shown in Table 6-1.

Materials	**Resonant Frequency**	**Tuning Efficiency**	**Tuning Range**	**Switched-off Voltage**	**Reference**
STO	2.2GHz	0.067%	1.62%	Normally-off	[111]
BST	3.76GHz	0.04%	2.3%	Normally-off	[70]
Crystalline PZT	2.42GHz	1%	16.6%	-4.6V	[112]
AlScN	2.93GHz	0.007%	2.9%	350V	[68]
α-In_2Se_3	8.60GHz	0.05%	0.3%	- 4V	This work

Table 6-1 Performance comparison between our α-In_2Se_3 based FBARs and other reported FBARs based on STO, BST, Crystalline PZT and AlScN in terms of the resonant frequency, tuning efficiency, tunability and switched-off voltage.

Our α-In_2Se_3 based FBARs show the highest resonant frequency. They possess the smallest switched-off voltage among all the other FBAR devices by other groups. The tuning efficiency of our α-In_2Se_3 based FBAR is larger than AlScN based FBARs, comparable with STO/BST based FBARs, but largely lower than the crystalline PZT based FBARs. α-In_2Se_3 based FBAR has relatively low tuning range among all the devices.

6.3.6 Mechanism of the switchability and tunability of α-In_2Se_3 based FBARs

The generation of the longitudinal acoustic wave inside the α-In_2Se_3 based FBARs originates from the strong out-of-plane piezoelectricity of the α-In_2Se_3 flakes. While the DC controlled switchability and tunability of the α-In_2Se_3 based FBARs results from the room-temperature ferroelectricity of the α-In_2Se_3 flakes.

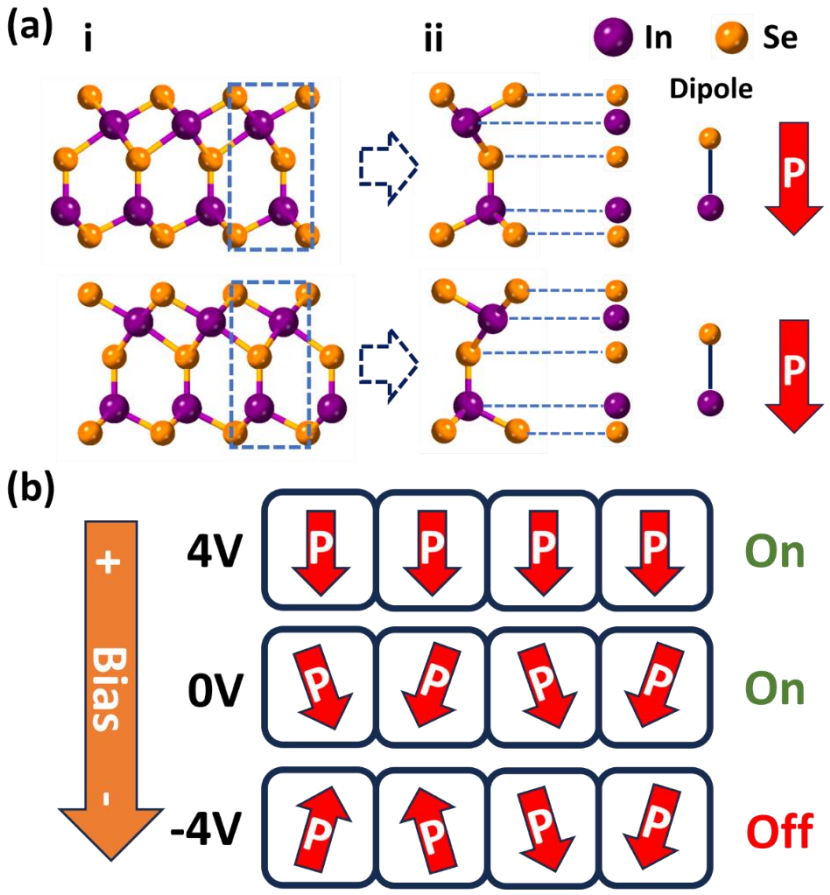

Figure 6-12 (a)(i) Atomic structure of 2H α-In_2Se_3. (ii) Illustration of vertical dipoles and polarizations of adjacent layers of 2H α-In_2Se_3 resulting from its asymmetric structure. (b)Schematic diagram of the polarization direction of the domains in α-In_2Se_3 flake in response to the DC bias.

An α-In_2Se_3 flake is constructed from a space group $P6_3mc$ with hexagonal stacking (2H). Adjacent Se-In-Se-In-Se quintuple layers with a 60 degree in-plane rotation relative to each other are bonded through vdWs force as illustrated in Figure 6-12 (a)(i).[113] The vertically oriented dipoles, resulting from the vertical dislocation between positive indium ion centers and negative selenium ion centers, have the same orientation in each quintuple layer, contributing to the intrinsic out-of-plane polarization or ferroelectric characteristics.[26]

The switchability of α-In_2Se_3 based FBARs can be interpreted using the illustrations of the domains' polarization tuned by DC bias voltage inside an α-In_2Se_3 flake shown in Figure 6-12. When the applied external electric field aligns with the polarization direction of the α-In_2Se_3 flake (corresponding to the positive DC bias voltages in our case), the vertical dislocation between the two ion centers would be stretched, enhancing the out-of-plane piezoelectricity of the α-In_2Se_3 flake. As a result, the vibrations near the

resonant frequencies are strengthened under positive bias voltages. In contrast, an external electric field opposite to the polarization direction (corresponding to the negative DC bias voltages in our case) could lead to reduction of the vertical dislocation between the two ion centers, so that the polarization direction in some domains could be reversed. When the negative bias is increased up to a certain value, around half of the domains undergo a reverse of their polarization direction, opposite to the rest domains. As a result, the overall net polarization could vanish, resulting in nearly zero out-of-plane piezoelectric coefficient. Consequently, the α-In_2Se_3 based FBAR device would disfunction as an acoustic wave resonator under certain negative bias voltages, for example, – 4 V for Samples D and E. This is also qualitatively consistent with our PFM observations (see Figure 4-6 (c) and (e)) where the measured amplitude reached to the minimum under a bias voltage around – 1 V under the On-field and a bias voltage around – 2.5 V under the Off-field.

It is well understood that modulation of polarizations could cause internal electrostrictive strain. [114, 115] As discussed above, positive DC bias voltages (the electric field in the polarization direction) would create a tensile strain and higher out-of-plane acoustic velocity v_l. As $v_l \propto f_r$, the frequency modulation by the applied bias (or electric field) could mainly originate from the strain modulation.

6.4 Summary

Tunable and switchable FBARs based on α-In_2Se_3 flakes with high resonant frequencies of 8.60 GHz are successfully designed, fabricated, and characterized. The devices have demonstrated high tuning efficiency of 4.3 MHz/V (0.05% tuning/V at the resonant frequency up to 8.60 GHz). The devices are at the on-state under zero bias voltage and can be switched off under a small bias voltage of − 4 V. The bias voltage dependence of the resonant frequency tunability and resonance switchability originate from the unique atomic structure and the polarization directions of the domains in α-In_2Se_3 flakes. Utilization of 2D piezo/ferroelectric materials, like α-In_2Se_3 flakes in this study, for tunable and switchable FBAR devices is promising for high performance tunable and switchable FBARs in RF circuit and multi-band, high-speed communications.

Chapter 7 Conclusion and Future Work

7.1 Conclusion

In this thesis, a systematic study of 2D piezoelectric/ferroelectric materials has been conducted for development of high performance FBARs. 3R-MoS_2 multilayer flakes were experimentally confirmed to be of good piezoelectricity. α-In_2Se_3 multilayer flakes were found to possess not only good piezoelectricity but also ferroelectricity. 2D piezoelectric 3R-MoS_2 based SMR-type FBARs with the resonant frequencies up to 27.5 GHz and 2D ferroelectric α-In_2Se_3 based tunable and switchable FBARs with the resonant frequencies of 8.60 GHz have been successfully designed and fabricated for the first time, to the best of our knowledge.

The out-of-plane piezoelectricity of 3R-MoS_2 flakes with thickness ~200 nm and α-In_2Se_3 flakes with the thickness ranged from 50 to 200 nm have been characterized by PFM technique. The out-of-plane piezoelectric coefficient d_{33} of 3R-MoS_2 flakes was found to be 2.0-3.5 pm/V. The out-of-plane piezoelectric coefficient d_{33} for α-In_2Se_3 flakes with thickness from 50 to 200 nm was found to increase from 4 to 7 pm/V. The ferroelectricity of α-In_2Se_3 flakes was confirmed by the DART mode PFM in which hysteresis loops were clearly observed in both On-field and Off-field.

3R-MoS_2 based SMR-type FBARs have been designed according to the observed piezoelectric properties of 3R-MoS_2 multilayer flakes and successfully fabricated with conventional semiconductor device fabrication techniques. The SMR devices with 210-290 nm 3R-MoS_2 flakes involved could operate at frequencies higher than 20 GHz. The SMR with 240 nm 3R-MoS_2 flakes involved was of very high electromechanical coupling coefficient K_t^2 of 47.6%. According to the FEM simulation, the observed resonance belongs to the fundamental longitudinal acoustic modes. Boost of the operating frequencies originates from the excellent piezoelectricity and atomically flat surface of the sub-micron thick 2D 3R-MoS_2 flakes. This work proves that utilization of 2D piezoelectric materials could be a feasible way-out to break through the limitations to high performance FBAR devices based on conventional piezoelectric materials reported so far.

α-In_2Se_3 based air gap type FBARs have been designed and fabricated. The RF characterization under different DC bias voltages was conducted to test the switchability and tunability of the devices. High tuning efficiency of 4.3 MHz/V (0.05% tuning/V at

the resonant frequency of 8.60 GHz) was achieved by the device with a 160 nm thick α-In_2Se_3 flake involved. They were at the on-state under zero bias and could be switched off under a small bias voltage of − 4 V. The bias voltage dependence of the resonant frequency tunability and resonance switchability originates from the unique atomic structure and the switchable polarization directions of the domains in α-In_2Se_3 flakes. This work shows that 2D ferroelectric materials are promising for tunable and switchable FBARs with high operational frequencies, large tuning efficiency and good swichability.

Both 3R-MoS_2 based SMRs and α-In_2Se_3 based air gap type FBARs are repeatable under our laboratory conditions. As the challenge of synthesizing large area atomically flat 2D piezoelectric materials has not be conquered, 2D-based FBARs are not industrially or commercially viable at this stage.

7.2 Future Work

This thesis has showcased that 2D piezoelectric materials are promising for high performance FBAR devices. As this is the first report on 2D materials based FBAR devices, the design and fabrication of the devices are still in the proof-of-concept stage. There is a large room to improve the performance of the devices and optimize the architectures of the devices. Several important systematic studies could be conducted in this field in future, including exploring new 2D piezoelectric materials and developing new types of acoustic devices. Hence, several recommendations for the future works are summarized as follows:

- To optimize the design of the fabricated devices and to develop RF filters with the developed 2D piezoelectric material based FBARs. For 3R-MoS_2 based SMRs, the quality of the Bragg mirror requires further improvement in both design and fabrication processes. Mismatch between the Bragg mirror and the 3R-MoS_2 flake could be solved by growing the 2D materials in a thermal CVD system with precise thickness control. For α-In_2Se_3 based FBARs, the depth and the width of the air gap, and the thickness of the supporting layer can be optimized to enlarge the vibration of the piezoelectric materials. Additionally, the performance of the FBARs could be further improved by optimizing the

materials and thickness of the electrodes, the impedance matching of the outer circuit and the de-embedding technique.

- To decrease the thickness of the 2D piezoelectric materials involved in the FBARs to further increase the resonant frequencies of the FBARs. Since 2D piezoelectric materials could maintain their piezoelectricity with thickness down to a single atomic layer, it might be feasible to develop ultrahigh resonant frequency FBARs with very thin 2D piezoelectric materials. The upper limit of the resonant frequencies of the FBARs could be explored, and quantum effect may have to be introduced when the acoustic wavelength is approaching to the thickness of few atomic layers.
- The interface effects between the piezoelectric nanoflakes and the electrodes can affect the resonant frequency of the FBARs. This influence becomes more significant as the film thickness is further reduced. A model could be developed to analyze the impact of these interface effects by examining the relationship between the resonant frequencies and film thickness.
- Beyond telecommunication, 2D-based FBARs may have potential applications such as sensors and detectors. For example, In_2Se_3 nano flakes have excellent surface adsorption capabilities for gases like NO_2, NH_3, and CO_2.[116, 117] As a result, In_2Se_3 FBARs could be used as gas sensors.[16] It has been reported that the surface chemistry of MoS_2 flakes is compatible with biological systems.[118]. MoS_2 based FBARs might have potential in detecting biomolecules. Since 2D-based FBARs have been successfully developed, and no research has been conducted in those field, studying of the 2D-FBAR based sensors and detectors could lead to promising results.
- Unique merits may come from the stacking structures of the 2D vdWs layered materials. It's highly worth to conduct more work to experimentally study the elastic/piezoelectric properties of the 2D materials. Notably, several components of the stiffness matrix and piezoelectric coefficient matrix for 2D piezoelectric materials are either poorly understood or lack experimental confirmation. For instance, existing techniques are insufficient for accurately measuring in-plane and shear piezoelectric coefficients in these materials. Developing advanced characterization methods and conducting more comprehensive studies on 2D

materials would address these gaps and further unlock their potential.

- Most of the 2D piezoelectric materials possess the odd-even effect that the piezoelectricity would be canceled out for adjacent layers because of their opposite polarization directions, which highly limits the applications of them. However, several 2D piezoelectric materials do not affected by the odd-even effect. In addition to 3R MoS_2 and α-In_2Se_3, CIPS ($CuInP_2S_6$) is another 2D piezoelectric material which possess room-temperature ferroelectricity and good dielectric properties, regardless of its thickness. As a result, it might be interesting to develop CIPS based tunable and switchable FBARs. For FBAR design, the XBAR structure is easily fabricated and is suitable for the piezoelectric materials which can be excited by lateral field. Employing 2D piezoelectric materials for XBAR may lead to very interesting and meaningful results.

Publication List:

1. Yang Yang, Jiayi Sun, Weifan Cai, Zheng Liu, Corinne Dejous, Magali De Matos, Hamida Hallil, and Qing Zhang. "Solidly Mounted Resonators with Ultra-High Operating Frequencies Based on 3R-MoS2 Atomic Flakes." *Advanced Functional Materials* 33, no. 29 (2023): 2300104.
2. Sun, Jiayi, Weifan Cai, Yang Yang, Yihao Zhuang, and Qing Zhang. "2D α-In2Se3 Flakes for High Frequency Tunable and Switchable Film Bulk Acoustic Wave Resonators." *Advanced Electronic Materials*: 2400498.
3. Deng Shuo, Ran Xu, Weibin Seh, Jiayi Sun, Weifan Cai, Jianping Zou, and Qing Zhang. "Current degradation mechanism of tip contact metal-silicon Schottky nanogenerator." *Nano Energy* 94 (2022): 106888.

Reference

1. El Hassan, M., et al., *Techniques for tuning BAW-SMR resonators for the 4th generation of mobile communications,* in *Modeling and Measurement Methods for Acoustic Waves and for Acoustic Microdevices*. 2013, IntechOpen.
2. Ruby, R., et al. *Acoustic FBAR for filters, duplexers and front end modules*. in *2004 IEEE MTT-S International Microwave Symposium Digest (IEEE Cat. No. 04CH37535)*. 2004. IEEE.
3. Ruby, R., et al. *Ultra-miniature high-Q filters and duplexers using FBAR technology*. in *2001 IEEE International Solid-State Circuits Conference. Digest of Technical Papers. ISSCC (Cat. No. 01CH37177)*. 2001. IEEE.
4. Ruby, R.C., et al. *Thin film bulk wave acoustic resonators (FBAR) for wireless applications*. in *2001 IEEE Ultrasonics Symposium. Proceedings. An International Symposium (Cat. No. 01CH37263)*. 2001. IEEE.
5. Saddik, G.N. and R.A. York, *An L-Section DC Electric Field Switchable Bulk Acoustic Wave Solidly Mounted Resonator Filter Based on Ba 0.5 S r 0.5 TiO 3.* IEEE transactions on ultrasonics, ferroelectrics, and frequency control, 2012. **59**(9): p. 2036-2041.
6. Yang, C.-M., et al. *Highly c-axis-oriented AlN film using MOCVD for 5GHz-band FBAR filter*. in *IEEE Symposium on Ultrasonics, 2003*. 2003. IEEE.
7. Boudot, R., et al., *A solid-mounted resonator-oscillator-based 4.596 GHz frequency synthesis.* Review of Scientific Instruments, 2011. **82**(3): p. 034706.
8. Edrees, H.M., et al., *Monolithically integrated CMOS-SMR oscillator in 65 nm CMOS using custom MPW die-level fabrication process.* Journal of Microelectromechanical Systems, 2017. **26**(4): p. 846-858.
9. Johnston, M.L., I. Kymissis, and K.L. Shepard, *FBAR-CMOS oscillator array for mass-sensing applications.* IEEE Sensors Journal, 2010. **10**(6): p. 1042-1047.
10. Steinem, C. and A. Janshoff, *Piezoelectric sensors*. Vol. 5. 2007: Springer Science & Business Media.
11. Wei, C.-L., et al., *Highly sensitive UV sensors based on SMR oscillators.* Procedia Engineering, 2012. **36**: p. 468-475.
12. Wingqvist, G., *AlN-based sputter-deposited shear mode thin film bulk acoustic resonator (FBAR) for biosensor applications—A review.* Surface and Coatings Technology, 2010. **205**(5): p. 1279-1286.
13. Chu, Y., et al., *Creation and control of multi-phonon Fock states in a bulk acoustic-wave resonator.* Nature, 2018. **563**(7733): p. 666-670.
14. Tian, H., et al., *Hybrid integrated photonics using bulk acoustic resonators.* Nature communications, 2020. **11**(1): p. 1-8.
15. Uchino, K., *Piezoelectric actuators 2006.* Journal of Electroceramics, 2008. **20**(3): p. 301-311.
16. Gabl, R., et al. *Novel integrated FBAR sensors: a universal technology platform for bio-and gas-detection*. in *SENSORS, 2003 IEEE*. 2003. IEEE.
17. Lee, T.Y. and J.T. Song, *Detection of carcinoembryonic antigen using AlN FBAR.* Thin Solid Films, 2010. **518**(22): p. 6630-6633.
18. Patel, R., et al., *FEM modeling of solidly mounted film bulk acoustic resonator and gas sensor using PIB-sensitive layer.* Journal of Micro/Nanolithography, MEMS, and MOEMS, 2017. **16**(2): p. 025002.
19. Zhang, Y. and D. Chen, *Multilayer integrated film bulk acoustic resonators*.

2012: Springer Science & Business Media.
20. Ababneh, A., et al., *The influence of sputter deposition parameters on piezoelectric and mechanical properties of AlN thin films.* Materials Science and Engineering: B, 2010. **172**(3): p. 253-258.
21. Shirakawa, A., et al., *Design of FBAR filters at high frequency bands.* International Journal of RF and Microwave Computer ‐ Aided Engineering: Co ‐ sponsored by the Center for Advanced Manufacturing and Packaging of Microwave, Optical, and Digital Electronics (CAMPmode) at the University of Colorado at Boulder, 2007. **17**(1): p. 115-122.
22. Fan, Z., et al., *Defect annihilation in AlN thin films by ultrahigh temperature processing.* Applied Physics Letters, 2000. **76**(14): p. 1839-1841.
23. Dong, L., J. Lou, and V.B. Shenoy, *Large in-plane and vertical piezoelectricity in Janus transition metal dichalchogenides.* ACS nano, 2017. **11**(8): p. 8242-8248.
24. Hinchet, R., et al., *Piezoelectric properties in two-dimensional materials: Simulations and experiments.* Materials Today, 2018. **21**(6): p. 611-630.
25. Tan, D., M. Willatzen, and Z.L. Wang, *Prediction of strong piezoelectricity in 3R-MoS2 multilayer structures.* Nano Energy, 2019. **56**: p. 512-515.
26. Xue, F., et al., *Multidirection piezoelectricity in mono-and multilayered hexagonal α-In2Se3.* ACS nano, 2018. **12**(5): p. 4976-4983.
27. Zhou, Y., et al., *Out-of-plane piezoelectricity and ferroelectricity in layered α-In2Se3 nanoflakes.* Nano letters, 2017. **17**(9): p. 5508-5513.
28. Zhu, H., et al., *Observation of piezoelectricity in free-standing monolayer MoS 2.* Nature nanotechnology, 2015. **10**(2): p. 151-155.
29. Hallil, H., et al., *Strong Piezoelectricity in 3R ‐ MoS2 Flakes.* Advanced Electronic Materials, 2022: p. 2101131.
30. Wang, W., Y. Jiang, and P.J. Thomas, *Structural design and physical mechanism of axial and radial sandwich resonators with piezoelectric ceramics: a review.* Sensors, 2021. **21**(4): p. 1112.
31. Arnau, A., *Piezoelectric transducers and applications*. Vol. 2004. 2004: Springer.
32. Gautschi, G. and G. Gautschi, *Piezoelectric sensors*. 2002: Springer.
33. Erturk, A. and D.J. Inman, *Piezoelectric energy harvesting*. 2011: John Wiley & Sons.
34. Jaffe, H., *Piezoelectric ceramics.* Journal of the American Ceramic Society, 1958. **41**(11): p. 494-498.
35. Uchino, K., *Advanced piezoelectric materials: Science and technology*. 2017: Woodhead Publishing.
36. De Jong, M., et al., *A database to enable discovery and design of piezoelectric materials.* Scientific data, 2015. **2**(1): p. 1-13.
37. Wu, M., et al., *Acoustofluidic separation of cells and particles.* Microsystems & nanoengineering, 2019. **5**(1): p. 1-18.
38. Liu, Y., et al., *Materials, design, and characteristics of bulk acoustic wave resonator: A review.* Micromachines, 2020. **11**(7): p. 630.
39. Kim, E.K., et al., *Air gap type thin film bulk acoustic resonator fabrication using simplified process.* Thin Solid Films, 2006. **496**(2): p. 653-657.
40. Campanella, H., *Acoustic wave and electromechanical resonators: concept to key applications*. 2010: Artech House.
41. ONSCALE. *Design and Optimization of FBAR Filters to Enable 5G* 2018 13 Augest 2024]; Available from: https://spectrum.ieee.org/design-and-

optimization-of-fbar-filters-to-enable-5g.
42. Nyikayaramba, G. and B. Murmann, *S-Parameter-Based Defect Localization for Ultrasonic Guided Wave SHM.* Aerospace, 2020. **7**(3): p. 33.
43. Bai, X., et al., *The thin film bulk acoustic wave resonator based on single-crystalline 4 3 ○ Y-cut lithium niobate thin films.* Aip Advances, 2020. **10**(7): p. 075002.
44. Umeda, K., et al. *Piezoelectric properties of ScAlN thin films for piezo-MEMS devices*. in *2013 IEEE 26th International Conference on Micro Electro Mechanical Systems (MEMS)*. 2013. IEEE.
45. Lee, J.B., et al., *Deposition of ZnO thin films by magnetron sputtering for a film bulk acoustic resonator.* Thin Solid Films, 2003. **435**(1-2): p. 179-185.
46. Yokoyama, T., et al., *Highly piezoelectric co-doped AlN thin films for wideband FBAR applications.* IEEE transactions on ultrasonics, ferroelectrics, and frequency control, 2015. **62**(6): p. 1007-1015.
47. Chen, L., et al., *Scandium-doped aluminum nitride for acoustic wave resonators, filters, and ferroelectric memory applications.* ACS Applied Electronic Materials, 2022. **5**(2): p. 612-622.
48. Nagakubo, A., et al., *Acoustic properties of co-doped AlN thin films at low temperatures studied by picosecond ultrasonics.* Japanese Journal of Applied Physics, 2015. **54**(7S1): p. 07HD01.
49. Han, C., et al., *The deposition and wet etching of Mg-doped ZnO films and their applications for solidly mounted resonators.* RSC advances, 2020. **10**(16): p. 9672-9677.
50. Duan, F.L., et al., *Process optimization and device variation of Mg-doped ZnO FBARs.* Solid-State Electronics, 2019. **151**: p. 11-17.
51. Chen, Y., et al., *Multifunctional ZnO-based thin-film bulk acoustic resonator for biosensors.* Journal of electronic materials, 2009. **38**: p. 1605-1611.
52. Kim, E.K. and Y.S. Kim, *The effect on the annealing temperature of Li doped ZnO thin film for a film bulk acoustic resonator.* Superlattices and Microstructures, 2007. **42**(1-6): p. 343-347.
53. Chen, H.-H., et al., *Microstructure and piezoelectric properties of hexagonal MgxZn1− xO/ZnO films at lower Mg compositions.* Thin Solid Films, 2019. **690**: p. 137459.
54. Gong, S., *Lithium niobate for M/NEMS resonators.* Piezoelectric MEMS Resonators, 2017: p. 99-129.
55. Gorisse, M., et al. *High frequency LiNbO 3 bulk wave resonator*. in *2019 Joint Conference of the IEEE International Frequency Control Symposium and European Frequency and Time Forum (EFTF/IFC)*. 2019. IEEE.
56. Lu, R., et al., *A1 resonators in 128° Y-cut lithium niobate with electromechanical coupling of 46.4%.* Journal of Microelectromechanical Systems, 2020. **29**(3): p. 313-319.
57. Chen, G. and M. Rinaldi, *Aluminum nitride combined overtone resonators for the 5G high frequency bands.* Journal of Microelectromechanical Systems, 2020. **29**(2): p. 148-159.
58. Baron, T., et al., *High-overtone bulk acoustic resonator.* Modeling and Measurement Methods for Acoustic Waves and for Acoustic Microdevices, 2013: p. 297.
59. Schaffer, Z., P. Simeoni, and G. Piazza, *33 GHz overmoded bulk acoustic resonator.* IEEE Microwave and Wireless Components Letters, 2022. **32**(6): p. 656-659.

60. Lau, W.W., Y. Song, and E.S. Kim. *Lateral-field-excitation acoustic resonators for monolithic oscillators and filters*. in *Proceedings of 1996 IEEE International Frequency Control Symposium*. 1996. IEEE.
61. Assylbekova, M., et al. *11 GHz lateral-field-excited aluminum nitride cross-sectional Lamé mode resonator*. in *2020 Joint Conference of the IEEE International Frequency Control Symposium and International Symposium on Applications of Ferroelectrics (IFCS-ISAF)*. 2020. IEEE.
62. Yang, Y., et al. *Toward Ka band acoustics: Lithium niobate asymmetrical mode piezoelectric MEMS resonators*. in *2018 IEEE International Frequency Control Symposium (IFCS)*. 2018. IEEE.
63. Yang, Y., et al. *5 GHz lithium niobate MEMS resonators with high FoM of 153*. in *2017 IEEE 30th International Conference on Micro Electro Mechanical Systems (MEMS)*. 2017. IEEE.
64. Gevorgian, S.S., A.K. Tagantsev, and A.K. Vorobiev, *Tuneable film bulk acoustic wave resonators*. 2013: Springer.
65. Zhu, X., J.D. Phillips, and A. Mortazawi. *A DC voltage dependant switchable thin film bulk wave acoustic resonator using ferroelectric thin film*. in *2007 IEEE/MTT-S International Microwave Symposium*. 2007. IEEE.
66. Zhu, X., et al., *An intrinsically switchable FBAR filter based on barium titanate thin films.* IEEE microwave and wireless components letters, 2009. **19**(6): p. 359-361.
67. Lee, V.C., *Switchable and Tunable Ferroelectric Devices for Adaptive and Reconfigurable RF Circuits*. 2014.
68. Wang, J., et al., *A film bulk acoustic resonator based on ferroelectric aluminum scandium nitride films.* Journal of Microelectromechanical Systems, 2020. **29**(5): p. 741-747.
69. Koohi, M.Z., S. Lee, and A. Mortazawi. *Fabrication of a Low insertion loss intrinsically switchable BAW filter based on BST FBARs*. in *2017 IEEE MTT-S International Microwave Symposium (IMS)*. 2017. IEEE.
70. Yang, T.-Y., et al., *Tunable Ba0. 5Sr0. 5TiO3 film bulk acoustic resonators using SiO2/Mo Bragg reflectors.* Chinese Physics B, 2012. **21**(10): p. 106801.
71. Lee, S., et al. *Linearity analysis of intrinsically switchable ferroelectric FBAR filters*. in *2013 IEEE MTT-S International Microwave Symposium Digest (MTT)*. 2013. IEEE.
72. Iqbal, A. and F. Mohd-Yasin, *Reactive sputtering of aluminum nitride (002) thin films for piezoelectric applications: A review.* Sensors, 2018. **18**(6): p. 1797.
73. You, L., et al., *Origin of giant negative piezoelectricity in a layered van der Waals ferroelectric.* Science advances, 2019. **5**(4): p. eaav3780.
74. Wu, W., et al., *Piezoelectricity of single-atomic-layer MoS2 for energy conversion and piezotronics.* Nature, 2014. **514**(7523): p. 470-474.
75. Vorobiev, A., et al., *Effect of interface roughness on acoustic loss in tunable thin film bulk acoustic wave resonators.* Journal of Applied Physics, 2011. **110**(2).
76. Instruments, O., *Piezoresponse Force Microscopy with Asylum Research AFMs*.
77. Nandra, S., *High‐rate sputter deposition of SiO2 and TiO2 films for optical applications.* Journal of Vacuum Science & Technology A: Vacuum, Surfaces, and Films, 1990. **8**(4): p. 3179-3185.
78. Sandager, M.K., C. Kjelde, and V. Popok, *Growth of Thin AlN Films on Si Wafers by Reactive Magnetron Sputtering: Role of Processing Pressure, Magnetron Power and Nitrogen/Argon Gas Flow Ratio*. Crystals, 2022. **12**(10): p. 1379.

79. Vanamoorthy, M., B. Salim, and K. Mohanta, *Study on optimizing c-axis oriented AlN thin film for piezoelectric sensing applications controlling the sputtering process parameters.* Applied Physics A, 2022. **128**(1): p. 48.
80. Saif, A.e.A., N. Ramli, and P. Poopalan, *AFM study of multilayer sol-gel BaxSr1-xTiO3 thin films.* 2010.
81. Wang, Z.L., *Nanopiezotronics.* Advanced Materials, 2007. **19**(6): p. 889-892.
82. Konabe, S. and T. Yamamoto, *Piezoelectric coefficients of bulk 3R transition metal dichalcogenides.* Japanese Journal of Applied Physics, 2017. **56**(9): p. 098002.
83. Tiemeijer, L.F., et al., *Comparison of the" pad-open-short" and" open-short-load" deembedding techniques for accurate on-wafer RF characterization of high-quality passives.* IEEE Transactions on Microwave Theory and Techniques, 2005. **53**(2): p. 723-729.
84. Worsley, M.A., et al., *Ultralow density, monolithic WS2, MoS2, and MoS2/graphene aerogels.* ACS nano, 2015. **9**(5): p. 4698-4705.
85. Yang, Y., *Modeling and design of a new generation of RF piezoelectric acoustic wave devices based on atomic monolayers of transition metal dichalcogenides*. 2023, Université de Bordeaux.
86. Bai, X., et al., *Mo/Ti multilayer Bragg reflector for LiNbO3 film bulk acoustic wave resonators.* Journal of Applied Physics, 2020. **128**(9): p. 094503.
87. Bousquet, M., et al. *Lithium niobate film bulk acoustic wave resonator for sub-6 GHz filters*. in *2020 IEEE International Ultrasonics Symposium (IUS)*. 2020. IEEE.
88. Matsumoto, K., M. Kadota, and S. Tanaka, *High frequency thickness expansion mode bulk acoustic wave resonator using LN single crystal thin plate.* Japanese Journal of Applied Physics, 2020. **59**(3): p. 036506.
89. Pijolat, M., et al., *Large electromechanical coupling factor film bulk acoustic resonator with X-cut LiNbO 3 layer transfer.* Applied Physics Letters, 2009. **95**(18): p. 182106.
90. Shealy, J.B., et al. *Single crystal AlGaN bulk acoustic wave resonators on silicon substrates with high electromechanical coupling*. in *2016 IEEE Radio Frequency Integrated Circuits Symposium (RFIC)*. 2016. IEEE.
91. Hodge, M.D., et al. *High rejection UNII 5.2 GHz wideband bulk acoustic wave filters using undoped single crystal AlN-on-SiC resonators*. in *2017 IEEE International Electron Devices Meeting (IEDM)*. 2017. IEEE.
92. Segovia-Fernandez, J. and E.T.-T. Yen. *Non-Released Highly-Dispersive Aluminum Nitride Bulk Acoustic Wave Resonators*. in *2022 IEEE 35th International Conference on Micro Electro Mechanical Systems Conference (MEMS)*. 2022. IEEE.
93. Kadota, M., Y. Ishii, and S. Tanaka, *A solidly mounted, high frequency, thickness shear mode bulk acoustic wave resonator using X-LiTaO3 thin plate and SiO2/Ta multilayer acoustic films.* Japanese Journal of Applied Physics, 2021. **60**(SD): p. SDDC11.
94. Yokoyama, T., et al., *Effect of Mg and Zr co-doping on piezoelectric AlN thin films for bulk acoustic wave resonators.* IEEE Transactions on Ultrasonics, Ferroelectrics, and Frequency Control, 2014. **61**(8): p. 1322-1328.
95. Taniguchi, S., et al. *7E-1 an air-gap type FBAR filter fabricated using a thin sacrificed layer on a flat substrate*. in *2007 IEEE Ultrasonics Symposium Proceedings*. 2007. IEEE.
96. Johar, A.K., et al., *Modeling, fabrication, and structural characterization of thin*

film ZnO based film bulk acoustic resonator. Materials Today: Proceedings, 2021. **46**: p. 5716-5721.
97. Chen, D., et al., *Highly sensitive ZnO thin film bulk acoustic resonator for hydrogen detection.* Journal of Micromechanics and Microengineering, 2011. **21**(11): p. 115018.
98. Serhane, R., et al., *Pulsed laser deposition of piezoelectric ZnO thin films for bulk acoustic wave devices.* Applied Surface Science, 2014. **288**: p. 572-578.
99. Bousquet, M., et al. *Potentialities of LiTaO3 for Bulk Acoustic Wave Filters*. in *2020 IEEE International Ultrasonics Symposium (IUS)*. 2020. IEEE.
100. Lanz, R. and P. Muralt, *Bandpass filters for 8 GHz using solidly mounted bulk acoustic wave resonators.* IEEE transactions on ultrasonics, ferroelectrics, and frequency control, 2005. **52**(6): p. 938-948.
101. Nishihara, T., et al. *High performance and miniature thin film bulk acoustic wave filters for 5 GHz*. in *2002 IEEE Ultrasonics Symposium, 2002. Proceedings.* 2002. IEEE.
102. Umeda, K., et al., *Characteristics of an AlN-based bulk acoustic wave resonator in the super high frequency range.* Vacuum, 2008. **83**(3): p. 672-674.
103. Kubo, R., et al. *Fabrication of 5GHz band film bulk acoustic wave resonators using ZnO thin film*. in *IEEE Symposium on Ultrasonics, 2003.* 2003.
104. Bousquet, M., et al. *Single-mode high frequency LiNbO3 Film Bulk Acoustic Resonator*. in *2019 IEEE International Ultrasonics Symposium (IUS)*. 2019.
105. Link, S., et al. *An A1 Mode Resonator at 12 GHz using 160nm Lithium Niobate Suspended Thin Film*. in *2021 IEEE International Ultrasonics Symposium (IUS)*. 2021. IEEE.
106. Yang, Y., L. Gao, and S. Gong, *Surface-Acoustic-Wave Devices Based on Lithium Niobate and Amorphous Silicon Thin Films on a Silicon Substrate.* IEEE Transactions on Microwave Theory and Techniques, 2022. **70**(11): p. 5185-5194.
107. Ahmed, I., et al., *Super-High-Frequency Low-Loss Sezawa Mode SAW Devices in a GaN/SiC Platform.* IEEE Transactions on Ultrasonics, Ferroelectrics, and Frequency Control, 2023.
108. Yang, Y., et al., *Solidly Mounted Resonators with Ultra‐High Operating Frequencies Based on 3R‐MoS2 Atomic Flakes.* 2023. **33**(29): p. 2300104.
109. Liu, J. and S. Pantelides, *Pyroelectric response and temperature-induced α-β phase transitions in α-In2Se3 and other α-III2VI3 (III= Al, Ga, In; VI= S, Se) monolayers.* 2D Materials, 2019. **6**(2): p. 025001.
110. Yan, W., et al., *Nondestructive Picosecond Ultrasonic Probing of Intralayer and van der Waals Interlayer Bonding in α‐and β‐In2Se3.* Advanced Functional Materials, 2021. **31**(50): p. 2106206.
111. Volatier, A., et al., *Switchable and tunable strontium titanate electrostrictive bulk acoustic wave resonator integrated with a Bragg mirror.* Applied Physics Letters, 2008. **92**(3).
112. Cai, X., et al., *Film bulk acoustic resonators with 400 MHz ultrawide-range tunability using crystalline PZT thin film.* Materials Science in Semiconductor Processing, 2023. **167**: p. 107817.
113. Cui, C., et al., *Intercorrelated in-plane and out-of-plane ferroelectricity in ultrathin two-dimensional layered semiconductor In2Se3.* Nano letters, 2018. **18**(2): p. 1253-1258.
114. Tang, Z., et al., *Strain engineering the ferroelectric polarization and optical absorption in the FEβ-In2Se3 monolayer.* The Journal of Physical Chemistry C,

2022. **126**(24): p. 10181-10189.
115. Chen, Z., et al., *Atomic Imaging of Electrically Switchable Striped Domains in β′-In2Se3.* Advanced Science, 2021. **8**(17): p. 2100713.
116. Bolarinwa, S.O., S. Sattar, and A.A.J.C.M.S. AlShaikhi, *Superior gas sensing properties of β-In2Se3: A first-principles investigation.* 2022. **201**: p. 110880.
117. Xie, Z., et al., *Functionalization of α-In2Se3 monolayer via adsorption of small molecule for gas sensing.* 2018. **6**: p. 430.